



HAL
open science

Resonant nanophotonics: structural slow light and slow plasmons

Rémi Faggiani

► **To cite this version:**

Rémi Faggiani. Resonant nanophotonics: structural slow light and slow plasmons. Other [cond-mat.other]. Université de Bordeaux, 2016. English. NNT : 2016BORD0396 . tel-01525824

HAL Id: tel-01525824

<https://theses.hal.science/tel-01525824>

Submitted on 22 May 2017

HAL is a multi-disciplinary open access archive for the deposit and dissemination of scientific research documents, whether they are published or not. The documents may come from teaching and research institutions in France or abroad, or from public or private research centers.

L'archive ouverte pluridisciplinaire **HAL**, est destinée au dépôt et à la diffusion de documents scientifiques de niveau recherche, publiés ou non, émanant des établissements d'enseignement et de recherche français ou étrangers, des laboratoires publics ou privés.

THÈSE PRÉSENTÉE
POUR OBTENIR LE GRADE DE

**DOCTEUR DE
L'UNIVERSITÉ DE BORDEAUX**

ÉCOLE DOCTORALE DES SCIENCES PHYSIQUES ET DE L'INGENIEUR (SPI)
SPÉCIALITÉ LASERS MATIERE ET NANOSCIENCES

Par

Rémi FAGGIANI

**Resonant Nanophotonics: Structural Slow
Light and Slow Plasmons**

Sous la direction de : Philippe LALANNE

Soutenue le 09 Décembre 2016

Membres du jury :

M. COLAS DES FRANCS Gérard
Mme. DAGENS Béatrice
M. LEROSEY Geoffroy
M. ADAM Philippe
M. AMRA Claude
M. LALANNE Philippe

Laboratoire Interdisciplinaire Carnot de Bourgogne
Centre de Nanosciences et de Nanotechnologie
Institut Langevin
Direction Générale de l'Armement
Institut Fresnel
Laboratoire Photonique Numérique et Nanoscience

Président
Rapporteur
Rapporteur
Examineur
Examineur
Directeur de thèse

Title: Resonant Nanophotonics: Structural Slow Light and Slow Plasmons

Abstract: Enhancing light-matter interactions at micro and nanoscales is one of the spearheads of nanophotonics. Indeed, the control of the field distribution due to the resonant interaction of nanostructures with electromagnetic waves has prompted the development of numerous optical components for many applications in telecommunication, spectroscopy or sensing. A promising approach lies in the control of light speed in nanostructures. Light slowdown, obtained by wave interferences in periodic structures or subwavelength confinement in plasmonic waveguides, is associated to pulse compressions and large field enhancements, which are envisioned as key processes for the miniaturization of optical devices and the enhancement of light-matter interactions.

The thesis studies both fundamental aspects and possible applications related to slow light in photonic and plasmonic nanostructures. In particular, we study the impact of periodic system sizes on the group velocity reduction and propose a novel family of resonators that implement slow light on very small spatial scales. We then investigate the role of fabrication disorder in slow periodic waveguides on light localization and demonstrate how modal properties influence the confinement of localized modes. Also we propose a new hollow-core photonic crystal waveguide that provides efficient and remote couplings between the waveguide and atoms that are trapped away from it. Finally we demonstrate the important role played by slow plasmons on the emission of quantum emitters placed in nanogap plasmonic antennas and explain how large radiation efficiency can be achieved by overcoming quenching in the metal. Additionally, one part of the thesis is devoted to the derivation of a novel modal method to accurately describe the dynamics of plasmonic resonators under short pulse illumination.

Keywords: Structural slow light, Slow plasmons, Photonic crystal waveguide, Metal-insulator-metal waveguide, Plasmonic nanoresonator, Density of states, Light localization, Quasi-normal modes, Quenching, Atom-photon interaction.

Titre : Résonance en Nanophotonique : Lumière Lente Structurale et Plasmons Lents

Résumé : L'augmentation de l'interaction lumière-matière aux échelles micro et nanométriques est un des fers de lance de la nanophotonique. En effet, le contrôle de la répartition spatiale de la lumière grâce à l'interaction résonante entre nanostructures et ondes électromagnétiques a conduit aux développements de nombreuses applications dans des domaines variés tels que les télécommunications, la spectroscopie et la détection d'objets. Le ralentissement de la lumière, sujet de la thèse, obtenue grâce à l'interférence d'ondes contre-propageantes dans des milieux périodiques ou le confinement sub-longueur d'onde dans des guides d'ondes plasmoniques, est associé à une compression des pulses lumineux et une forte augmentation du champ électrique, deux phénomènes clés pour la miniaturisation de composées optiques et l'augmentation de l'interaction lumière matière.

Mots clés : Lumière lente structurale, Plasmon lent, Guide à cristaux photoniques, Guide métal-diélectrique-métal, Nanorésonateur plasmonique, Densité d'états, Localisation de la lumière, Modes quasi-normaux, Quenching, Interaction atome-photon.

Unité de recherche

Laboratoire Photonique, Numérique et Nanosciences (LP2N) - UMR 5298

Institut d'Optique d'Aquitaine, LP2N, Rue F. Mitterrand,
33400 Talence, France

RESUME EN FRANÇAIS

Cette thèse, articulée autour de 5 chapitres indépendants, étudie à la fois des aspects fondamentaux et appliqués liés à la lumière lente structurale et aux plasmons lents. Les pages suivantes détaillent le contenu des 5 chapitres et donnent un aperçu des différents points abordés.

----- Chapitre 1 -----

Les systèmes périodiques infinis possèdent des vitesses de groupe extrêmement faibles et présentent une divergence de la densité d'états en bord de bande. En pratique cependant, tout système a une taille finie. Cela pose inévitablement la question de savoir si les quantités physiques définies à partir de systèmes infinis, comme la vitesse de groupe déduite du diagramme de bande, conservent leur signification dans des systèmes de tailles finies. Nous pouvons par exemple nous demander si la densité d'états d'un système infini peut être approchée ou reproduite dans un système de taille finie. Intuitivement, nous pouvons nous attendre à ce que l'implémentation d'une densité d'états de plus en plus grande, ou de manière équivalente d'une vitesse de groupe de plus en plus faibles, augmente considérablement la taille du système.

Dans le chapitre 1, nous démontrons, grâce à des arguments basés sur les ondes se propageant dans des systèmes à 1 dimension (1D), que de fortes augmentations de la densité d'états dues au seul effet de la lumière lente peuvent en réalité être observées sur des systèmes très courts, dont la taille varie avec le logarithme de l'inverse de la vitesse de groupe. La compréhension obtenue dans les systèmes 1D nous conduit à proposer une toute nouvelle famille de résonateurs photoniques, analogues de dos d'âne pour photons, dans lesquelles l'énergie électromagnétique est accumulée,

non pas à cause de l'interférence d'ondes entre deux miroirs, mais à cause d'une chute soudaine de la vitesse de groupe, suivie d'une ré-accélération à la vitesse de groupe initiale. Des simulations numériques en 3 dimensions montrent que des systèmes courts (quelques longueurs d'ondes) peuvent mimer le comportement de systèmes infinis, même pour des vitesses de groupes extrêmement faibles. Nous montrons de plus que l'augmentation de la densité d'états du dos d'âne pour photons provient d'une résonance classique caractérisée par un seul mode résonant dont la nature et les propriétés sont drastiquement différentes de celles de microcavités classiques.

----- Chapitre 2 -----

Les études initiales sur le transport de la lumière dans les guides d'ondes périodiques ont montré que les défauts résiduels de fabrication avaient un impact considérable sur la propagation de la lumière lente et limitaient sévèrement la réalisation de systèmes optiques exploitant ce phénomène [Mel14, Not01]. La conséquence la plus marquante est incontestablement la formation de modes localisés en bord de bande, généralement expliquée par la grande sensibilité de la lumière lente à des défauts aléatoires [Mel14]. Cependant, une analyse détaillée de l'extension spatiale de ces modes localisés est manquante, notamment l'analyse du plus petit confinement atteignable pour un niveau d'imperfection de fabrication donné, renseignant sur les limites de fonctionnement de ces systèmes.

Dans le chapitre 2, nous examinons l'impact des défauts de fabrication résiduels dans les guides périodiques lents sur la formation de modes fortement localisés, avec l'ambition de déterminer les paramètres clés régissant leur extension spatiale. D'un point de vue expérimental, nous observons que des modes fortement localisés apparaissent naturellement en bord de bande de guides à cristaux photoniques fabriqués sans désordre intentionnel mais seulement perturbés par des défauts de fabrication intrinsèques (perturbations d'environ 1 nm pour une longueur d'onde de 1.5

μm). Ces observations, réalisées par le groupe de Frédérique De Fornel à l'Université de Bourgogne, révèlent que le plus petit mode naturellement formé dans ce type de guide possède un volume modal de l'ordre de quelques longueurs d'onde au cube. Ce résultat surprenant soulève des questions fondamentales sur la manière dont des guides d'ondes quasiment parfait, comprenant seulement de petits défauts de l'ordre du nanomètre, peuvent modifier à tel point le transport de la lumière. Comme évoqué plus haut, la vitesse de groupe est reconnue comme étant le paramètre clé expliquant le phénomène de localisation en bord de bande, puisque faible vitesse de groupe est synonyme de forte interaction entre lumière et défauts de fabrication. Nous montrons cependant que la taille des plus petites modes localisés est en réalité régie par la masse effective, i.e. l'aplatissement de la courbe de dispersion. Nous démontrons de plus que les guides à cristaux photoniques, grâce à une masse effective plus élevée que d'autres structures périodiques telles que les empilements de Bragg, peuvent en effet supporter des modes localisés sur une longueur de l'ordre de la longueur d'onde, en accord avec les mesures expérimentales.

Ce travail a été réalisé en étroite collaboration avec les groupes de Thomas Krauss à l'Université de York et Frédérique de Fornel à l'Université de Bourgogne. Les premiers ont fabriqué les guides à cristaux photoniques tandis que les seconds ont réalisé les expériences en champ proche. Cette collaboration a conduit à une publication dans *Scientific Reports* en 2016. L'article donne les détails sur la méthode de fabrication et les mesures en champ proche qui ne sont pas détaillés dans le chapitre.

----- Chapitre 3 -----

L'intégration sur puce de composés photoniques couplés à des atomes froids offre des perspectives intéressantes dans la réalisation de nouveaux composés optiques pour le domaine de l'information quantique [Kim08a]. Dans ce contexte, un obstacle récurrent réside dans la difficulté de coupler efficacement photons uniques et atomes uniques et de piéger simultanément

les atomes à une distance suffisante de la nanostructure pour éviter de subir les forces attractives de Casimir-Polder présentes entre matière et atome. Jusqu'à présent, la nature évanescence du champ électrique dans le vide, limitant fortement la distance d'interaction due à une décroissance rapide, a empêché l'implémentation simple de couplage entre atomes et photons à l'aide de nanostructures.

Dans le chapitre 3, nous concevons un guide lent à cristaux photoniques à fente permettant d'obtenir une interaction élevée entre lumière et atomes loin de toute interface de la nanostructure. La conception repose sur l'ingénierie des propriétés d'un mode de Bloch permettant l'obtention d'un champ intense dans une fente d'environ $1 \mu\text{m}$ de large, bien plus grande que dans les précédents guides à fentes dans lesquels la taille est généralement limité à des largeurs de l'ordre de deux cents nanomètres [San07, Hun13]. L'augmentation de l'amplitude du champ électrique dans la fente est obtenue grâce à un ralentissement de la lumière et une décroissance plus lente du champ évanescent dans le vide environnant. Cependant, la conception d'un tel objet est contradictoire. D'un côté, la lumière doit être déconfinée dans le vide, et donc interagir peu avec la matière. D'un autre côté, le ralentissement de la lumière nécessite une interaction forte entre la lumière et une modulation périodique de l'indice de réfraction de la matière. Pour contourner ce problème, nous proposons un nouveau type de guide d'onde, possédant deux périodicités distinctes mais proportionnelles, permettant de contrôler l'aplatissement de la courbe de dispersion du mode proche de la ligne de lumière du vide.

----- Chapitre 4 -----

Le domaine de la plasmonique ultra-rapide a connu une croissance considérable dans la dernière décennie grâce au développement de nouveaux outils expérimentaux permettant l'observation de l'interaction lumière-matière avec une précision nanométrique sur des échelles de temps de l'ordre de la femtoseconde. Cependant, aucun outil théorique simple et

intuitif n'a été développé jusqu'à présent pour interpréter de manière claire ces résultats et comprendre les mécanismes physiques à leurs origines. Dans un premier temps, des modèles d'oscillateurs harmoniques simples ont été utilisés mais ce type de modèle est souvent trop simpliste pour expliquer la riche physique de ces systèmes. D'un autre côté, des simulations numériques dans le régime fréquentiel [Sun13] avec des fréquences réelles ou dans le domaine temporel [Mar15] ont été réalisées mais ne permettent pourtant pas toujours d'avoir accès à la physique sous-jacente.

Dans le chapitre 4, nous proposons une nouvelle approche modale décrivant précisément la dynamique temporelle du champ diffusé par des nano-résonateurs. Cette approche, basée sur une expansion en modes quasi normaux (MQN) développée récemment dans le groupe, considère explicitement les modes résonants naturels de la structure [Sau13]. Les MQNs, dénotés par $\mathbf{E}_m(\mathbf{r})$, $m = 1, 2 \dots$ sont des solutions des équations de Maxwell en l'absence de source avec une fréquence de résonance complexe dont la partie imaginaire prend en compte les fuites et l'absorption du système. L'analyticité apportée par l'expansion en MQNs et la continuité dans le plan complexe permettent de décrire précisément la réponse spectrale de résonateurs plasmoniques autour de la fréquence de résonance. Dans le régime temporel, nous démontrons qu'une expression simple

$$\mathbf{E}_{sca}(\mathbf{r}, t) \approx \sum_m \beta_m(t) \mathbf{E}_m(\mathbf{r}),$$

où les coefficients d'excitation β_m sont connus analytiquement, conduit à une description très précise du champ $\mathbf{E}_{sca}(\mathbf{r}, t)$ diffusé par le résonateur. Nous appliquons cette théorie au calcul de la réponse temporelle de modes dipolaires brillants et de modes quadripolaires bien plus sombres et comparons nos prédictions à celles obtenues par la méthode "Finite-difference Time-Domain" (FDTD). Nous montrons que la prise en compte des modes naturels du système permet d'interpréter de manière très intuitive des résultats obtenus lors d'expériences de plasmonique ultra-rapide. La comparaison permet également de mettre en évidence que le formalisme

permet, si la réponse temporelle peut être décrite par seulement quelques modes dominants, de décrire très précisément la réponse au temps long, i.e. pendant la désexcitation, pour des temps de calculs extrêmement plus faibles que ceux de la méthode FDTD.

La méthode de calcul des MQNs développée dans le groupe repose sur une recherche itérative de pôles et ne permet de calculer que quelques MQNs dominants, nécessitant de plus un a priori sur la valeur du pôle. Pendant les 8 derniers mois de la thèse, nous avons travaillé sur la possibilité de calculer tous les MQNs d'un système donné, en un seul calcul et sans valeur initiale, en considérant une méthode basée sur des champs auxiliaires [Ram10]. Des résultats encourageants, qui ne sont pas présentés dans le manuscrit, ont été obtenus avec la nouvelle méthode de calcul et seront présentés pendant la soutenance.

Ce travail a été réalisé en collaboration avec le groupe d'Anders Mikkelsen (Université de Lund, Suède) qui a réalisé les calculs FDTD et fournit les données expérimentales.

----- Chapitre 5 -----

De récentes expériences [Aks14, Egg15, Kin09, Rin08] ont montré la possibilité d'obtenir de fortes augmentations de taux de d'émission spontanée ($\times 1000$) avec des efficacités d'émission relativement élevées ($> 50\%$) en plaçant des émetteurs quantiques dans des nano-fentes diélectriques à l'interface de deux objets métalliques. Ces résultats très surprenants sont obtenus pour des émetteurs placés à proximité du métal (quelques nanomètres) dans un régime où le quenching est considéré comme le canal de désexcitation dominant, empêchant a priori toute émission radiative de l'émetteur. La contradiction de ces observations suggèrent que les mécanismes physiques précis régissant l'émission d'émetteurs quantiques placés à proximité d'objets métalliques dans les nano-fentes diélectriques est toujours incomprise.

Dans le chapitre 5, nous clarifions comment de bonnes efficacités d'émission peuvent être obtenues malgré la proximité du métal et essayons de répondre à des questions fondamentales sur le rôle du quenching dans les antennes plasmoniques à nano-fentes. Nous discutons notamment du rôle primordiale d'un autre canal de désexcitation, le couplage aux plasmons lents de fentes, grâce à l'écriture d'une expression analytique du ratio entre couplage aux plasmons à fentes et quenching pour des systèmes planaires dans la limite de fentes fines. De manière intéressante, cette expression montre que l'émission dans les plasmons à fentes peuvent surpasser le quenching en choisissant de manière adéquate les permittivités des matériaux. A partir de la connaissance obtenue dans les systèmes planaires, nous quantifions les différents taux de désexcitation dans des antennes plasmoniques réalistes en modélisant leur comportement par des résonateurs Fabry-Perot.

Ce travail a permis une compréhension plus complète de la physique en jeu dans les antennes plasmoniques à fentes et donne une nouvelle vision pour la conception de systèmes plus efficaces. Ce travail a été publié en 2015 dans ACS Photonics et en 2016 dans Nanoscale Horizons.

ACKNOWLEDGEMENTS

Now that this three years adventure comes to an end, I would like to spend a few lines to warmly thank all the people who gave me this fantastic opportunity and helped me making it to the finish line.

The person that first comes to mind is my supervisor Philippe Lalanne to who I am truly grateful. His insatiable desire of understanding pushed me to go beyond what I thought was my possibility. Despite animated discussions and our respective strong personalities, I always enjoyed learning from you and valued your advices. I hope that it is not an end but a new beginning for our personal and professional relationship.

I would also like to thank Kevin Vynck who, in addition to his precious help during my PhD, always reassured me in periods of doubts.

I cannot forget other members of the group, Xiaorun Zang, Jianji Yang, Kévin Cognée, Wei Yan and Alexis Devilez, with who I shared daily during the last three years of my life. Thank you all for the intense discussions, ideas, opinions, but also for the relaxing moments.

Thank to Thomas Krauss's, Frédérique de Fornel's and Anders Mikkelsen's groups for the opportunity to collaborate on exciting projects and for the chance to learn always more. A special thank to Arthur Losquin who I recently met and with who I shared hours of discussions, by Skype or in conference, to make our project works.

I would also like to thank Jean-Paul Hugonin, for his constant and incredibly reactive support along those years, and Mondher Besbes, for his time and help in a new and exciting project.

This thesis would have not been possible without the contribution of my funding agencies, the "Direction Generale de l'Armement" (DGA) and the "Centre National de la Recherche Scientifique" (CNRS) to which I am grateful.

Finally, I would like to thank all my friends and family who lived this long journey by my side. No need to list all your names, or write how much I want to thank you and what you all mean to me. You know who you are and I will be showing you every day for as long as I can.

CONTENTS

Abstract	i
Résumé en français	iii
Acknowledgements	xi
Introduction.....	1
Chapter 1 - Implementing structural slow light on short length scales: the photonic speed-bump.....	15
1.1 Introduction	15
1.2 1D toy-model	16
1.3 Photonic-crystal speed bump	19
1.4 Speed bump LDOS.....	Error! Bookmark not defined.
1.5 Nature of the speed-bump resonance mode	26
1.6 Conclusion.....	28
Chapter 2 - Lower bound for the spatial extent of localized modes in photonic-crystal waveguides with small random imperfections	31
2.1 Introduction	31
2.2 Formation of localized modes at band edges.....	33
2.3 Computational method	37
2.4 Threshold in the size distribution of localized modes.....	38
2.5 Near-field observation of a wavelength-scale localized mode.	42
2.6 Conclusion	45
Chapter 3 - Hollow-core photonic crystal waveguide for remote and efficient couplings between atoms and waveguides	47
3.1 Introduction	47
3.2 Wide-slot photonic crystal waveguide design.....	49
3.3 Bloch mode properties.....	52
3.4 Figures of merit	54
3.5 Atom-photon coupling.....	56
3.6 Conclusion.....	58

Chapter 4 - Modal analysis of the temporal response of plasmonic resonators	61
4.1 Introduction	61
4.2 Theoretical Method	63
4.3 PEEM experimental data.....	66
4.4 Interpretation of the PEEM experimental data.....	68
4.5 Quantitative test of the modal formalism.....	71
4.6 Conclusion.....	77
Chapter 5 - Quenching, Plasmonic, and Radiative Decays in Nanogap Emitting Devices	79
5.1 Introduction	79
5.2 Decays on a single interface.....	82
5.3 Decays in dielectric nanogaps	83
5.4 Analytical expression of the decay rate in gap plasmons	87
5.5 Classification of nanogap emitting devices.....	91
5.6 Study of the nanocube antenna.....	93
5.7 Conclusion.....	97
Conclusion and Perspectives	99
Appendix 1: Computational method	105
Appendix 2: Fabry-Perot model for the description of the photonic speed bump	109
Appendix 3: Protocol for the calculation of individual localized modes..	113
Appendix 4: Wide-slot photonic crystal waveguide with full band gap mirror	115
Appendix 5: Convergence of the FDTD and temporal QNM-expansion methods	119
Appendix 6: Approximation on the dispersion in the temporal QNM-expansion	121
Appendix 7: Quenching calculation	123
Bibliography	127

INTRODUCTION

The last two decades have witnessed the rapid development of a new research field - nanophotonics - that comprises the studies of the interaction between electromagnetic fields with quantum objects or structured materials of characteristic size on the nanometer scale. Primarily this research has been encouraged by the high promises for miniaturization and processing rate enhancement of information and communication devices. This motivation has driven the study and development of new components for data storage and exchange such as waveguides, filters, buffers or optical switches [Kni96, Rab02, Xia07, Yan03]. However, the study of light-matter interaction at the nanoscale has expanded far beyond its initial goal and has conveyed many developments for sub-wavelength imaging [Spe92], new platform in quantum technologies [Lod15], sensing devices [Scu11], improvement in spectroscopy techniques [Nie97] energy harvesting in photovoltaic technologies [Atw10, Mok12] or sub-wavelength light sources [Oul09].

The large majority of applications emerging in nanophotonics essentially relies on the design of nanostructures that can resonantly interact with light to enhance light-matter interactions and to control field distributions at sub-wavelength scales. Accordingly, one fundamental quest has been the reduction of the confinement volume of light, i.e. the mode volume, to locally enhance the field intensity. The most common examples are undoubtedly dielectric microcavities. Their light trapping is achieved by surrounding highly reflective mirrors and the resonance originates from constructive interferences of the reflected waves [Vah03]. Those first attempts enabled to confine light in volumes of the order of the wavelength cube and to reach new regimes of light-matter interaction to achieve for instance strong coupling with atoms in quantum electrodynamics experiments [Ver98] or to

design filters for optical communications [Rab02]. More recently, new regimes of light confinement have been developed by exploiting metallic (i.e. plasmonic) nanostructures whose properties arise from their ability to support collective electron excitations, known as surface plasmons. Owing to their confinement at scales far beyond the diffraction limit in free space, metallic-based resonators have enabled to concentrate light in deep sub-wavelength volumes [Agi12, Sch10]. Although resistive heating losses in metals can severely limit the performance, many useful functionalities have recently been realized [Ada09, Liu11, Yu11].

An alternative route towards enhancing light-matter interactions is provided by structural slow light, i.e. light pulses that are slowed down by their interaction with a periodic arrangement along the propagation direction. Well-known examples are slow photonic-crystal waveguides formed by a periodic modulation of the refractive index [Joa08]. The highly dispersive nature of the mode sustained by periodic waveguides leads to the appearance of frequency ranges for which the group velocity is considerably reduced [Not01]. This phenomenon can be intuitively understood as resulting from the establishment of a standing wave, with a net flux close to zero, due to the interferences between forward- and backward-going waves within the structure. Due to energy conservation, the slowdown of light is accompanied by an increase of the field intensity proportional to the inverse of the group velocity [Boy11, Sol04]. In addition to dielectric periodic structures, nanogap-based plasmonic waveguides (also known as metal-insulator-metal (MIM) waveguide), in which thin dielectric layers are sandwiched between metallic claddings, also sustain slow light modes [Fer10, Yan12]. In those structures, the power flow in the tiny dielectric gap is compensated by a power flow in the metal (due to the electron motion) with opposite sign, giving a null total flow and thus creating slow plasmons. By combining a strong confinement and slowdown of light, nanogaps offer huge field enhancements, recently exploited for the design of new optical components [Aks14, Oul09].

The thesis mainly focuses on fundamental aspects and possible applications related to slow plasmons and structural slow light. Interestingly, they both share similarities that may inspire new understanding or new components. For instance, the photonic speed bump proposed and analyzed in chapter 1 is a perfect illustration of application in photonics of well known concepts in plasmonics. But some of their characteristics may also strongly differ as they originate from different physical processes. Hereafter, we briefly review their main properties, summarized as well in Fig. I-0.

As previously mentioned, structural slow light is usually implemented in periodic waveguides and originates from interferences between scattered waves in periodic structure. The characteristic dimension of the structure, i.e. the lattice constant a , therefore scales with the wavelength of interest $a \approx \lambda/(2n)$ with n the average refractive index. It immediately appears that structural slow light operates in a narrow frequency range. Importantly, in contrast to other kind of slow light obtained by nonlinearities in atomic-gas transition for instance [Boy11], structural slow light is associated to an enhancement of the field intensity. The enhancement in the slow light regime can be easily derived from Poynting's theorem. If one denotes by \mathbf{E}, \mathbf{H} the normalized electromagnetic field of an electromagnetic Bloch mode of a periodic waveguide, the Poynting's theorem stipulates that:

$$\frac{c}{n_g} \times \frac{1}{4a} \iiint_{period} (\epsilon_0 \epsilon |\mathbf{E}|^2 + \mu_0 \mu |\mathbf{H}|^2) dV = 1,$$

for a mode with a unitary power flow. The equality of the electric and magnetic energy density (the energy oscillates every half period from electric field energy to the magnetic field energy) directly implies that both the electric and magnetic fields scale proportionally to the square root of the group index, $\mathbf{E}, \mathbf{H} \propto \sqrt{n_g}$ (if one neglects any change of the spatial mode dispersion as n_g varies in the narrow spectral range of slowness). This important scaling law represents the building block for structural slow light applications, allowing a strong boost in light-matter interactions as exploited

in Chapter 3. However, the electric field enhancement represents also a huge limitation for the implementation of real devices as structural slow light suffers from enhanced backscattering by unavoidable fabrication disorder. This considerably limits the propagation length L_p ($L_p \propto n_g^{-1}$) and may even lead to light localization, as studied in Chapter 2.

Slow plasmons in nanogaps originate instead from sub- λ confinement and interaction of electromagnetic field with free electrons of metals. As a result, slow plasmons operate in the quasi-static limit and the characteristic dimension of the system, i.e. the gap size g , is much smaller than the wavelength ($g \ll \lambda$). Slow plasmons in nanogaps are thus inherently broad band. Interestingly, transition from fast to slow light regime is instead obtained by tuning the gap size, $n_g = \frac{\lambda^2}{g} \frac{\varepsilon_d}{\pi \varepsilon_m^2} \frac{\lambda \partial \varepsilon_m}{\partial \lambda}$ with ε_d and ε_m the relative permittivities of dielectric and metallic materials. Using the unconjugated form of Lorentz reciprocity theorem (the analog of the Poynting theorem for lossy media), one obtains for a normalized ($\iint (\mathbf{E} \times \mathbf{H}) \cdot d\mathbf{S} = 2$) gap plasmon

$$\frac{c}{n_g} \times \frac{1}{4} \iint \left(\varepsilon_0 \varepsilon (E_x^2 + E_y^2 - E_z^2) + \mu_0 \mu (H_x^2 + H_y^2 - H_z^2) \right) dS = 1,$$

with n_g a complex number due to absorption. For subwavelength gap sizes, the energy oscillates between the electric energy and the kinetic energy sustained by free electrons while the magnetic energy becomes negligible [Khu15]. This energetic considerations lead to a different scaling law, $\mathbf{E} \propto n_g$ and $\mathbf{H} \propto Cte$. As discussed in Chapter 5, the increase of the electric field with the group index may be for instance exploited for enhancing coupling to quantum emitters and the design efficient plasmonic structures. Nevertheless, the electron motion is inevitably accompanied by absorption and the propagation length $\frac{\lambda}{2\pi \times \text{Im}(n_{eff})}$, $n_{eff} = \varepsilon_d \lambda / \pi \varepsilon_m g$, considerably reduces as the gap size shrinks. The propagation length scales, as for the case

of structural slow light, as n_g^{-1} , but this damping originates from a completely different physical process.

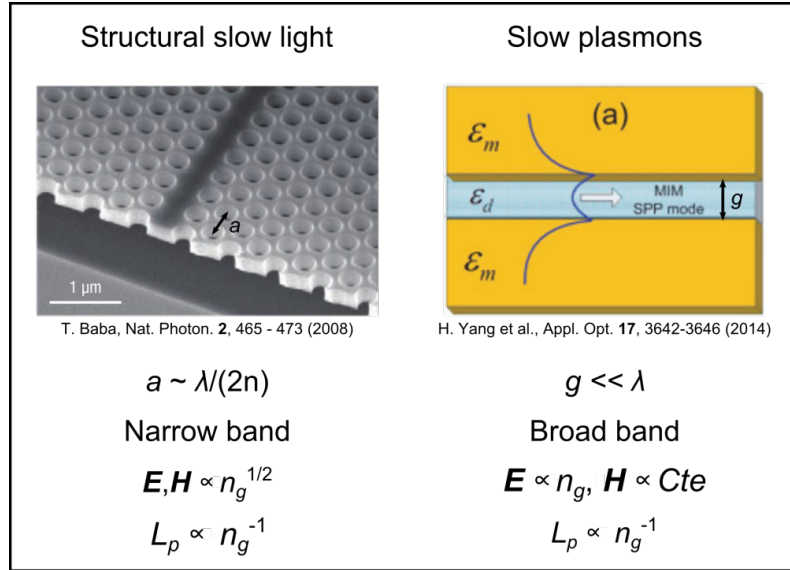


Figure I-0. Structural slow light and slow plasmons.

Overall, structural slow light and slow plasmons, thanks to their propensity to reinforce the interaction between light and matter, have led to numerous developments in photonics and in other domains of sciences and technologies; yet, a lot remains to be discovered ...

Throughout the manuscript, structural slow light and slow plasmons have been studied and this thesis, articulated in 5 *independent* chapters, investigates both fundamental and applied aspects related to these physical phenomena.

----- Chapter 1 -----

One-dimensional (1D) infinite periodic systems exhibit vanishing group velocity and diverging density of states (DOS) near band edges. In practice, however, systems have finite sizes, which inevitably prompts the question of whether physical quantities related to infinite systems, such as the group velocity that is deduced from the band structure, remain relevant in finite systems. For instance, an interesting aspect is to understand how the DOS

divergence can be approached in systems with finite size and if the implementation of larger and larger DOS (or equivalently smaller and smaller group velocities) relies on a considerable increase of the structure length, as it may intuitively be expected.

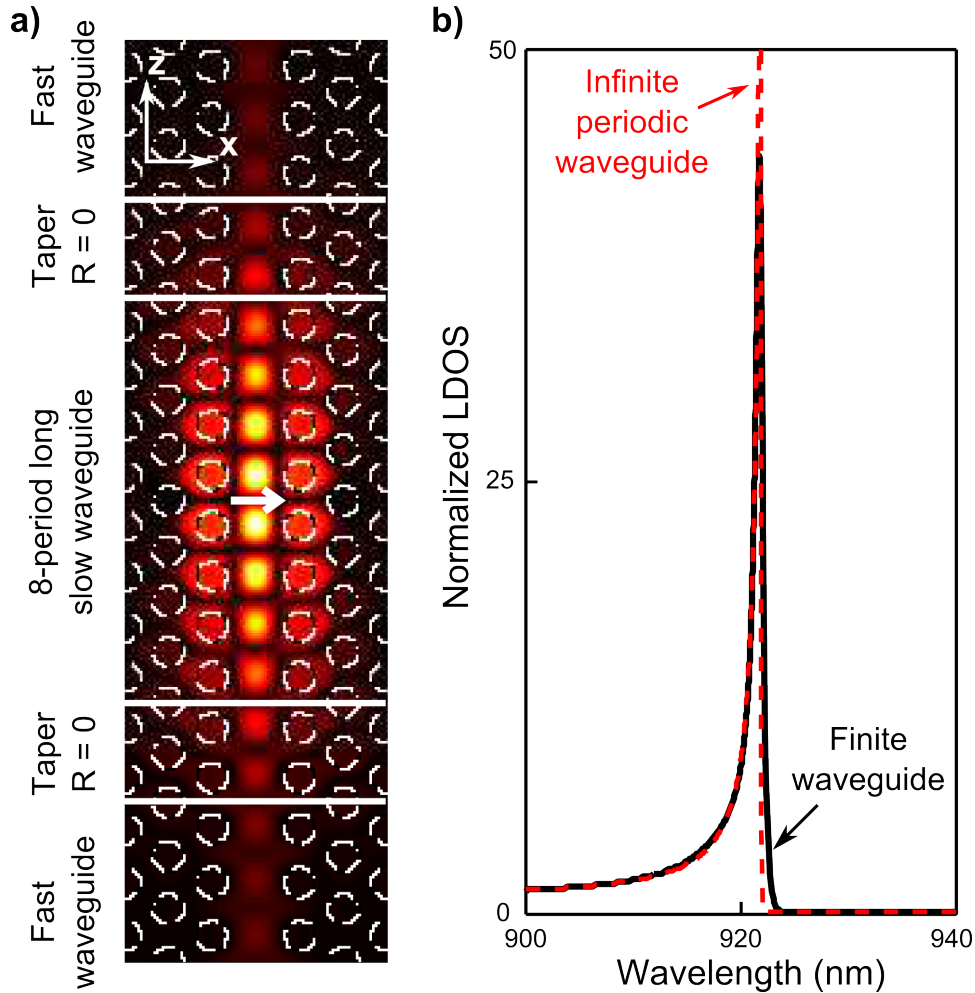


Figure I-1. Implementation of slow light effect in short nanostructures with a photonic speed bump. **a)** Schematic of the speed bump and field profile. The speed bump is composed of a N -period long slow waveguide (here $N = 8$) surrounded by perfectly transparent tapers, working at their optimized frequency (here corresponding to $n_g = 100$), and semi-infinite fast waveguides. The field map represents the absolute value of the y -component of the magnetic field excited by an electric dipole source (white arrow) emitting at the frequency corresponding to $n_g = 100$. The light emitted by the dipole slowly propagates in the slow waveguide and is perfectly expelled in the fast waveguides. **b)** Normalized LDOS (solid black) seen by the x -polarized source placed in the center of the speed bump shown in (a). The red dashed curve corresponds to the LDOS achieved for a fully-periodic, infinite slow-W1 waveguide (Van Hove singularity). As evidenced, the speed-bump well reproduces the DOS of the infinite waveguide up to $n_g = 100$.

In chapter 1, based on general 1D-wave-physics arguments, we demonstrate that the large slow-light DOS enhancement of periodic systems can in fact be observed with very short systems, whose lengths scale with the logarithm of the inverse of the group velocities. The understanding obtained in 1D leads us to propose a totally new family of photonic micro-resonators, photonic analogues of speed-bumps, in which the electromagnetic energy accumulates, similarly to plasmonic nanofocusing devices, not because of a resonant recirculation between two mirrors, but because of a sudden reduction of the group velocity, followed by a reciprocal acceleration to go back to the initial speed (see Fig. I-1a). 3D simulations conclusively support that short systems may mimic the slow-light DOS enhancements of infinite systems even for very small group velocities (see Fig. I-1b). In addition, we show that the DOS enhancements of speed bumps result from a classical electromagnetic resonance characterized by a single resonance mode and that the nature and properties of the resonance are markedly different from those of classical defect-mode photonic-crystal cavities.

----- Chapter 2 -----

Initial studies on light transport in periodic waveguides have shown that fabrication imperfections have significant impacts on slow light transport and impose important limitations on the realization of slow light photonic devices [Mel14, Not01]. The most striking phenomenon is undoubtedly the formation of localized modes at band edges, generally explained by the enhanced sensitivity of light to randomly-distributed defects at small group velocities [Mel14]. However, the analysis of the spatial extent of localized modes is missing, especially regarding the smallest confinement which provides an upper bound of the longest propagation delay that can be implemented for a given technology, i.e. for a given level of fabrication imperfection.

In chapter 2, we investigate the impact of residual fabrication imperfections in slow light periodic waveguides on the formation of highly-

localized modes, with the ambition to understand the key parameters driving their spatial extent. From an experimental side, we show that highly-confined states are naturally formed at the band-edges of photonic-crystal waveguides manufactured without any intentional disorder, just with the intrinsic imperfections of the fabrication technology (1 nm perturbations @ $\lambda = 1.5\ \mu\text{m}$). Our experimental observations, conducted in Frédérique de Fornel's group in Burgundy University, reveal that the smallest confined modes that naturally form have mode volumes equal to a few wavelengths cube (see Fig. I-2). This surprising result raises fundamental questions on how almost perfect waveguides with tiny defects of $\approx 1\text{ nm}$ may so profoundly impact light transport. As mentioned above, the group velocity is known to be a key parameter for localization near photonic band edges, since small group velocities reinforce light interaction with imperfections. In contrast with previous works, we show that the size of the smallest localized modes is instead driven by the effective photon mass, i.e. the flatness of the dispersion curve. Additionally, we demonstrate that photonic-crystal waveguides, owing to their large effective mass compare to other 1D periodic systems such as Bragg stacks, may indeed support wavelength-scale localized modes whose sizes are in agreement with the experimental observations.

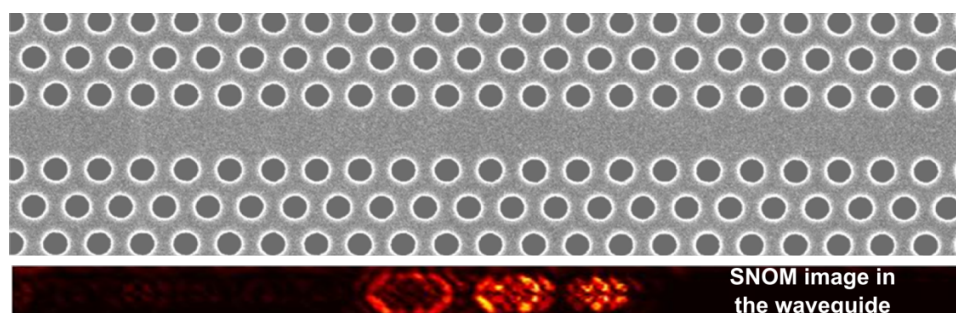


Figure I-2. Measurements of wavelength-scale localized modes with residual disorder in photonic crystal waveguides. The top image shows a SEM of the photonic-crystal waveguide we have studied. Although the waveguide seems almost perfect, highly localized states have been observed with near-field optics in Frédérique de Fornel's group in Dijon, see the bottom image.

The work was conducted in close collaboration with Thomas Krauss's group in York University and Frédérique de Fornel's group in Burgundy University. The former fabricated state-of-art photonic crystal waveguides and the latter carried out the near-field experiments. The fruitful collaboration led to a publication in 2016 in Scientific Reports. The article provides details on the fabrication procedure and the near-field measurement techniques which are not discussed in the chapter.

----- Chapter 3 -----

The emerging field of on-chip integration of nanophotonic devices and cold atoms offers extremely strong and pure light-matter interaction schemes, which may have a profound impact on quantum information science [Kim08a]. In this context, a long-standing obstacle is to achieve a strong interaction between single atoms and single photons while simultaneously trapping atoms in vacuum at distances large enough from the dielectric waveguide to avoid Casimir-Polder forces. To date, the evanescent nature of the electric field in vacuum, whose amplitude rapidly decreases with distance, limits the separation distance and prevents easy implementations of atom-photon coupling in nanostructures.

In chapter 3, we design a slotted photonic-crystal slow-light waveguide that achieves enhanced light-matter interaction far from the nanostructure (see Fig. I-3). We engineer the modal properties of a guided Bloch mode in order to reach a strong electric field in a $1\mu\text{m}$ -large gap, much larger than that of previous slot waveguides, usually limited to widths of about two hundred nanometers [San07, Hun13]. The field enhancement is achieved thanks to a slower decay of the evanescent field in vacuum, combined with a slowdown of light. The design embraces two conflicting issues: on the first hand, the light has to be deconfined in vacuum, and therefore it should weakly interact with the periodic structure. On the other hand, implementing slow light requires a strong interaction between the light and the refractive index modulation. To circumvent this issue, we propose a new type of

waveguide with two commensurate periodicity, which allows to tailor flat dispersion curves at (ω, k) very close to the light line of the air clad. Figure I-3 shows the Bloch mode field in a transverse section of the waveguide and its geometry.

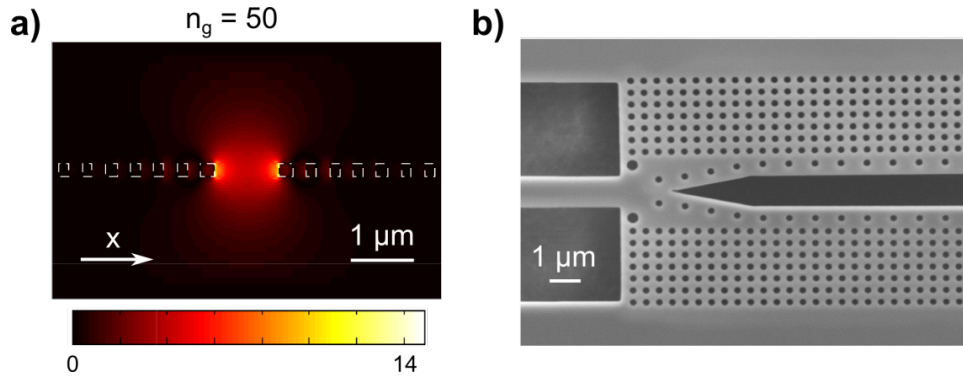


Figure I-3. Slow-light waveguide for enhanced light-interaction in air. a) Cross-sectional view of the x-polarized electric field amplitude in a wide slot waveguide for a frequency corresponding to a group index of 50. The field is extremely intense in the air region. **b)** First fabrication in Thomas Krauss's group of the wide slot waveguide using e-beam lithography.

----- Chapter 4 -----

The field of ultrafast plasmonics is constantly growing for the last decade thanks to the development of new experimental tools for observing light-matter interaction with nanometric precision at femtosecond timescales. However, no intuitive or simple theoretical tool has been developed so far to clearly interpret experimental measurements and unravel the physical processes at their origins. On one side, damped harmonic oscillator models have been used but it is often too simplistic to embrace all the rich physics. On the other hand, numerical brute-force simulations have been carried out either in the spectral domain [Sun13] with real frequencies or in the time domain [Mar15] but a clear insight on the underlying physical processes is not always granted.

In chapter 4, we propose a novel modal approach that accurately describes the temporal dynamics of the field scattered by resonators. The approach is based on a quasi-normal-mode (QNM) expansion recently

developed in our group, which explicitly considers the natural resonant modes of the structure [Sau13]. The QNMs, denoted by $\mathbf{E}_m(\mathbf{r})$, $m = 1, 2, \dots$, are solutions of Maxwell's equations in the absence of a source with complex resonance frequencies whose imaginary part accounts for leakage and absorption. The analyticity brought by the QNM expansion and the continuation in the complex plane allows us to accurately describe the spectral response of plasmonic nanoresonators around the resonance frequency. In the temporal regime, we demonstrate that a very simple expression

$$\mathbf{E}_{sca}(\mathbf{r}, t) \approx \sum_m \beta_m(t) \mathbf{E}_m(\mathbf{r}),$$

where the excitation coefficients β_m 's are known analytically, leads to very accurate predictions of the field $\mathbf{E}_{sca}(\mathbf{r}, t)$ scattered by plasmonic nanoresonators. We apply this theory to calculate the temporal response of bright dipolar and much darker quadrupolar plasmonic modes and compare the theory predictions with numerical data obtained with the FDTD method. We show that, since it intrinsically relies on the natural resonances of the systems, the QNM theory provides unprecedented intuitive clues for interpreting ultrafast nanoplasmonic experiments. The comparison additionally evidences that, provided that the temporal response is well described by a few dominant resonance modes, the formalism leads to highly-accurate predictions (see Fig. I-4) of the long time behavior, with CPU times considerably smaller than the FDTD ones.

The QNM solver that has been developed in the group relies on an iterative pole search [Bai13] and can calculate only a few dominant QNMs in reasonable time, provided that accurate guess values for the poles exist. During the last 8 months of the PhD work, we have investigated the possibility to calculate all QNMs with a single computation (no preconditioning) by considering the auxiliary-field method [Ram10]. Encouraging results, not reported in the thesis, have been obtained with the new QNM solver. They will be presented during the defense.

The work was realized in collaboration with Anders Millelsen's group (Lund University, Sweden), which carried out FDTD calculations and provided experimental measurements.

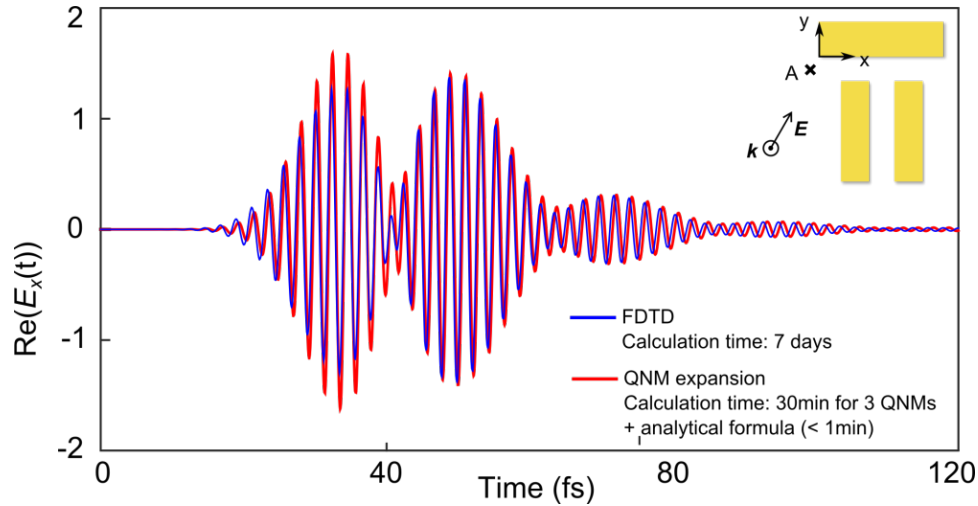


Figure I-4. Temporal dynamic responses computed at point $A = (-5, -10, 0)$ nm of a gold dolmen [Zha08], see sketch in the upper-right inset, illuminated by a 12.7-fs Gaussian driving pulse polarized along the $\hat{x} + 2\hat{y}$ direction. (blue) FDTD computational results and (red) QNM-expansion formalism. Calculation time for the FDTD method is about 7 days. The QNM method requires the calculation of the dominant modes (here 3 modes are considered for a total calculation time of 30 min). Since the β_m 's are known analytically, the CPU time to compute the temporal response for another driving field, with a different polarization, incidence angle or pulse duration for instance, is negligible. With the FDTD the entire calculation should be re-performed for every driving field. Note that the discrepancy between the FDTD and QNM results at long times is due to a numerical dispersion of the FDTD.

----- Chapter 5 -----

Recent experiments [Aks14, Egg15, Kin09, Rin08] have shown the possibility to significantly increase the spontaneous emission rate ($\times 1000$) with relatively good radiative efficiencies ($> 50\%$) by burying quantum emitters in tiny nanogaps at the interface of two metallic objects. This result comes as a surprise as quantum emitters in close proximity to metallic objects (a few nanometers) are in a regime where quenching is considered as the predominant decay channel, preventing any radiation. Those contradictory results suggest that the precise physical mechanisms that drive the emission

of quantum emitters placed very close to metal surfaces in tiny gaps are not well understood.

In chapter 5, we clarify why good efficiencies are achieved despite the proximity to the metal, and try to respond to fundamental questions on the importance of quenching in nanogap antennas. Using analytical derivations and a simple emission-rate model (Fig. I-5), we show that a competing decay channel, the coupling to slow gap plasmon polaritons, exists in nanogaps and provide analytical expressions for the branching ratio between gap plasmon decay and quenching in the small gap limit. Interestingly, the expressions evidence that gap-plasmon decay may overcome quenching for tiny gaps by solely choosing properly the materials permittivities. From the understanding gained in planar systems, we then study the decay rates in realistic nanogap antennas by modeling the antenna behavior as a Fabry-Perot resonator.

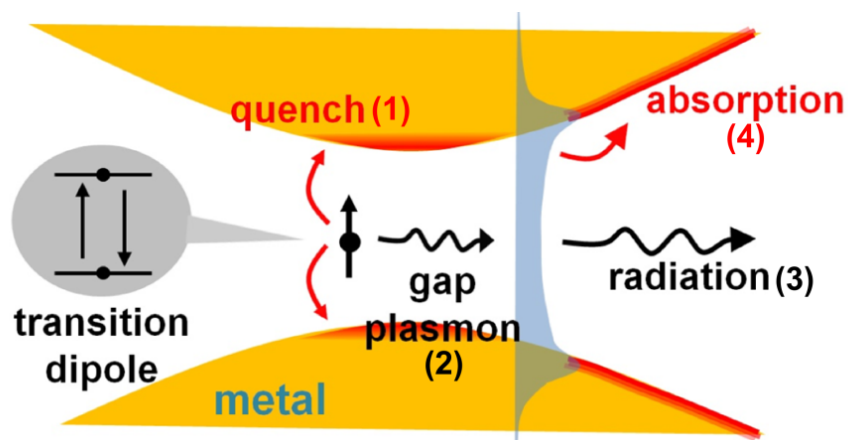


Figure I-5. Schematic representation used in chapter 5 for modeling light emission in tiny gaps. (1) Near-field non-radiative decay (quenching) at rate γ_{quench} of the emitter into the metal; (2) excitation of gap plasmons at rate γ_{GSP} ; (3) conversion of the excited plasmons into free space photons at rate γ_{rad} ; (4) plasmon decay into metal at rate γ_{abs} .

The work enables a more complete understanding of the physics at play in nanogap-based nanoantennas and provides insight on the design of more efficient systems. It was published in ACS Photonics in 2015 and Nanoscale Horizons in 2016.

Chapter 1 - IMPLEMENTING STRUCTURAL SLOW LIGHT ON SHORT LENGTH SCALES: THE PHOTONIC SPEED-BUMP

1.1 Introduction

Introducing a 1D periodic modulation into an initially uniform wire results in a bandgap opening and a redistribution of the states that cluster at the band edge, leading to a divergence of the density of states (DOS), known in solid-state physics as the Van Hove singularity [Ash76]. The DOS singularity and the related group-velocity reduction have important consequences in optics. They are responsible for the feedback mechanism in distributed-feedback solid-state lasers [Dow94, Xue16], help implementing nonlinear processes [Cor09, Sol02, Bar09a], enhance the mode lifetimes of photonic-crystal cavities [Ben96, Lal08] and the sensitivity of optical sensors [Scu11, Dic12], and serve as key building blocks for interfacing light with atoms for a range of applications in photonic quantum-information processing [Gob14, Gob15].

The singularity (Fig. 1-1a) exists only in infinite systems, meaning that an infinite number of unitary cells are required to build it up. Intuitively, if one assumes that a resonance state can be attached to every individual cell or a few cells, the singularity is seen as originating from a coherent superposition of an infinite number of resonance states, which are all phase-matched and form a Bloch state with a null group-velocity at a precise frequency. However, no structure is strictly periodic and in any real device, e.g. photonic-crystal cavities [Not10], single photon sources [Lod15], lasers [Mor14], slow waves are reflected at the device termination and since the reflectivity considerably increases as the group velocity vanishes [Cot72], only very weak reminiscences of the DOS singularity are observed.

Slow-light DOS enhancements are always entangled with other cavity-like DOS effects [Ben96, Cot72, Lal08, Kra16a, Moo08, Atl10], so that the Van Hove singularity of infinite media is an abstract concept only. Despite the ample literature on slow-light-assisted spontaneous-emission rate in periodic waveguides and cavities [Lod15], it is not clear if the DOS enhancement associated to given slowness can be observed in a finite-length structure, especially for large slowness. Nor it is evident what is the minimum number of cells required to experience the slowness, or how close can one approach the DOS singularity with a finite structure. The goal of this work is to provide the answers to these questions and to propose a new structure to observe slow-light DOS enhancements.

We first consider 1D periodic systems. Based on general wave-physics arguments, we explain how to engineer the impedance at the system terminations to achieve slow-light DOS enhancements on very short lengths that scale with the logarithm of the inverse of the group velocities, the group index. Then in a second step, capitalizing on the mature knowledge recently gained on photonic-crystal (PhC) waveguides, we validate the previous general considerations with realistic designs. This leads us to propose a totally new family of photonic micro-resonators, photonic analogues of speed-bumps, in which the electromagnetic energy accumulates, not because of a resonant recirculation between two mirrors, but because of a sudden reduction of the group velocity, followed by a reciprocal acceleration to go back to the initial speed. 3D simulations of the transmission and DOS enhancement conclusively support that short systems may mimic the slow-light DOS enhancements of infinite systems even for very small group velocities.

1.2 1D toy-model

Let us start by considering a 1D periodic system (Fig. 1-1a) composed of alternating layers of high and low indices for instance. In 1D, only a single

pair of counter-propagating Bloch modes, either evanescent (in the gap) or propagative (in the band), exists, and the DOS exhibits the classical $(\omega - \omega_0)^{-1/2}$ divergence at the band edge ω_0 . For a periodic system of finite length L , Bloch modes are back-reflected at the terminations, the singularity is smoothed and the DOS in the bandgap is no longer zero [Yeg14]. Intuitively, if one assumes that the momentum space is typically sampled with a resolution of $1/L$ because of the finite length, one expects to observe group velocities v_g that scales inversely proportional to the system length, $v_g \propto 1/L$, see Fig. 1-1b.

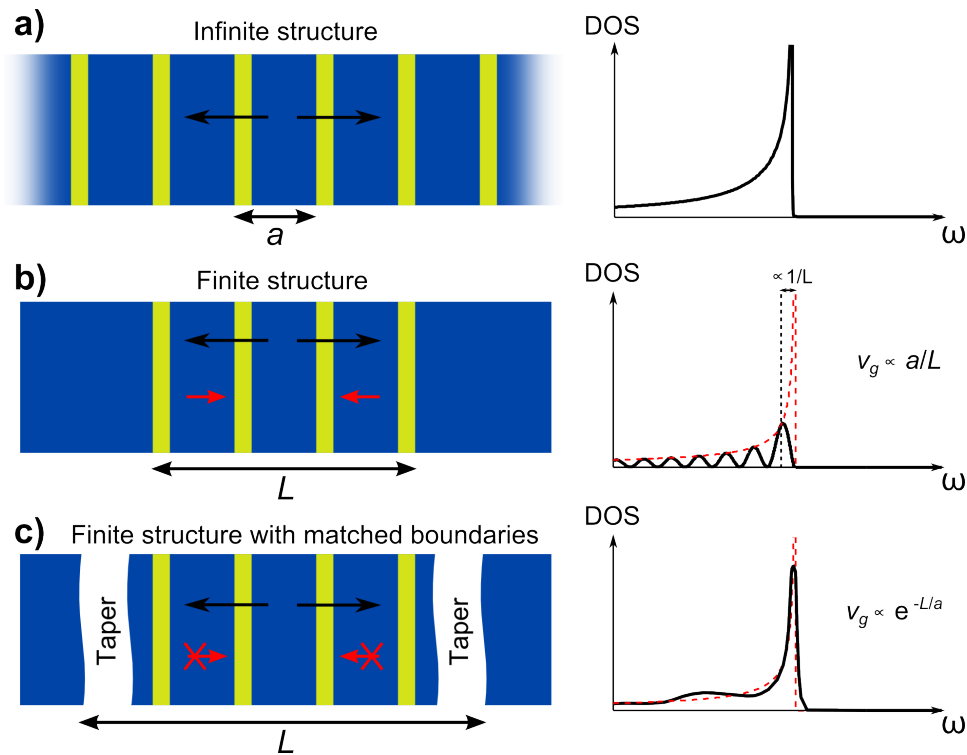


Figure 1-1. Mimicking periodic infinite media with finite periodic media. **a)** 1D infinite periodic medium: the source couples to outgoing Bloch modes (black) that propagate away without any reflection. **b)** 1D finite system: the Bloch modes are back-reflected on the terminations and modify the field distribution inside the periodic structure. **c)** 1D finite periodic medium with perfectly matched boundaries (tapers): the Bloch modes are not reflected on the boundaries and the source sees an infinite periodic medium. **a)-c)** The right insets sketch the corresponding DOS.

Actually, much shorter length scales can be achieved with suitably engineered terminations. The local DOS can be evaluated by considering to

the total power radiated by a Dirac dipole source at a working frequency ω . The radiation mechanism in 1D is very simple. The source, a 2D current sheet, excites the two counter-propagative Bloch modes existing at ω . The modes propagate until they reach the terminations. Thus if the terminations are equipped with tapers whose impedance matches the slow Bloch modes with the fast modes of the surrounding medium (Fig. 1-1c), no back-reflection occurs at the terminations. The tapers act as trompe-l'oeil that mimics the infinite system: the source sees the same impedance in the finite or infinite systems and radiates identically.

Counter-intuitively, our simple reasoning also suggests that the number of periods of the finite-length crystals is unimportant, and might be 1,2 or many, since there is no back-action of the termination on the source. Thus answering our initial question of how many cells are required to experience a given slowness v_g amounts to answer what is the minimum length required to *perfectly* bridge the impedance mismatch between a slow Bloch mode and a fast mode. Adiabatic tapers based on a gradual variation of the geometry could be a first alternative [Ste02]. Such tapers have the advantage to offer broadband operation and to conform to any kind of waveguide geometries, but their lengths may become prohibitively long at small v_g 's. For 1D systems, it is possible to design much shorter tapers. By assuming that slow-Bloch modes of 1D periodic media are stationary patterns locally formed by two counter-propagating plane waves, *perfectly-matched* tapers formed by a combination of a phase plate and a quarter-wave stack can be designed at any arbitrarily-small v_g [Vel07]. Such tapers are not broadband, but interestingly offer small lengths that scale with the logarithm of the group index, $L \sim \log(n_g)$ with $n_g = c/v_g$. This implies that perfect matching at $n_g = 10^4$ for instance is achieved with a taper length as small as four quarter-wave periods.

Albeit simplistic, the 1D toy model suggests that the DOS enhancement at the band edge of periodic media, which is generally attributed to slow Bloch

modes in infinite media, may be recovered in a very short length scale, $L \propto \log(n_g)$. In a different point of view, one may illuminate the tapered system from outside with a plane wave, rather than with an internal source. The structure then can be seen as the analogue of a "speed-bump" for photons. The light propagating at large group velocity in the surrounding medium is first slowed down in the taper and then propagates at slower group velocity in the periodic system, before being reaccelerated in the second taper and escaping in the surrounding medium on the opposite side. Indeed, the perfectly-matched impedance ensures a complete transmission at the working frequency ω .

Structural slow light has many applications in science and technology, from delay lines [San12], pulse compression [Kon15] and sensors [Scu11, Dic12] to single-photon components for quantum information [Lod15]. Hereafter, we implement the concept of photonic speed bumps, developed in 1D, with the aim to design a manufacturable photonic structure that potentially offers new properties.

1.3 Photonic-crystal speed bump

We will rely on the mature photonic crystal (PhC) waveguide platform to study the optical properties of realistic speed bumps. A schematic of the proposed speed-bump is shown in Fig. 1-2. A finite-length N -period-long slow-W1 waveguide (with one row of holes missing in the ΓM direction of the photonic lattice) is bridged, by two tapers, to two semi-infinite fast-W1 waveguides obtained by slightly elongating the period of the slow-W1 waveguide in the longitudinal direction. This structure will be referred to as the N -period long speed bump. The geometrical parameters of the waveguides are given in the caption of Fig. 1-2.

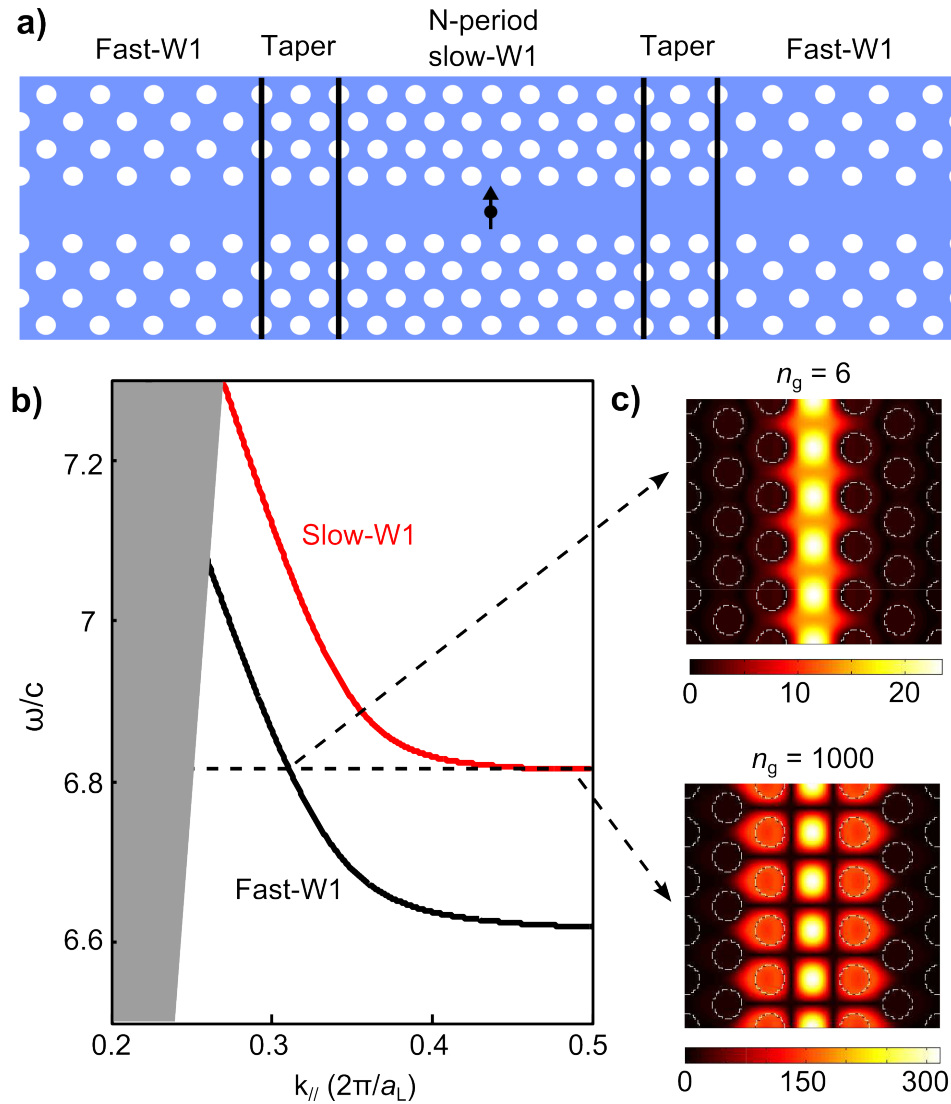


Figure 1-2. Photonic-crystal speed bump. **a)** Schematic of an N -period-long speed bump, composed of an N -period-long slow-W1 waveguide surrounded by bilayer heterostructure tapers and fast-W1 waveguides. The waveguides are assumed to be etched in a membrane of thickness 220nm and refractive index 3.45. The 2D photonic crystal mirrors of the slow-W1 waveguide are made of a triangular lattice of air holes of periodicity $a = 232\text{nm}$. The fast-W1 waveguide is obtained by stretching the longitudinal period of the slow-W1 waveguide from $a = 232\text{nm}$ to $a_L = 245\text{nm}$, the transverse period being unchanged. **b)** Dispersion curves of slow-W1 (red) and fast-W1 (black) waveguides. The operating frequency is marked with a black horizontal dashed line. **c)** Amplitude of the y -component of the magnetic field of the slow-W1 ($n_g = 1000$) and fast-W1 ($n_g = 6$) Bloch modes at the operating frequency. The modes are normalized to carry a power flow of 1.

Hereafter, the theoretical analysis is performed with a 3D fully-vectorial Fourier-modal method [Lec07a], which relies on an analytical integration of Maxwell's equations along the waveguide direction through a Bloch mode expansion of the field. The method has already been successfully applied to accurately analyze various scattering problems in photonic crystal waveguides and in sequences of them, see [Hug07, Fag16] for instance. More details on the computation method can be found in Appendix 1.

The dispersion curves of the slow- and fast-W1 Bloch modes are plotted in Fig. 1-2b. In the spectral range of interest, close to the band edge of the slow-W1 waveguide marked by the horizontal black dotted line, the waveguides are monomode. The slow-W1 waveguide exhibits a small group velocity, while the fast-W1 waveguides exhibit rather large and nearly constant group velocity $c/6$. Figure 1-2c shows the normalized amplitude of the y -component of the magnetic field in the median plane of the membrane at $\omega/c = 6.816\mu\text{m}^{-1}$, $n_g = 6$ and 1000 for the fast- and slow-W1 waveguides respectively. The mode profiles and amplitudes are sharply distinct due to the group-velocity impedance mismatch. We note that the fast-W1 waveguides may be replaced with other types of waveguides, e.g. ridge waveguides; the choice just impacts the taper design, but not the principle of operation of the speed bump.

The impedance mismatch leads to large modal reflectance at the interface between the slow- and fast-W1 waveguides, see the black curve in Fig. 1-3b. Thus the PhC speed-bump design relies solely and critically on our ability to suppress this impedance mismatch with effective tapers that match the fast- and slow-W1 waveguides to mimic an infinite slow-light system. To design effective tapers for coupling to slow-light PhC waveguides, several geometries and optimization techniques can be considered [Osk12, Scu14]. Hereafter, we follow the approach in [Hug07].

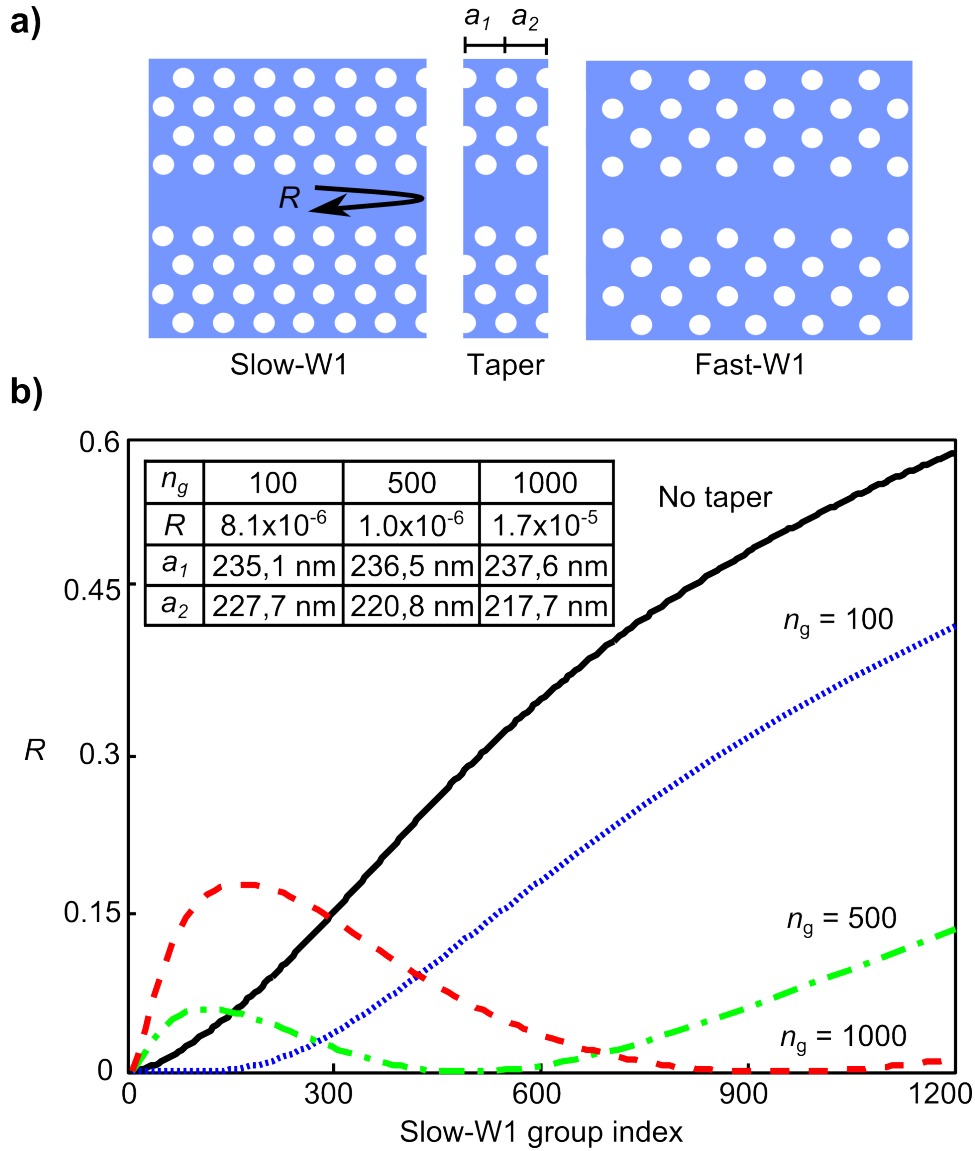


Figure 1-3. Taper optimization. a) Taper layout. A slow-W1 waveguide is connected to an elongated fast-W1 waveguide through a bilayer-heterostructure taper, which is optimized by tuning the longitudinal periods a_1 and a_2 of the two layers. b) Reflectance of the tapered interface for 3 tapers optimized for $n_g = 100$ (dotted blue), 500 (dotted-dashed green) and 1000 (dashed red). The solid black curve shows the reflectance without taper. Inset: Minimum taper reflectance and taper geometrical parameters.

Figure 1-3a shows the taper geometry. The latter is composed of a bilayer-heterostructure formed from the slow-W1 waveguide by slightly varying the longitudinal periods, a_1 and a_2 . Similar bilayer tapers have been previously used to design remarkably-short and effective couplers with 2D computational results [Hug07], and have been used in many slow-light

experiments afterwards [Arc14, Cor09, Lod15]. The following numerical results are obtained with a 3D fully-vectorial method that takes into account scattering into the air clads. They evidence that the bilayer geometry is versatile since it allows us to design effective tapers from $n_g = 4$ up to 1000.

Figure 1-3b shows the performance of 3 tapers optimized for 3 target group indices, $n_g = 100$ (dotted-dashed green curve), 500 (dotted-blue curve) and 1000 (dashed-red curve), respectively. In contrast with the abrupt interface case (no taper), the reflectance shows a markedly different behavior with a nearly-zero reflectance around the targeted n_g . Additionally, the calculations shows that the scattering in the cladding is negligible and that the transmission is equal to $1-R$ with a very good approximation ($1-R-T = 0.012$ for $n_g = 1000$). Although compactness comes at a price of narrowband operation, the ultra-short bilayer-heterostructure taper provides a very effective approach to reduce the impedance mismatch and to mimic an infinite system on short length scales. Also, it is worth noting that, the taper design presented here is just a proof-of-concept demonstration. Tapers with more than two periods and/or other intricate topology [Ben03] may be designed to achieve even better performances, in terms of, e.g., bandwidth, target group index, and tolerance to fabrication imperfection.

1.4 Speed bump LDOS

The capability of PhC speed bumps to mimic the DOS singularity is analyzed by computing the local DOS, or LDOS, seen by an x -polarized electric dipole (small arrow in Fig. 1-2a) placed in the center of the PhC speed bump. This quantity, normalized by the emission of the same dipole in the bulk, is commonly known as the Purcell factor. Figure 1-4 shows the normalized LDOS for a long speed bump ($N = 8$) for the optimized tapers of Fig. 1-3. For comparison, we also show the LDOS of the same emitter placed in an infinite

slow-W1 waveguide (black dotted curve showing the van Hove singularity) and in a speed bump without taper (black solid curve).

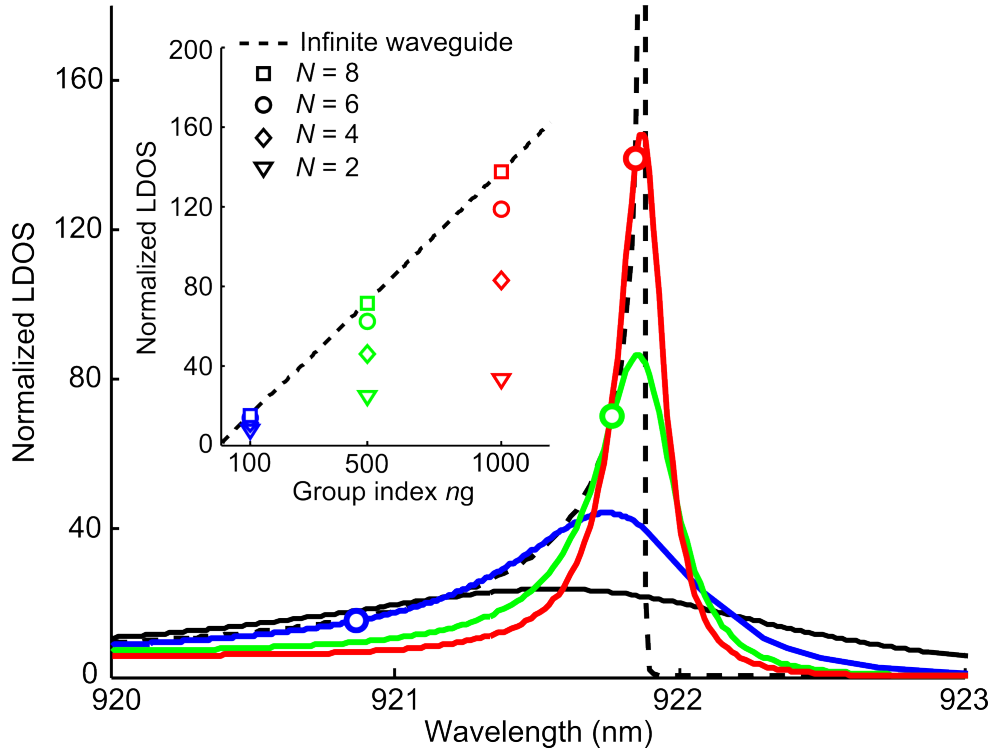


Figure 1-4. Mimicking the van Hove singularity with PhC speed bumps. Normalized LDOS (or Purcell factor) seen by an x -polarized source placed in the center of a 8-period-long speed bump optimized for operation at $n_g = 100$ (blue), 500 (green), 1000 (red) and without taper (black). The black dashed curve corresponds to the LDOS achieved for a fully-periodic, infinite slow-W1 waveguide (Van Hove singularity). The blue, green and red circles highlight the Purcell values achieved by the speed bump at their nominal operation wavelengths for which the taper reflectance is almost null. Importantly, the dots are almost superimposed with the black dashed curve, evidencing that the source emitting in the speed bump emits as if it were in a fully periodic waveguide. Inset: Evolution of the Purcell factor with speed bump length Na for the same three optimized tapers at $n_g = 100, 500$ and 1000.

The results evidence that the LDOS is substantially enhanced by tapering and that the enhancement is stronger for speed bumps with tapers that are designed for high group indices. We also note that the LDOS is not null in the gap of the slow-W1 waveguide, simply because of the tunneling effect associated to the evanescent gap Bloch modes that are not perfectly matched at the interface. More interesting are the LDOS enhancements achieved by the speed bumps at every target group indices. The enhancements are

highlighted by circle markers. It is noteworthy that all markers are superimposed with the black-dashed curve obtained for the truly infinite slow-W1 waveguide, implying that the tapers act as a trompe-l'oeil at their target group indices and that the source therefore emits as if it were experiencing the LDOS of the fully periodic structure. This observation fully validates the possibility to mimic, at least in a narrow spectral band, the DOS of infinite periodic systems up to $n_g \approx 1000$ with compact systems with lengths of a few periods.

The inset of Fig. 1-4 displays the LDOS enhancements achieved at the target group indices for several values of the speed-bump length N . In contrast with the predictions of the 1D toy-model, the normalized LDOS vary with N . Further computations, not reported here, have shown that the LDOS at the target group index remains stable for $N > 8$. Unlike 1D thin-film stacks, PhC waveguides support, in addition to the guided Bloch modes, a few evanescent Bloch modes [Hug07]. The source emission feeds all the modes. The latter propagate outward until reaching the tapers, where they scatter back (only the truly guided Bloch mode is fully transmitted) and potentially excite the inward-propagating guided Bloch modes, resulting in a back-action on the source. Overall, these intricate scattering processes involving evanescent Bloch modes not considered in 1D systems may lead to a substantial change of the LDOS, preventing the observation of a mere signature of the slow-light LDOS enhancement. However, when the slow-W1 section length increases, the impact of radiation modes fades away as they effectively lose their energy by radiation before reaching the taper. Similar conclusions may be obtained by using a Fabry-Perot model, presented in Appendix 2, that quantifies the sole contribution of the propagating Bloch mode in the Purcell factor.

1.5 Nature of the speed-bump resonance mode

In classical defect-modes PhC microcavities [Not10], the resonance modes are essentially Fabry-Perot resonances formed by the bouncing back and forth of light in a region surrounded by two high- R mirrors. In the speed bump, the trapping mechanism is different. The electromagnetic energy accumulates because of a sudden and drastic reduction of the light group velocity from $c/6$ to $c/1000$, followed by a reciprocal acceleration to go back to the initial speed. The accumulation does not rely on a confinement with high- R mirrors, but rather on the possibility for the light to efficiently escape the slow-light region. The speed-bump can thus be seen as the photonic analogue of plasmonic nanofocusing devices, which provide strong field enhancements with slow plasmons in tiny air gaps formed at the mouth of almost touching metallic dimers [Fer10, Gra14].

Due to the unusual nature of the trapping mechanism, the question arises as to whether the DOS enhancement in speed bumps results from the excitation of an electromagnetic resonance. Often asymmetric lineshapes that are seemingly Lorentzian, such as those in Fig. 1-4, are not due to a single resonance but to an interference between two modes with very similar energies [Lov13], see the striking example of Fig. 3 in [Sau13]. To clarify the origin of the asymmetric lineshapes, we compute the resonance modes supported by the speed bump designed for a target group index of 100 in the spectral range of interest, around the band edge frequency $\omega_0 = 2.043 \cdot 10^{15} \text{ s}^{-1}$. We find a single resonance mode with a complex eigenfrequency $\omega = \omega_0(0.999 - 0.001i)$ corresponding to a quality factor of $Q = 500$. Figure 1-5a shows the distribution of the y -component of the magnetic field of the resonance mode. The mode volume, normalized with the method in [Bai13], is $V = 0.092 + i0.039 \mu\text{m}^3$.

The real part of V , ≈ 0.1 wavelength cube, directly quantifies the normalized LDOS enhancement (the Purcell factor P) at resonance $\omega = \omega_0$, and the

imaginary part accounts for the asymmetry of the spectral lineshape

$$\text{response, } P(\omega) = \frac{3}{4\pi} \left(\frac{\lambda_0}{n}\right)^3 \text{Re}\left(\frac{Q}{V}\right) \frac{\omega_0^2}{\omega^2} \frac{\omega_0^2}{\omega_0^2 + 4Q^2(\omega - \omega_0)^2} \left[1 + 2Q \frac{\omega - \omega_0}{\omega_0} \frac{\text{Re}(V)}{\text{Im}(V)}\right] \text{ [Sau13].}$$

Figure 1-5b shows the normalized LDOS seen by an x -polarized emitting dipole placed in the center of the speed bump. The single-mode model prediction computed with the analytical expression for $P(\omega)$ and shown with the red-dashed curve faithfully agrees with fully-vectorial Green-tensor calculations (black-solid curve), evidencing that the speed-bump physics is governed by a single electromagnetic resonance.

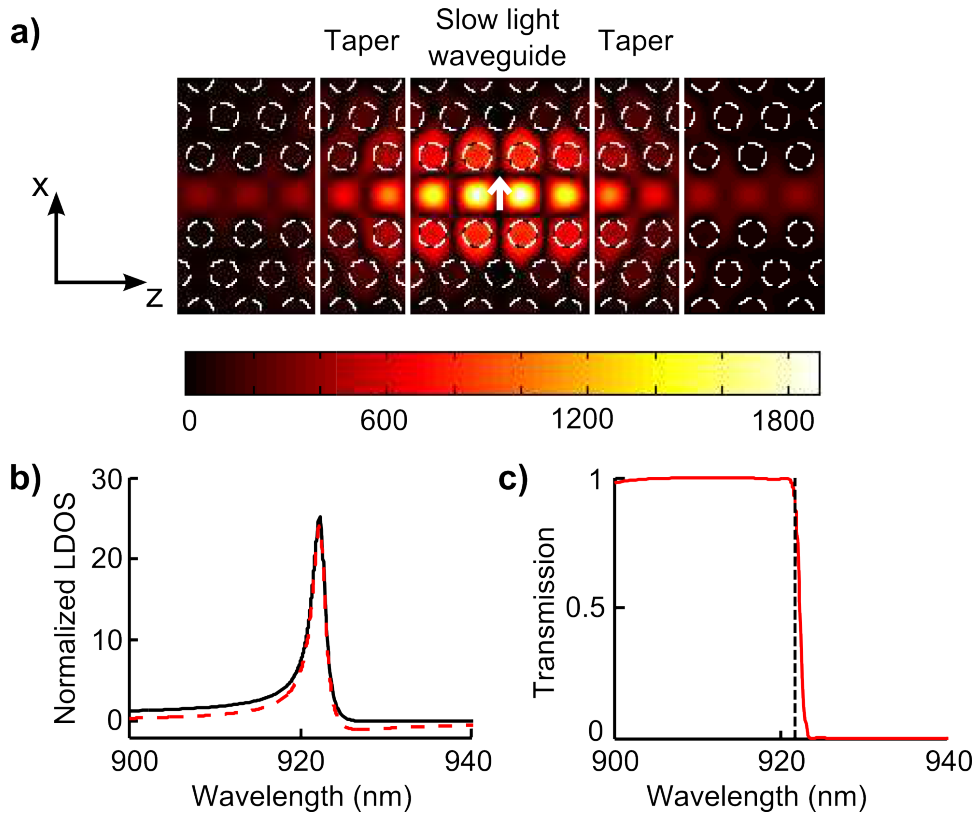


Figure 1-5. Optical properties of the speed bump resonance mode. **a)** $|H_y|$ for the resonance mode of a 4-period long speed bump. **b)** Normalized LDOS seen by the x -polarized electric dipole source placed in the center of the speed bump, see **a)**. The black and dashed-red curves are respectively obtained with fully-vectorial Green-tensor calculations [Fag16] and with the single-mode expansion formula. **c)** Step-like transmission (red curve) under illumination by the guided Bloch mode of the fast-W1 waveguide. The black dashed line represents the band edge of the slow-W1 mode. All the results in **(a)-(c)** are obtained for a speed bump with a taper optimized for $n_g = 100$.

Comparatively, classical defect-modes PhC microcavities have much smaller $\text{Im}(V)$'s, and also more symmetric lineshape. Large values of $\text{Im}(V)$ are encountered with plasmonic nanoantennas [Sau13], for which the asymmetry of the DOS on the red and blue sides of the resonance is due to the metal dispersion. For speed bumps, the asymmetry is not due to material dispersion, but to the highly dispersive nature of the slow-W1 Bloch mode at the band edge.

The value of $\text{Im}(V)$ is not the sole difference between the speed bumps and the classical defect-modes PhC microcavities. PhC microcavities have energies in the photonic gap of the mirrors, whereas speed bumps have energies at the band edge frequency. Also, the responses of PhC microcavities strongly depend on the defect length, while the length of the slow-light region of speed bumps is only of minor importance. No precise phase accumulation and matching are required with speed bumps. Another striking difference with classical PhC microcavities is shown in Fig. 1-5c. Unlike PhC microcavities that present an Airy-type symmetric Fabry-Perot transmission, the speed-bump transmission exhibits an unusual step-like shape, varying from 1 to 0 at the band edge of the slow-W1 waveguide with a steepness that slightly depends on the length of the slow-light region and the target group index used to design the tapers.

1.6 Conclusion

We have added a new family of resonators to the long list of photonic microcavities. The photonic speed bumps are composed of a short slow-light section with a few identical unit cells that are impedance-matched with the outside space by short tapers. The latter give the impression to the slow wave that the short slow light section is much more extended and thus artificially enhance the DOS. The nature of speed-bump resonances is markedly different from that of the resonances of classical defect-mode PhC microcavities. Speed-bump resonances more resemble those found in

plasmonic nanofocusing devices. Energy is not accumulated by confining light between two mirrors, but rather by implementing a sudden reduction of the light speed, followed by a reciprocal acceleration to go back to the initial speed.

Using the mature photonic-crystal-waveguide platform, we have designed realistic speed-bumps that can be easily fabricated with present technologies. 3D simulations confirm the possibility of mimicking infinite periodic waveguides with compact devices that are only 10-period long and achieving large DOS enhancements corresponding to slowdown factors of 1000. Just as for PhC microcavities, we have shown that the LDOS enhancement of speed bumps is due to a single electromagnetic resonance, but striking differences have also been observed between the two resonators. For instance, the resonance frequencies of speed bumps are no longer set by a Fabry-Perot-like phase-matching condition and are actually independent of the length of the slow-light periodic section. Also the transmission presents a highly unusual step-like character not encountered in PhC microcavities.

Photonic-crystal speed bumps may find applications for engineering photon emission and scattering. Owing to their capability to suddenly vary the light speed, these microscale dielectric devices are ideal candidates to implement 1D photon/emitter interfaces [Sol15, Haa15] capable of mediating long-range interactions between quantum emitters using photons propagating in fast guided modes and achieving nearly-perfect couplings between the emitters and the waveguide in slow light sections. In addition, the possibility of mimicking infinite periodic waveguides with compact devices may allow fundamental studies on structural slow light at ultra-low speeds, whose observation is usually hampered by localization effects due to inevitable fabrication errors [Moo08, Xue16]. In this regard, it would be interesting to study the properties of speed bumps for slowness such that the localization length is longer or comparable to the slow-light section length.

Chapter 2 - LOWER BOUND FOR THE SPATIAL EXTENT OF LOCALIZED MODES IN PHOTONIC-CRYSTAL WAVEGUIDES WITH SMALL RANDOM IMPERFECTIONS

2.1 Introduction

Random imperfections, even very small ones, can have a profound impact on light propagation in periodic photonic structures, the most striking phenomenon being undoubtedly the formation of small localized modes in the vicinity of photonic band edges. The interplay between long-range order and perturbative disorder, originally proposed as a way to enable strong light localization in three-dimensional media [Jon87, Con08], was largely investigated in one-dimensional (1D) layered structures (i.e., Bragg stacks), which can be modelled with greater ease [Mcg93, Bul98, Dey98, Vin04, Kal06, Izr09, Pod12]. Besides these works, the research topic arose considerable interest in the photonic-crystal community, when it was realized that the operation of slow-light devices based on photonic-crystal waveguides (PhCWs) was unavoidably limited by small residual fabrication imperfections [Not01, Moo08, Maz10, Mel14]. The possibility to observe individual localized modes formed by disorder in these structures and exploit them as "optical cavities" for, e.g., quantum information processing [Sap10, Thy12, Gao13, Min13] or random lasing [Yan11, Liu14] prompted numerous studies on their confinement properties [Top07, Smo11, Spa12, Hui12]. Quite remarkably, near-field measurements on PhCWs fabricated with state-of-the-art nanotechnologies [Spa12, Hui12] suggest that *wavelength-scale* localized modes, comparable in size to engineered heterostructure nanocavity modes in PhCWs [Son05, Kur06], could naturally be formed in spite of the very low perturbation level.

It is widely accepted that the typical spatial extent of localized modes in the band decreases when approaching the edge. This trend is generally understood by drawing a parallel between the mode spatial extent and the "Anderson" localization length, which describes the exponential attenuation of the ensemble-averaged intensity with the system size. The localization length is known to scale as the square of the group velocity v_g for small disorder levels [Hug05a, Maz09, Gar10], thereby indicating that light confinement should be extremely strong at the band edge, where v_g vanishes (in perfectly periodic media). The formation of small localized modes in close vicinity to the band edge, however, deserves special attention, as it relies not only on the interference between multiply-scattered propagating waves, leading to Anderson localization [Lag09, Seg13], but also on the attenuation provided by the photonic band gap. Imperfections, even vanishingly small ones, can indeed easily create gap (defect) modes, similar in nature to photonic-crystal nanocavities [Lal08, Bli08, Not10], which participate in the broadening of the band edge [Sav11, Hui12, Man12] and in the formation of the so-called Lifshitz tail in the band gap [Lif64, Hui12]. In this narrow spectral range around the band edge, propagating and evanescent waves mix up and the group velocity evidently loses physical significance, thereby requiring the basic parallel between mode spatial extent and localization length to be revisited.

In this chapter, we theoretically, numerically and experimentally investigate the confinement properties of localized modes in close vicinity to the band edge of 1D periodic photonic structures at small disorder levels. We demonstrate in particular that the size of the smallest localized mode that may be found in a given photonic structure is driven by the *effective photon mass*, i.e. the flatness of the dispersion curve, rather than the group index. This, in turn, suggests that an engineering of photonic bands in PhCWs may allow us either to lower the impact of residual imperfections on the performance of slow-light photonic devices or to reinforce the light confinement for strong light-matter interaction purposes.

The fact that the sensitivity of wave transport to random perturbations is increased with the flatness of the dispersion relation is well known in condensed matter physics [Cha10, Bab16], but the possibility to control the spatial extent of the smaller localized modes via the effective mass has not been suggested in earlier works on light localization in photonic structures [Joh87, Not01, Hug05a, Top07, Moo08, Maz09, Sap10, Maz10, Gar10, Smo11, Yan11, Sav11, Thy12, Spa12, Hui12, Gao13, Min13, Mel14, Liu14, Man15]. We believe that the conceptual understanding gained from our study could help the design of PhCWs and cavities with potential outcomes in photonic technologies.

In the remainder of this chapter, we first present a phenomenological model for light propagation near the band edge of 1D periodic media with small random perturbations. We predict that a minimum number of periods is necessary to form a localized mode at a given disorder level and derive a closed-form expression relating this lower bound to the disorder level and the effective photon mass. Then, we test and validate our predictions by a series of numerical simulations on randomly-perturbed Bragg stacks and PhCWs. At tiny disorder levels, PhCWs are found to support surprisingly small localized modes, much smaller than those observed in Bragg stacks thanks to their larger effective photon mass. Finally, in collaboration with Thomas Krauss's group in York University for the fabrication and Frédérique de Fornel's group in Burgundy University for the near-field experiments, we verify this possibility by performing near-field measurements on a photonic-crystal waveguide fabricated without any intentional disorder and observe very distinctly a localized mode with a spatial extent of only $6 \mu\text{m}$, in agreement with our numerical simulations.

2.2 Formation of localized modes at band edges

We start by considering an arbitrary one-dimensional periodic photonic structure and aim at establishing an explicit relation between the dispersion

relation of the unperturbed medium, the level of geometric variation, and the spatial extent of the resulting localized modes at the band edge. A typical dispersion curve $\omega(k)$ near a band edge is sketched in Fig. 2-1a. While it is common practice in the literature to plot band structures for purely real wavevectors only, one should be aware that the wavevector is in general a complex quantity, $\kappa = k + i\alpha$. Dispersion relations are analytic and continuous at band edges [Koh59] and can be approximated by a quadratic expression

$$\omega - \omega_0 = \frac{(\kappa - \pi/a)^2}{2m}, \quad (2-1)$$

where $m = (\delta^2\omega/\delta^2\kappa)^{-1}$ is the effective photon mass, which describes the flatness of the dispersion curve. The complex wavevector equals $\kappa = k$ in the band, corresponding to propagating waves, and $\kappa = k + i\alpha$ in the gap, leading to an exponentially-damped evanescent wave. Note that Eq. 2-1, which comes from a Taylor expansion of the dispersion relation at the band edge, remains valid for complex periodic waveguides provided that the mode dispersion remains below the light line of the cladding. It is hence often used in photonics to describe band-edge phenomena [Son05, Pov05, Xue16] (albeit for real wavevectors only in most cases).

As sketched in Fig. 2-1a, small geometrical variations result in energy shifts $\pm\Delta\omega$ of the dispersion curve with negligible deformation [Sol04]. In the perturbative regime, the relative frequency shift $\Delta\omega/\omega$ is directly proportional to the variation of the waveguide effective refractive index $\Delta n_{eff}/n_{eff}$, which itself scales linearly with the disorder level σ . These energy shifts define three frequency regions, where different behaviors are expected. At frequencies $\omega < \omega_0 - \Delta\omega$, Bloch waves are essentially evanescent (bottom panel in Fig. 2-1b). In this regime, light is expected to be strongly damped via the band gap attenuation and few gap modes may be found. By contrast, at frequencies $\omega > \omega_0 - \Delta\omega$, Bloch waves are essentially propagating (top panel in Fig. 2-1b). This is typically the regime where

Anderson-localized modes are found and the localization length should scale as $\xi \sim 1/n_g^2$. To understand the limited range of validity of this regime, one should know that this scaling behavior comes from a double limit in the group velocity $v_g = c/n_g$ and the disorder level $\sigma \propto \Delta\omega$ both tending towards zero. It is valid only when σ tends towards zero at a fast enough rate compared to v_g . This requirement guarantees that the impact of random imperfections on transport remains perturbative [Wan08]. Due to the nonvanishing disorder level in real nanostructures, this condition necessarily fails in the close vicinity of the band edge and the $1/n_g^2$ scaling behavior unavoidably breaks down. This peculiar regime that surrounds the band edge, $\omega_0 - \Delta\omega \leq \omega \leq \omega_0 + \Delta\omega$, is the one of interest in this chapter. Here, light propagating in the randomly-perturbed periodic medium will experience alternatively and randomly either phase-shifts Δk (in $\text{Re}(\kappa)$) or exponential attenuations α (in $\text{Im}(\kappa)$). The formation of localized modes should therefore rely on an interplay between propagating and evanescent waves (middle panel in Fig. 2-1b).

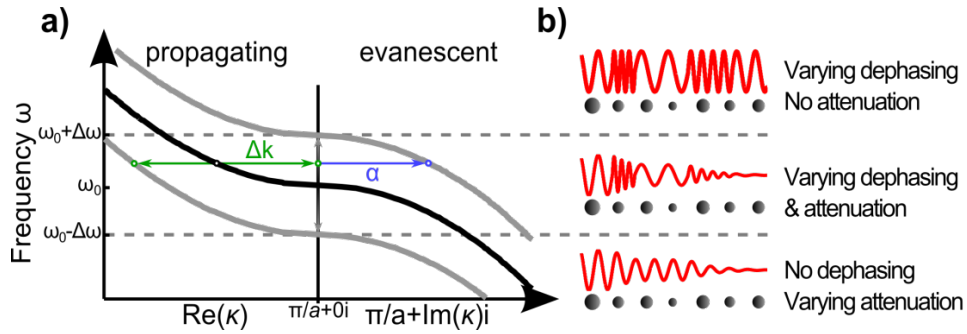


Figure 2-1. Effect of random imperfections on light propagation in one-dimensional periodic media. **a)** Sketch of the dispersion curve of a one-dimensional periodic medium near a band edge at $\omega = \omega_0$ (black curve). Note that the left and right parts of the plot correspond to the real and imaginary parts of the wavevector κ . Perturbations result in positive or negative energy shifts $\pm\Delta\omega$ of the dispersion curve (gray curves), where $\Delta\omega \ll \omega_0$, resulting in a phase-shift Δk (green arrows) and/or a damping at rate α (blue arrow) for a guided wave at $\omega = \omega_0 + \delta\omega$. **b)** Sketches of wave propagation in randomly-perturbed periodic media. In the vicinity of the band edge, $\omega_0 - \Delta\omega \leq \omega \leq \omega_0 + \Delta\omega$, light successively and randomly experiences either phase-shifting or damping unit cells (middle), contrary to higher and lower frequencies, for which only phase-shifts or tunnelling damping are experienced (top and bottom, respectively).

We adopt a Fabry-Perot picture to model the formation of a localized mode in this regime. By analogy with standard optical cavities, for a localized mode to appear at a frequency ω (it is convenient to situate the frequency in relation to the band edge, $\omega = \omega_0 + \delta\omega$), it is required that, during its transport, light both accumulates a phase-shift that satisfies a phase-matching condition (typically, 2π on a round trip) and experiences a strong damping (typically, $1/e^2$ for the intensity). This simple reasoning first indicates that *a minimum number of periods N_{min} is necessary to form a localized mode in a perturbed medium.*

Evidently, smaller localized modes are formed for imperfections that produce larger momentum variations and damping rates. Depending on the perturbation and the frequency, the momentum variations (with respect to the unperturbed mode) can be either positive or negative, and the damping rate can be zero or take large values. To account for these statistical variations, we calculate the average momentum variation $\langle \Delta k \rangle$ and the average damping rate $\langle \alpha \rangle$ using Eq. 2-1 and, keeping only the lowest order in $\Delta\omega/\omega$, find that

$$\langle \Delta k \rangle \approx \begin{cases} \frac{1}{2} \sqrt{2m\Delta\omega} \left(1 + \frac{\delta\omega}{2\Delta\omega} \right) & \text{for } \delta\omega \leq 0 \\ \frac{1}{2} \sqrt{2m\Delta\omega} \left(1 - \sqrt{\frac{\delta\omega}{2\Delta\omega}} \right) & \text{for } \delta\omega \geq 0 \end{cases} \quad (2-2)$$

and

$$\langle \alpha \rangle \approx \frac{1}{2} \sqrt{2m\Delta\omega} \left(1 - \frac{\delta\omega}{2\Delta\omega} \right), \quad (2-3)$$

Hence, $\langle \Delta k \rangle$ is the largest at the band edge ($\omega = \omega_0$) and decays more slowly in the gap than in the band ($\delta\omega/2\Delta\omega$ compared to $2\sqrt{\delta\omega/2\Delta\omega}$), while $\langle \alpha \rangle$ continuously increases when entering deeper into the gap. This indicates, on the one hand, that *the smallest localized modes should be found at the band edge ($\omega = \omega_0$)*, and on the other hand, that the localized modes formed in the gap

should be smaller and more numerous than in the band. To obtain the lower bound value for the mode spatial extent, it is thus sufficient to consider the momentum variation and damping rate at the band edge, $\langle \Delta k \rangle = \frac{1}{2} \sqrt{2m\Delta\omega}$ and $\langle \alpha \rangle = \frac{1}{2} \sqrt{2m\Delta\omega}$, which evidently become more important as the dispersion curve flattens, i.e. for larger effective photon masses. This leads us to predict that the lower bound on the spatial extent of localized modes in perturbed periodic media scales as

$$N_{min} \propto (a^2 m \Delta\omega)^{-1/2}, \quad (2-4)$$

Equation 2-4 is obtained by neglecting intricate multiple-scattering processes in transport, such as variations of the reflection and transmission coefficients at the perturbed lattice sites [Bar11], yet it is highly robust and accurate. As will be seen with numerical and experimental results, fine effects related to the actual geometry, especially the scattering coefficients at every lattice sites, impact the proportionality factor but not the scaling with m and $\Delta\omega$.

2.3 Computational method

To test our prediction on the existence of a minimum number of periods necessary to form a localized mode near a photonic band edge, we resort to numerical simulations. The computational results are obtained with an in-house fully-vectorial frequency-domain Fourier-Bloch-mode method presented in the previous chapter [Sil01, Lec07a] and described in Appendix 1. In the present context, a systematic exploration of real PhCWs with long-scale propagation lengths and nanometer-scale perturbations would require unreasonably long computation times with 3D fully-vectorial approaches, considering as well the large number of simulated structures to reach good statistical accuracy.

For this reason, we resort to a 2D fully-vectorial analysis and use an effective index for the dielectric material to model the transverse confinement of the

main TE-mode in the membrane [Hug07]. The effective index value is chosen so that the cutoff frequency of the W1 waveguide matches that of the 3D structure. Out-of-plane scattering into the air cladding is therefore omitted in the computation. Fortunately, in close vicinity of the band edge, that is the region of interest here, out-of-plane scattering into the air cladding is much weaker than backscattering (scaling as n_g and n_g^2 , respectively) [Hug05a, Ofa10]. Since the out-of-plane channel is much weaker than the backscattering channel near the band edge, we expect inaccuracies on the quality factor of the resonances but we believe that the approximation is likely to impact only weakly our predictions on the spatial extent of the cavity modes.

The same method is implemented later on for the calculations of localized modes in Bragg stacks. In this case, 1D calculations are sufficient to describe the system.

2.4 Threshold in the size distribution of localized modes

We perform 2D fully-vectorial calculations on a single-row-missing (W1) PhCW with an hexagonal lattice constant $a = 420 \text{ nm}$, a hole radius $0.3a$ and an effective index of 2.83 to model the transverse confinement in a silicon membrane of thickness 240 nm suspended in air [Hug07]. We implement disorder by varying the hole radii in the first rows of the W1 waveguide according to a normal distribution with standard deviation σ . The computational layout is shown in Fig. 2-2a. In brief, we calculate the local density of states (LDOS) spectrum in the center of a $100a$ -long perturbed medium and spectrally locate the resonant modes of the system from the observed Lorentzian peaks, see Fig. 2-2b for an example. The LDOS spectrum is calculated on a narrow frequency window close to the band-edge wavelength $\lambda_0 = 2\pi c/\omega_0$ ($\lambda_0 - 0.5 \text{ nm} < \lambda < \lambda_0 + 1.5 \text{ nm}$), in which,

according to our analysis above, the smallest possible localized modes should be observed. We apply a strict protocol, described in the Appendix 3, to ensure that the peaks correspond to individual localized modes, i.e. they are not affected by the finite length of the computational window. Repeating the calculation for 900 independent disorder realizations, we estimate the distribution function $P_\sigma(L_0)$, which represents the likelihood of observing a localized mode near the band edge frequency with a spatial extent L smaller than L_0 at any position along an infinitely-long W1 waveguide perturbed by a disorder level σ .

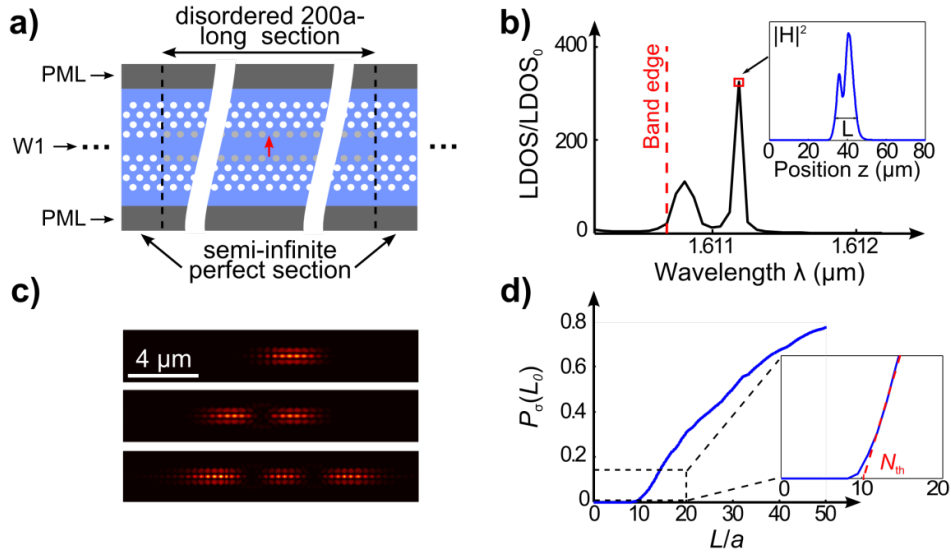


Figure 2-2. Numerical study of small localized modes formed in W1 waveguides. **a)** Computational layout used to estimate $P_\sigma(L_0)$. The red arrow represents a dipole source placed in the center of a $100a$ -long section of the PhCW. The grey holes of the two inner rows represent the perturbed holes. Two semi-infinite unperturbed PhCWs surround the perturbed section. **b)** Spectral dependence of the LDOS normalized to that in free space, LDOS_0 , in a specific configuration. The vertical red dashed line indicates the band edge wavelength. The envelop of the magnetic-field-intensity profile $|H|^2$ of the resonant mode marked by a red square is shown in the inset. Its spatial extent is $L = 12.4 \mu\text{m}$. **c)** Examples of the intensity distribution $|E|^2$ of small localized modes obtained by numerical calculations with $\sigma = 1.5 \text{ nm}$. The localized modes may be composed of several sub-spots. **d)** Numerical prediction of $P_\sigma(L_0)$ for a W1 waveguide with $\sigma = 1.5 \text{ nm}$. The distribution exhibits a clear threshold N_{th} , obtained from a linear fit (red dashed line).

$P_\sigma(L_0)$ is shown in Fig. 2-2d for a disorder level $\sigma = 1.5 \text{ nm}$, which is comparable to the residual disorder amplitude left by state-of-the-art nanofabrication technologies. The curve clearly exhibits a threshold-like behavior and evidences that localized modes are formed essentially above a certain threshold length $N_{th}a$, where N_{th} is the number of lattice periods. The threshold is straightforwardly estimated by a linear fit of $P_\sigma(L_0)$ for $0.03 < P_\sigma < 0.15$. The intensity maps $|E|^2$ of three localized modes are shown in Fig. 2-2c, the first one corresponding to the smallest mode ($L = 3.85 \mu\text{m}$) we obtained among the 900 realizations, the others showing that localized modes may be composed of several sub-spots. Quite remarkably, our numerical simulations unambiguously show that wavelength-scale localized modes may be observed in PhCWs at disorder levels of the order of $\lambda/1000$. This point will be further discussed below. It is also interesting to remark that most of the smaller localized modes were formed in the gap region, as expected from the perturbative analysis in the previous section.

We proceed to the numerical verification of the scaling law in Eq. 2-4. For a careful testing, we consider two different geometries, the W1 waveguide investigated above and a 1D quarter-wave Bragg stack, which have substantially different localization properties. Figure 2-3a shows the dispersion curves of the unperturbed photonic structures, where the Bragg stack is composed of alternating dielectric layers with lattice constant $a = 453 \text{ nm}$ and refractive indices $n_1 = 1.5$ and $n_2 = 3.5$. The band edges of the two photonic structures appear at nearby frequencies, yet the PhCW exhibits an effective photon mass about 10 times larger than the Bragg stack.

The scaling law in Eq. 2-4 is tested, on the one hand, by varying the disorder level σ imposed on the PhCW without changing its structure -- $\Delta\omega$ is therefore varied while m and λ_0 remain constant -- and, on the other hand, by varying the refractive index n_2 of the Bragg stack up to large (unrelativistic for optical waves) values while precisely monitoring the disorder level and

the period to respectively maintain $\Delta\omega/c = 0.01 \mu\text{m}^{-1}$ and $\lambda_0 = 1.51 \mu\text{m}$ constant. In the latter case, the sole physical quantity that is expected to vary is therefore the effective photon mass, from $mc \approx 4$ to $40 \mu\text{m}^{-1}$. Furthermore, the same protocol is applied and an average over 10000 independent disorder realizations, obtained by randomly varying the layer thicknesses, is performed (computations rely on simple 2×2 matrix products). The resulting threshold lengths N_{th} are shown in Fig. 2-3b as a function of $(a^2 m \Delta\omega)^{-1/2}$. A clear linear dependence is obtained in both cases, thereby constituting a firm validation of the scaling law proposed in Eq. 2-4.

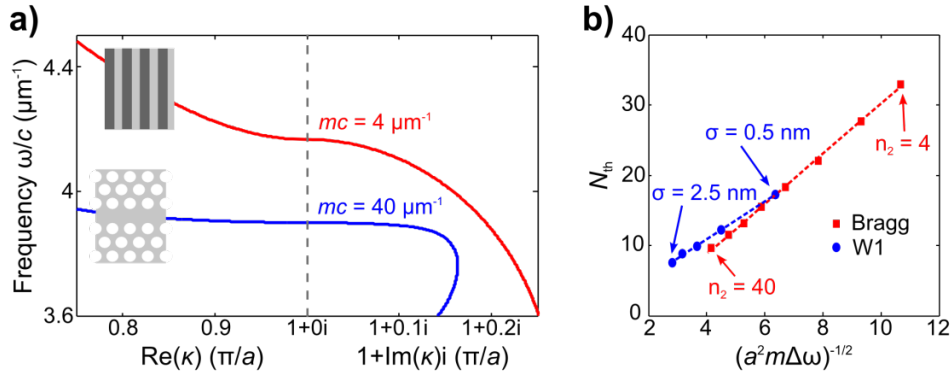


Figure 2-3. Scaling of the size of smallest localized modes: verification of Eq. 2-4. **a)** Dispersion curves $\omega(\kappa)$ of a W1 waveguide and of a quarter-wave Bragg stack with $n_1 = 1.5$ and $n_2 = 3.5$. The former has an effective photon mass that is about 10 times larger than that of the latter. **b)** Size threshold N_{th} for the two photonic structures with varying $\Delta\omega$ (while keeping m constant for the PhCW) or varying m (while keeping $\Delta\omega$ constant for the Bragg stack). The linearity of the curves validates Eq. 2-4. The difference in the slopes is likely to be due to the different scattering coefficients at every perturbed interface [Bar11]. Furthermore, W1 waveguides exhibit wavelength-scale localized modes, much smaller than those possibly obtained in Bragg stacks, even at tiny disorder levels.

As already noted above, our numerical simulations indicate that wavelength-scale localized modes may be observed in W1 waveguides even at tiny disorder levels. Figure 2-3b shows that such small localized modes *cannot* be observed in classical Bragg stacks (except if one considers unrealistically large values for the index contrast). It is the large effective photon mass provided by W1 waveguides that makes the difference.

The formation of localized modes near the photonic band edge is completely expected, but the fact that structural imperfections as small as $\lambda/1000$ may lead to the formation of modes with spatial extents of only a few wavelengths comes as a surprise. In engineered nanocavities, for instance, the lattice structural modifications employed to create wavelength-scale gap modes are usually larger than $\lambda/1000$, typically consisting in removing, shifting or resizing a few holes [Son05, Lal08, Not10]. In addition, they are spatially correlated and precisely controlled to collectively contribute to the mode formation. Thus, one would expect rather large volumes for modes created by perturbations that are much weaker and random.

2.5 Near-field observation of a wavelength-scale localized mode

Our numerical results encouraged us to explore the possibility of observing wavelength-scale localized modes at tiny disorder levels. The experimental part has been realized by Thomas Krauss's group in York University for the fabrication and Frédérique de Fornel's group in Burgundy University for the near-field experiments. We fabricated a W1 waveguide without adding any intentional disorder during the writing process, so that the sole perturbation that remained was the inevitable residual disorder caused by our state-of-the-art fabrication technology. The typical disorder level of the fabrication facility has been characterized by thorough statistical analysis in prior studies and was found to be $\sigma \sim 1\text{-}2\text{ nm}$ [Por11]. Though our procedure lacks control compared to previous studies on localization that introduce intentional random perturbations [Top07, Sap10, Gao13, Thy12], we are able to reach a minute and unprecedented level of perturbation that has never been probed up to now near photonic band edges.

At vanishingly small group velocities, it is well known that the optical mean free-path is very short and coupling light into localized modes cannot be achieved by end-fire injection through cleaved facets [Not10]. For this reason,

a layout consisting of a pair of collinear waveguides was designed: a W1 waveguide operating in the slow-light regime near the band cutoff-wavelength $\lambda_0 \sim 1490 \text{ nm}$, and a W1.1 (10% larger defect-width) waveguide operating in the fast-light regime, and therefore much less sensitive to residual imperfections. An SEM micrograph of a typical set of waveguides fabricated into a 220-nm thick free-standing silicon membrane is shown in Fig. 2-4a. The fast (W1.1) waveguide is used as an independent channel for delivering light into the localized modes supported by the slow (W1) waveguide via evanescent coupling, see the inset of Fig. 2-4a. This coupling is extremely weak due to the very low disorder level and is therefore expected not to affect the localization properties of interest here. Furthermore, compared to a previous approach where TE-like localized modes were excited via a weak coupling with TM-like ballistic modes in a single PhCW, thereby resulting in near-field images containing both localized and extended modes [Hui12], their configuration allows us to form clear near-field maps of individual localized modes and thus, estimate their spatial extent with greater accuracy.

Nevertheless, because of their small spatial extents and spectral bandwidths as well as their unknown spatial and spectral positions, wavelength-scale localized modes remain challenging to observe. Hence, they first realize multispectral near-field scanning-optical microscopy (SNOM) with low-spectral (200 pm) and low-spatial resolution (100 nm) [De12] followed by a high spectral-resolution (1 pm) and high-spatial-resolution ($\sim 62 \text{ nm}$) measurements at spatial locations found with low resolution. This allows us to detect modes with larger Q 's, but in return, finding a resonance becomes very time-consuming. Figure 2-4b shows a state formed by a chain of spots with varying brightness, which collectively resonate at the same wavelength, ergo all spots including the less intense spots belong to the same coherent state that covers the entire scan interval. The "stadium-shaped" patterns are due to the cavity tip interaction [Muj07]. Figure 2-4c shows a different mode composed of three dominant main spots that are grouped together and show

up over a dark background. It is the smallest mode that we have observed. Its total spatial extent L is smaller than $6 \mu\text{m}$. For comparison, the numerical data reported in Fig. 2-2d predict that $P_{1.5}(L_0)$ is equal to 0.14 for $L_0 = 6 \mu\text{m}$. This implies that, on average along the W1 waveguide, localized modes with spatial extents $L \leq 6 \mu\text{m}$ are expected every $L_0/P_{1.5}(L_0) = 43 \mu\text{m}$. This is consistent with our observation of a single localized mode obtained by scanning a $25\text{-}\mu\text{m}$ -long section of the W1 waveguide. Interestingly also, we note that the predicted and measured lower bound in mode spatial extent matches well with the cavity length above which the operation of photonic-crystal cavity lasers becomes significantly impacted by residual fabrication imperfections [Xue13]. The occurrence of disorder-induced localization in engineered cavities is an aspect that deserves more attention.

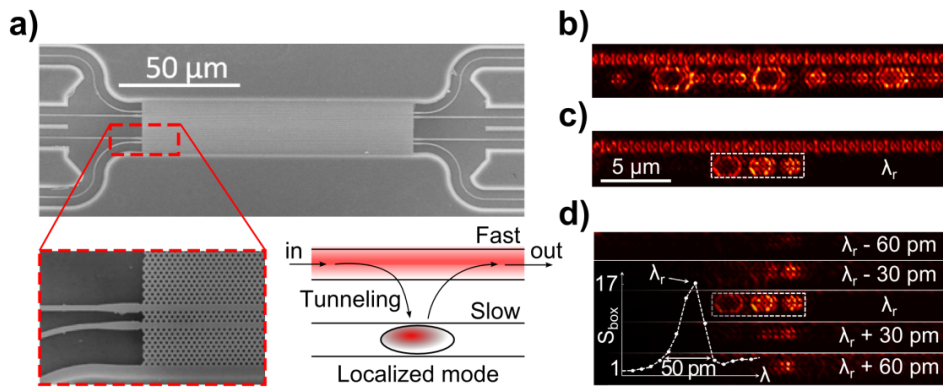


Figure 2-4. Near-field experiment. **a)** Scanning electron microscope images of the sample. The inset on the bottom left provides a close-up of the two side-coupled $84 \mu\text{m}$ -long PhCWs and of the access ridge waveguides used to inject light. The inset on the bottom right shows a sketch of the layout designed to obtain clear near-field images of the localized modes. Light is injected in the W1.1 waveguide, which operates in the fast-light regime, and couples evanescently to localized modes in the W1 waveguide, operating in the slow-light regime. **b)-c)** High-resolution (10 pm) near-field images of the PhCW pair recorded over an area covering the first $25 \mu\text{m}$ of the sample. The panel in **b)** shows an extended state ($\lambda = 1489.61 \text{ nm}$) composed of a series of coupled localized modes. The panel in **c)** shows a wavelength-scale localized mode ($\lambda = 1488.38 \text{ nm}$) composed of three sub-spots and of spatial extent about $6 \mu\text{m}$. It is the smallest localized mode detected experimentally. **d)** Spectral evolution of the wavelength-scale mode near the resonance wavelength λ_r . The inset shows the intensity $S_{\text{box}}(\lambda)$ integrated over the rectangular dashed-linebox and normalized to the averaged intensity in the W1.1 waveguide.

Figure 2-4d finally shows the spectral evolution of the localized mode, calculated by integrating the measured intensity over a fixed rectangular area comprising the mode and normalizing it to the averaged intensity in the W1.1 waveguide for several wavelengths. The result confirms the existence of a high confinement level both in the spatial and spectral domains. As the wavelength is tuned away from resonance at $\lambda = 1488.38 \text{ nm}$, we observe that the spatial and spectral variations of the spot intensities exhibit an intricate behavior, suggesting a beating between several modes (although non-uniform coupling with the tip cannot be excluded). The inset shows the spectral evolution of the normalized intensity of the localized state and evidences a resonance with a $Q \sim 5 \cdot 10^4$. Since the localized mode is formed from tiny structural modifications, smaller than those typically employed for engineered cavities, mode-profile impedance mismatch [Lal08] is kept at a very low level, and leakage into the air cladding and into the W1.1 waveguide is expected to be as small as that encountered with side-coupled engineered cavities. Thus, we believe that the observed Q value is limited by the tip interaction, consistently with earlier works with silica tips and engineered cavities [Koe05].

2.6 Conclusion

In this chapter, we have investigated the physical mechanism underlying the formation of small localized modes at band edges of periodic media, demonstrating the existence of a minimal mode size and showing that this bound is predominantly driven by the effective photon mass. In particular, we have found that wavelength-scale localized modes naturally form up in PhCWs at state-of-the-art intrinsic disorder levels due to the flatness of the dispersion curve.

The localized modes have positions and frequencies that are not known in advance by design. As such, they are not easy to handle in applications that require extreme precisions, but their existence and the possibility to enhance

(statistically) their spatial confinement by using flatter dispersion curves is extremely relevant for quantum electrodynamics experiments [Sap10, Thy12, Gao13, Min13], random lasing [Yan11, Liu14], but also for sensing applications [Wan10, Scu13] and random photonics devices [Vyn12, Red13].

The existence of a lower bound for the volume of localized states in perturbed periodic media and the importance of the effective photon mass have not been pointed out in early works on optical localization in the slow-light regime. These first results, supported by a simple intuitive model, should encourage more in-depth theoretical investigations.

Similarly, the effective photon mass is rarely acknowledged in the literature on engineered nanocavities, such as the heterostructure family [Son05, Kur06], which are defect-modes that benefit from a slow-light effect close to the band edge [Lal08] and, as explained in this chapter, are in many respects similar to the present localized modes. We therefore expect that the conceptual understanding gained from this disorder-driven study will have repercussions on future photonic structure designs to push back the ultimate limit imposed by unavoidable disorder in slow-light photonic devices [Hug05a, Maz09, San12] as well as in engineered cavities [Tag11, Xue16].

Chapter 3 - HOLLOW-CORE PHOTONIC CRYSTAL WAVEGUIDE FOR REMOTE AND EFFICIENT COUPLINGS BETWEEN ATOMS AND WAVEGUIDES

3.1 Introduction

Strong atom-photon interaction, whereby a single photon can deterministically interact with a single atom, constitutes the basic building block of a number of quantum-processing, simulation, and sensing schemes. Enhancing the atom-photon interaction requires increasing the mode electric field at the position of the atom. This can be done by reducing the transverse size of the light mode, for instance, by guiding it in ultrathin unclad optical fibers [Kie04, Kie05, Vet10] or focusing it with high-numerical-aperture lenses [Het11, Tey08]. Further enhancement of the field amplitude can be achieved by reducing the mode longitudinal extent, either by manipulating the light dispersion to slow down the group velocity or, equivalently, by implementing a longitudinal resonator. Current implementations using both of these methods include quantum dots integrated into photonic-crystal-waveguide structures [Lun08] and atoms placed in high-finesse cavities [Dua04, Muc10, Rai01]. An emerging alternative is the interaction between ultracold atoms in vacuum and evanescent fields of slow guided modes supported by periodic photonic nanostructures [Gob14, Tho13]. These hybrid systems combine the subwavelength confinement and dispersion control of the nanostructures with the long coherence time of isolated single atoms, all on a flexible and scalable platform. In current approaches [Dou15, Gob14, Yu14], the atoms are placed inside tiny 250-nm-wide slots etched into corrugated bridge waveguides. Due to the narrowness of the slit, hybrid trapping mechanisms involving Casimir-Polder forces and repulsive

frequencies-detuned dipole-force have been investigated [Vet10]. Although such a hybrid approach has great potential, it is not without significant technical challenges and the precise control of the interaction, implemented in corrugated-slot (or “alligator”) waveguide [Gob14], had proved difficult. Indeed constraints would be largely relaxed if the atoms could be trapped far away from any interfaces, while maintaining a strong atom-waveguide interaction. That, of course, begs the question of slow-light hollow-core waveguides. Indeed structural slow light offering a large fraction of its field in air at significant distance from any interface has a huge potential in many areas of science and technology, from cold atom engineering to sensing [Lai11, Scu13].

Slow light in air proceeds from two conflicting perspectives. One expects that the slow Bloch mode well extends into the vacuum cladding, implying that it weakly interacts with the periodic modulation. Conversely, a strong interaction between the Bloch mode and the periodic modulation is needed, keeping away from any weak-permittivity-modulation regime for which the slow-light spectral bandwidth is very weak [Zan16]. To realize this, one may consider a nanowire waveguide operating close to the cut-off frequency, with a mode profile that expels away in the air clad and with an effective index $n_{eff} \approx 1$. By periodically patterning the wire with an air-hole array for instance, light can be slowed down. However, due to the weak confinement, only a small fraction of the field interacts with the holes. The effective index modulation $\Delta n = n_{eff} - 1$ becomes small, thus reducing the effective photon mass $m = \left(\frac{\partial^2 \omega}{\partial^2 k}\right)^{-1}$, i.e. the flatness of the mode dispersion curve at small group velocities which acquaints us with the slow-light spectral bandwidth ($m \propto \Delta n$ [Yeh88]).

To mitigate the mass reduction, it is convenient to consider a photonic crystal (PhC) guidance mechanism with strong phase dispersion, rather than a guidance by total-internal reflection [Zan16]. The degree of freedom added by the dispersive PhC-reflection-phase can be exploited to flatten the mode

dispersion curve, as evidenced in [Zan16] where is reported an original PhC-waveguide structure that offers an empty half space to load the atoms and a $\times 60$ fold mass enhancement compared to the alligator structure for a comparable confinement level ($n_{eff} = 1.15$).

In this work, we explore ultimate regimes of slow hollow-core waveguides with effective mode indices that approaches 1, and obtain large coupling efficiencies in vacuum at large distances ($\lambda/3$) away from any material interface. After highlighting the limitations of simple index-guided periodic nanowire waveguides, we propose an original PhC waveguide that uses two different periodicities to implement a strong light-atom interaction in a wide vacuum slot. Finally, after comparing relevant figures of merit of the present waveguide with known geometries, we will study the atom-waveguide coupling and demonstrate coupling coefficient larger than 95% for 1.12 μm -large slot.

3.2 Wide-slot photonic crystal waveguide design

The first slow-light geometry that comes to mind to implement efficient atom-photon couplings at large distance in vacuum claddings is the periodic nanowire (Fig. 3-1b). One may tune the wire size to implement a mode with a dispersion curve, shown with the solid-green line in Fig. 3-1b, which lies just below the light line. Since the normalized propagation constant $k_{//}/k_0 = n_{eff}$ is close to 1, the mode profile slowly decays in the vacuum cladding, and the atom-waveguide coupling is relatively large. Even larger couplings are achieved by reducing the group velocity of the guided mode by implementing a periodic refractive index modulation. The latter folds the photonic band of the mode into the first Brillouin zone and opens a gap at a frequency close to the light line of the cladding, as shown with the solid-blue line in Fig. 3-1b. Let us note that folding close to the light line sets the periodicity a since the parallel wavevector modulus is simultaneously equal

to $\approx k_0$, ($n_{eff} \approx 1$) and $\approx \pi/a$ requiring that $a \approx \lambda_0/2$ for a fixed operation wavelength λ_0 .

The problem with such an approach is that the modulation effectively seen by the mode is very weak, and so does the slow-light bandwidth. As proposed in [Zan16], a solution to overcome this critical issue is to abandon the refractive guidance to implement a gap guidance that provides additional degrees of freedom to engineer the dispersion relation [Fra06, Not01] to implement large effective photon mass values that are out of reach from purely index-guided periodic waveguides.

The hollow-core photonic-crystal waveguide proposed in the present work is sketched in Fig. 3-1a. It is composed of a wide slot of width L_s surrounded by two PhC constructs implemented in a half-wavelength thick semiconductor membrane. The in-plane hybrid guidance is ensured on one side by gap guiding and on the other side by total-internal reflection at the slot interface. The PhC constructs are characterized by a double periodicity, as they feature a periodic waveguide of period $a = \lambda_0/2$ and a 2D square PhC mirror with a half period $a_M = a/2$. The periodic waveguide is formed by a 1D hole array in a tiny nanowire of width L_g ; it is responsible for the slowness of a guided Bloch mode with an effective index $n_{eff} \approx 1.01$, see Fig. 3-1b. The PhC crystal guarantees a partial gap guidance mechanism in the transverse x -direction for a longitudinal component of the wave vector $k_{//} \approx k_0$, similar to that encountered in PhC fibers [Bir95]. In contrast with the hybrid-clad waveguide [Zan16] for which the achievable values of n_{eff} are limited, the double periodicity allows us to independently tune and overlap the spectral ranges of slow-light in the longitudinal direction (periodicity a) and gap guidance in the transverse direction (periodicity a_M).

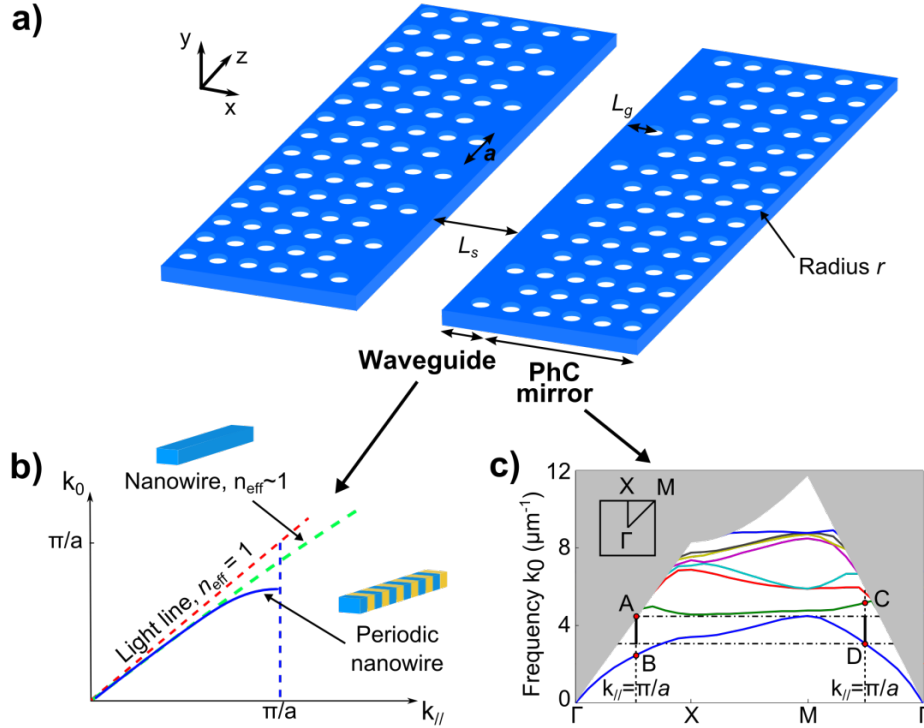


Figure 3-1. Wide-slot PhC waveguide. **a)** The waveguide is composed of a wide vacuum slot surrounded by two PhC constructs, with a double periodicity $a = 760 \text{ nm}$ for the periodic waveguide composed of a 1D hole array and $a_M = a/2 = 380 \text{ nm}$ for the 2D square PhC mirror. **b)** Periodic waveguide: a slow Bloch mode with $n_{eff} \approx 1$ is implemented by opening a band gap (solid-blue curve) in the dispersion relation (dashed-green curve) of a tiny waveguide operating close to the light line. **c)** 2D square PhC mirror: the photonic bands are computed for a period $a_M = 380 \text{ nm}$, a hole radius $r = 0.3a_M$ and a membrane thickness of 220 nm . The vertical dashed lines correspond to longitudinal (along z) momentum $k_{||} = \pi/a = \pi/(2a_M)$. The solid vertical black lines that are determined from the red dots A, B, C and D delimitate the partial band gap for $k_{||} = \pi/a$. Insets: First Brillouin zone of the PhC.

The design is performed for operation at telecom wavelength, $\lambda_0 = 1.55 \mu\text{m}$, with $a = 760 \text{ nm}$ and $a_M = a/2 = 380 \text{ nm}$. Figure 3-1c shows the photonic bands of TE-like modes supported by the square lattice of air holes of radius $r = 0.3a_M$ perforated in a half-wavelength thick semiconductor membrane ($n = 3.48$). The results computed with the MIT Photonic-Bands (MPB) package [Joh01] show that, in the spectral range of slow-light, the photonic crystal mirror does not provide a full band gap, but a partial gap for a longitudinal component of wave vector $k_{||} = \pi/a \approx k_0 \approx 4.1 \mu\text{m}^{-1}$. As shown by the thick solid black line in Fig. 3-1c, the partial gap edges at

$k_0 = 3.1 \mu\text{m}^{-1}$ and $4.13 \mu\text{m}^{-1}$, are determined from points A, B, C and D. Points A and B are determined for $k_{\Gamma X} = \pi/a$ and $k_{XM} = 0$, by the crossing between the vertical line AB with the light line (point A) and the PhC bands (point B). Similarly, points C and D are obtained for $k_{\Gamma X} = \pi/a$ and $k_{XM} = \pi/a$, by the crossing between the vertical line CD with the PhC bands. We note that a full band gap, like in classical PhC waveguides [Not01], is not required for gap guiding. As noted in a recent discussion session at the 2016 PECS meeting in York, it is even unclear what are the advantages of full- or partial-band-gap guidance over index guidance, other than the possibility to engineer the flatness of the dispersion curve. One may argue that gap guidance mitigates radiation losses due to fabrication imperfections [Pov04]. However, in the fast light regime, it is not clear that PhC waveguides provide smaller attenuations than nanowire waveguides, and in the slow light regime, scattered light is mainly backscattered (as discussed in Chapter 2) so that cladding leakage is negligible. However, for the sake of completeness, an alternative design using a full band gap PhC mirror was realized. The full band gap is obtained by elongating the periodicity of a triangular lattice in the transverse x -direction (details on the PhC mirror design are provided in Appendix 4). However, the alternative design does not improve the waveguide figures of merits, and we got identical low n_{eff} -values and flatness.

3.3 Bloch mode properties

The design of the wide-slot PhC waveguide depends on two additional parameters, the waveguide width L_g and the slot width L_s . As for classical waveguides, the width L_g controls the waveguide effective index. For small widths, the dispersion curve comes near the air light line and the field is expelled away in the cladding. On the other hand, the slot width L_s weakly impacts the dispersion curve as the electromagnetic interaction between the two PhC constructs weakens for large separation distances.

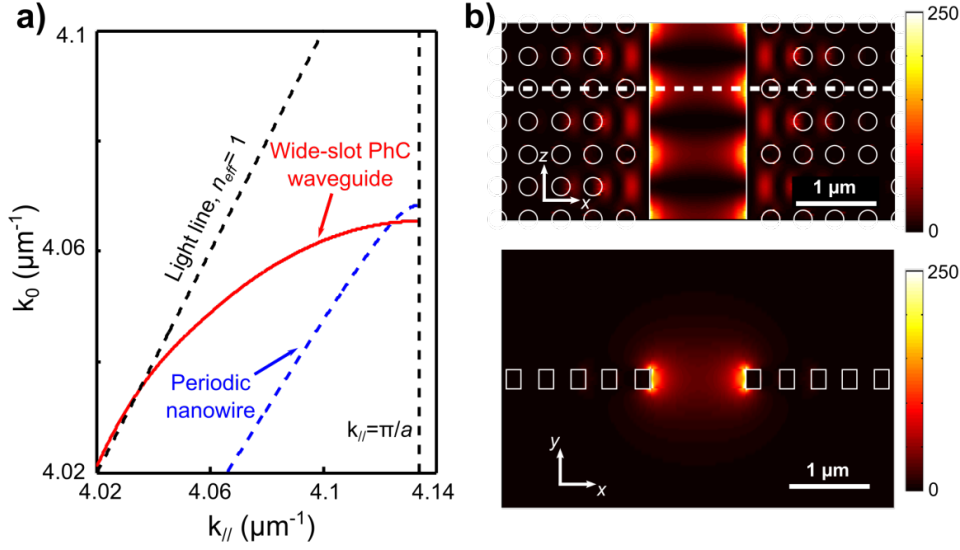


Figure 3-2. Bloch mode of wide-gap PhC waveguides. a) Comparison between the dispersion curves of a periodic nanowire waveguide (dashed-blue) and a wide-slot PhC waveguide (red). The periodic nanowire is composed of an array of semiconductor ($n = 3.48$) boxes with $220 \times 400 \text{ nm}^2$ cross section and 500 nm length. The period is $a = 760 \text{ nm}$, like the one of the PhC waveguide. The parameters of the wide-slot PhC waveguide are $L_g = 290 \text{ nm}$, $L_s = 1120 \text{ nm}$ and the membrane thickness is 220 nm . The black dashed lines represent the air light line and the edge of the first Brillouin zone. Both waveguides offer $n_{eff} \approx 1.016$ at slow speeds. b) Normalized field intensity for the wide-slot PhC waveguide in the median plane of the membrane (upper inset) and in a cross-section (lower inset) shown with a white dashed line in the upper inset. The field maps are computed for $n_g = 50$, but they are very similar at other n_g 's.

In Figure 3-2a, we plot the dispersion curve (solid-red) of a wide-slot PhC waveguide, which is computed for $L_g = 290 \text{ nm}$ and $L_s = 1120 \text{ nm}$ with the same 3D fully-vectorial Fourier-modal method used in Chapters 1 and 2 (Appendix 1). The waveguide width is chosen to achieve slow light at $\lambda_0 = 1.55 \mu\text{m}$. We have also computed the dispersion curve (dashed blue) of a periodic nanowire waveguide composed of an array of semiconductor boxes with the same period $a = 760 \text{ nm}$. The box cross-section and length (see caption for details) were chosen so that both waveguide Bloch modes have the same effective index $n_{eff} = 1.016$ at λ_0 , and thus comparable spatial extent in the air clad. As previously suggested, it is stringent that the wide-slot PhC waveguide offer a much broader slowness bandwidth than the periodic nanowire. Actually, the wide-slot effective mass obtained by fitting

the dispersion curves with a parabola, $\omega - \omega|_{k_{//}=\pi/a} = (k_{//} - \pi/a)^2 / (2m)$, is much larger, $mca = 0.12$ against $mca = 8.7 \times 10^{-3}$ for the periodic nanowire.

The intensity profiles $|\mathbf{E}|^2$ of the wide-slot PhC waveguide are displayed in Fig. 3-2b for $n_g = 50$. As expected, a significant fraction of the slot space is bathed in light. Indeed, $\sim 30\%$ of the electric energy, equal to $\frac{1}{4} \int \varepsilon |\mathbf{E}|^2 dV$ for Bloch modes, is contained in a volume of length a and cross-sectional size defined in the x -direction by the width of the slot and extending 500 nm above and below the membrane in the y -direction. Due to the evanescent character of the field in the air cladding, the intensity is minimum at the slot center. An oscillatory decaying field is also observed in the PhC mirrors, confirming that the mode is indeed gap-guided by the photonic gap. Let us notice that the electric field also expands above and below the semiconductor membrane. This expected feature may offer an additional freedom for implementing strong light-matter interaction.

3.4 Figures of merit

Two main conflicting figures of merit are important when comparing the performance of various slow-light waveguides: the normalized slowness bandwidth and the normalized field extension length in the vacuum cladding. The latter is approximately given by $L_d/\lambda = (2\pi\sqrt{n_{eff}^2 - 1})^{-1}$ and is thus directly characterized by the waveguide effective index. By assuming a quadratic expression for the dispersion relation close the band edge, $\omega - \omega|_{k_{//}=\pi/a} = (k_{//} - \pi/a)^2 / (2m)$, it is easily found that the slowness bandwidth $\Delta\omega$ imposed by a maximum group-velocity variation Δv_g is simply $\frac{\Delta\omega}{\omega} = \frac{mca}{4\pi} \left(\frac{\Delta v_g}{c}\right)^2$. From this expression, it immediately appears that the slowness bandwidth is directly characterized by the normalized effective mass mca .

Table 3-1 compares the values of L_d/λ and mca for all waveguides designed so far for implementing structural slow light with atoms, the alligator waveguide [Gob14] that is the only one tested experimentally, the hybrid-clad waveguide [Zan16], the present wide-slot PhC waveguide. For the sake of comparison the Table also includes the periodic nanowire waveguide analyzed in Fig. 3-2a.

Indeed, the periodic nanowire and the wide-slot PhC waveguides, whose periodicity has been carefully chosen to achieve low effective index values, offer the longest decay lengths ($\approx \lambda$), whereas the two other waveguides have limited lengths $\approx \lambda/3$. We also note that, for equivalent L_d/λ values, waveguides with a gap PhC guidance offer larger normalized effective masses than their counterparts with index guidance. In addition, the wide-slot PhC waveguide reaches a normalized effective mass comparable to that of the alligator waveguide whereas its decay length in vacuum is significantly larger.

	Alligator [Gob14]	Hybrid-clad [Zan16]	Periodic nanowire	Wide-slot PhC
mca	0.22	12	8.7×10^{-3}	0.12
L_d/λ	0.28	0.29	0.91	0.89

Table 3-1. Comparison of the two figures of merit for the implementation of slow light in vacuum.

In other simulations not reported here for simplicity, we tried to increase further the mass of the wide-slot PhC waveguides, by transversally shifting the 1D periodic hole array of the waveguide channel or by considering hexagonal lattices for the mirror. Indeed, we were able to increase the mass while maintaining the decay length, but disappointingly, only small increases were obtained from $mca = 0.12$ to 0.14. We do not know if these values are close to a fundamental limit, or if better designs may make a significant difference.

3.5 Atom-photon coupling

In order to analyze the performance of the wide-slot PhC waveguide, it is important to quantify the electromagnetic coupling between an atom trapped in the slot and the photonic Bloch mode. The key figure of merit used in many studies related to photon-emitter coupling experiments and computations [Arc14, Ble11, Fae14, Lec07b] is the β -factor, which represents the fraction of the total light emitted by a linearly polarized dipole oscillator that is coupled into the guided mode. The β -factor can be expressed as $\beta = 2\gamma_M/(2\gamma_M + \gamma')$, with γ_M the decay rate into the guided mode and γ' the decay into all other radiation decay channels. The factor 2 accounts for the coupling in both directions of the waveguide. For truly-guided Bloch modes with an electric field $\mathbf{E}(r)$, the decay rate γ_M normalized by the decay rate γ_0 of the same oscillator in free-space is simply $\gamma_M/\gamma_0 = 3/(8\pi) n_g \lambda^2 a/V_{eff}$, with $V_{eff} = \iiint_{unit\ cell} \varepsilon(r) |\mathbf{E}(r)|^2 dr^2 / |\mathbf{u} \cdot \mathbf{E}(r_S)|^2$ [Lec07a]. In the previous expression, r_S and \mathbf{u} denote the position and orientation of the linearly-polarized dipole oscillator, and $\varepsilon(r)$ the waveguide relative permittivity. It clearly indicates that the interaction is driven by two main quantities: the group index n_g and the mode volume V_{eff} .

The β -factor can straightforwardly be evaluated from the normalized Bloch-mode field distribution by assuming that γ' is equal to γ_0 . As shown in a recent study [Zan15], this assumption is likely to be valid for the wide-slot geometry, especially for atoms trapped in the middle of the wide slot and for large n_g 's since $\gamma_M \gg \gamma_0$.

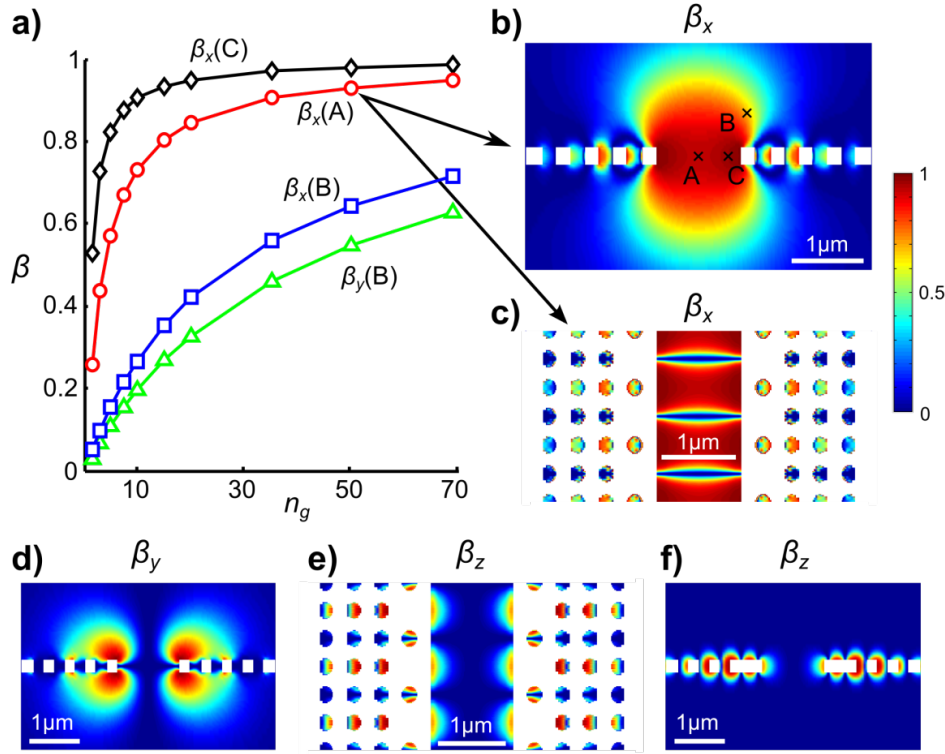


Figure 3-3. Atom-photon coupling in the wide-slot PhC waveguide. **a)** Dependence of the β -factor with n_g for dipoles polarized along the x -direction (red circles, blue squares and black diamonds) or the y -direction (green triangles). Three dipole locations are considered: points A and C are located in the median plan at 560 nm and 150 nm from the nearest slot facet, and point B is located 500-nm above the periodic waveguide. **b)-c)** β -factor maps for a x -polarized dipole located in the main symmetry planes of the waveguide for $n_g = 50$. **d)** β -factor maps for a y -polarized source in the same cross-section as **(b)**. **e)** β -factor maps for a z -polarized source in the same plane as **(c)**. **f)** β -factor maps for a z -polarized in a cross section where the β -factor is maximum in the slot. **b-f)** β -factors are displayed only in vacuum. The same scale is used for all maps.

Figure 3-3 gathers the main relevant computational results obtained for the β -factors for the three dipole orientations. The β -factors strongly increase with the group index n_g , as evidenced by Fig. 3-3a obtained for 3 different atom locations shown with the points A , B and C in Fig. 3-3b. Due to the extremely small effective index value, the coupling is remarkably large even for small n_g 's. At point C (located 150-nm away from the slot facet), the coupling efficiency is as high as 90% for a group index of only 10. A noteworthy efficiency of 95% for $n_g = 50$ is achieved for a x -polarized

dipole in the middle of the slot at point *A* situated 560-nm away from any interface.

As shown in Figs. 3-3b-c, the coupling efficiency β_x to *x*-polarized dipoles is very high in a wide area comprising the slot and a fraction of the vacuum spaces above and below the membrane. The coupling to *y*-polarized dipolar oscillators β_y is null in the median plane of the membrane for symmetry reason and is thus very weak in the slot (Fig. 3-3d). Similarly the coupling to *z*-polarized dipolar oscillators β_z is extremely weak in the slot (Figs. 3-3e-f). All this shows that the coupling in the slot area is almost completely achieved with the *x*-polarized field.

The coupling outside the slot area, above and below the membrane, is also an important characteristic of the wide-slot waveguide that may be exploited in experiments. In this area, the coupling to *z*-polarized dipolar oscillators remains negligible (Fig. 3-3f), but both β_x and β_y are large. As shown by the coupling maps of Figs. 3-3b and 3-3d, β_x is especially large over wide spaces that spread far away above and below the slot area, while β_y is the dominant coupling mechanism above and below the periodic waveguide channels on both sides of the slot.

Additionally, since the slot is large and the electromagnetic interaction between the waveguide channels is weak, it is anticipated that a mono-channel waveguide construct would offer β -factor maps similar to those reported here, together with an entire half-space to conveniently load and trap the atoms.

3.6 Conclusion

Cold atoms that interact almost exclusively with just a single propagating optical mode constitute a nearly ideal photon-matter interface with many applications in quantum information processing. We have explored an

ultimate regime of interaction for which the atoms are trapped away from any material interfaces and decoherence effects are kept at a minimum level.

In general, achieving strong and remote couplings address two conflicting objectives, and the proposed slow wide-slot PhC waveguide geometry offers a good trade-off. Its particularity is the double periodicity that enables to both control the mode confinement and slowness bandwidth, at least up to a certain extent. Notably, we have shown that the engineering of the modal properties could enable slow hollow-core Bloch modes with a significant fraction, $\sim 30\%$, of the field in vacuum. The designed structure achieves an unprecedented strong waveguide-atom couplings, $\sim 95\%$, at a remarkably large $\lambda/3$ separation distance from any materials, while offering a slowness bandwidth comparable to that achieved in recent realizations [Gob14].

However, the present design is certainly not optimal, and more theoretical and numerical investigations are needed to understand how to enlarge the slowness bandwidth by a better control of the penetration length of PhC mirrors operating with a longitudinal component of the wave vector $k_{//} \approx k_0$. It would also be interesting to understand how to design slow waveguide constructs for which the balance between confinement and bandwidth can be gradually tuned. Besides the cold atom field, the present waveguide that offers a remarkably large volume of high field may open interesting perspectives for sensing, especially at low concentration.

Chapter 4 - MODAL ANALYSIS OF THE TEMPORAL RESPONSE OF PLASMONIC RESONATORS

4.1 Introduction

Plasmonic structures, in addition to their ability to confine light in deep sub-wavelength volumes through collective excitation of electrons at metallic-dielectric interfaces, undergo ultrafast dynamics at timescales down to sub-femtosecond due to their broad spectral bandwidth. As a result, broadband excitation of plasmons by femtosecond lasers allows to control light-matter interaction with nanometric precision at femtosecond timescales [Sto02]. Combining high spatial and temporal confinements in plasmonic systems has repercussions in fields as diverse as material science, cell biology and quantum optics [Pia16] and, in addition to fundamental interests, has enabled to build intense high energy light sources [Kim08b], ultrashort electron sources [Vog15] or high contrast nanoscale probes [Ber10] by inducing strong non-linear optical phenomena.

Of particular interest is the temporal response of plasmonic nanoresonators, as represented by the scattering problem in Fig. 4-1, where the excitation by a given optical pulse gives rise to a spatially varying electric field with complex temporal evolution. The prospect of accessing experimentally this temporal response has stimulated the development of various, increasingly sophisticated, spatially resolved techniques based on optical microscopy [Han09, Bri13, Acc14], electron microscopy [Kub05, Bar09b, Aes10] or scanning near-field optical microscopy [Oni13, Nis15, Kra16b]. Such development is continuously fed by new theoretical proposals and discussions [Sto07, Aes16].

However, the measurements reported so far are interpreted or analysed using simple damped harmonic oscillator models [Kub05, Han09, Bri13, Acc14, Nis15, Kra16b, Aes16], only valid for simple samples and/or experimental conditions, or interpreted using classical numerical simulations (performed either in the spectral domain [Sun13] or in the time domain [Mar15] using Finite-Difference Time-Domain (FDTD) solvers). Overall, these simulations do not always provide a clear insight on the underlying physical processes. To the best of our knowledge, general and intuitive yet rigorous theoretical tools do not presently exist.

In this chapter, relying on recent advances on the modeling of plasmonic nanoresonators [Sau13, Bai13], we develop a semi-analytical modal approach to model the temporal response. In the approach, the scattered field is expanded in a basis formed by the quasi-normal modes (QNMs), i.e. the natural resonant modes of the resonator. If the scattering process can be accurately modelled with the excitation of a few dominant resonant modes, the modal approach provides a fast and intuitive tool to describe the temporal response of complex plasmonic structures. The physics required to understand experimental results is then made readily available and unambiguous, in sharp contrast with more widespread classical scattering theories that do not intrinsically rely on the natural modes of the resonator. Moreover, the general and versatile character of the modal formalism can be used advantageously to predict and interpret spatio-temporal control schemes of plasmonic structures [Sto02, Hua09, Aes10], design original geometries and develop new applications in the field of ultrafast nanoplasmonics. After emphasizing the gain brought by the modal method to interpret experimental measurements, we will quantitatively test its precision and versatility by comparing the results obtained on a complex plasmonic structure with those obtained using widespread numerical methods.

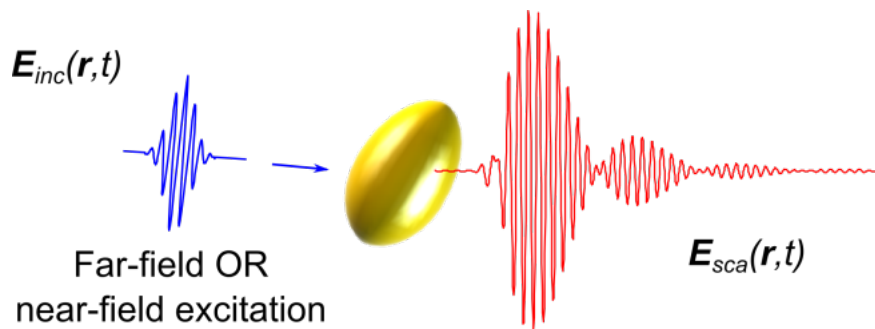


Figure 4-1. Scattering problem. An incident optical pulse $\mathbf{E}_{inc}(\mathbf{r}, t)$, which may be a far or near-field excitation, drives a plasmonic resonator and gives rise to a locally varying scattered field $\mathbf{E}_{sca}(\mathbf{r}, t)$.

4.2 Theoretical Method

In the vast majority of classical electromagnetic methods, the interaction between light and nanoresonators is described via continuum (scattering) theory with classical Maxwell's equation solvers, operating either in the frequency-domain with real frequencies, or in the time domain. The FDTD method for instance is almost hegemonically used by experimentalist groups nowadays. Nevertheless, the core physical concepts attached to the resonator, the resonance modes, are only indirectly accessed with such descriptions. Thus interpretation is not straight ahead and *the high "simplicity" of the physics is not always revealed*. In contrast, since it explicitly relies on the natural resonator modes, the present treatment restores analyticity and intuition into the modeling, closing the huge gap presently existing between nanoresonator physics and modeling tools.

Contrary to quasistatic eigenmodes [Sto02], which are solutions of the Poisson equation, QNMs are solutions of the full set of Maxwell equations, and can be used to model resonators with large sizes, much greater than a few tens of nanometers. Let us start by considering QNM expansions in the spectral domain. In the scattering field formulation, the total field is decomposed as a sum of a driving field $\mathbf{E}_{inc}(\mathbf{r}, \omega)$ at frequency ω and a scattered field $\mathbf{E}_{sca}(\mathbf{r}, \omega)$. As shown in [Bai13], the field scattered by the plasmonic nanoresonators can be expanded in a QNM basis, and provided

that few resonance modes are dominantly excited, $\mathbf{E}_{sca}(\mathbf{r}, \omega) \approx \sum_m \alpha_m(\omega) \mathbf{E}_m(\mathbf{r})$, the expansion provides accurate closed-form expressions even for strong radiation leakage, absorption and material dispersion. The coupling coefficient $\alpha_m(\omega)$ is simply obtained by an overlap integral between the normalized mode and the driving field $\alpha_m(\omega) = -\omega \iiint \Delta\epsilon(\mathbf{r}, \omega) \mathbf{E}_{inc}(\mathbf{r}, \omega) \cdot \mathbf{E}_m(\mathbf{r}) d\mathbf{r}^3 / (\omega - \omega_m)$, where ω_m is the complex frequency of the m^{th} mode and $\Delta\epsilon(\mathbf{r}, \omega)$ the permittivity difference between resonator and background medium [Bai13].

In principle, to be accurate, the expansion requires to consider many QNMs. In the 90's, key theoretical works [Leu94a, Leu94b] have nicely established the completeness of the QNM expansion for simple open systems, e.g. 1D systems and 3D spherical dielectric resonators surrounded by a uniform background. More recently, interesting numerical results [Via14] have shown that the expansion provides remarkably accurate predictions for the scattering cross-section of 2D dielectric (non-dispersive) resonators and TE polarization, provided that the continuum of radiation QNM is included in the expansion, see also [Doo13]. However, completeness for the general case of 3D systems made of absorbent and dispersive media, especially if surrounded by complex backgrounds, remains an open question.

In the following, we assume that only a few dominant QNMs in the expansion are sufficient to achieve a meaningful modeling. The advantage is that the interpretation remains simple, the calculations are very fast and, as we will see, the predictions remain very accurate in the near-field of the resonator, as already discussed in [Sau13, Bai13].

Referring to Fig. 4-1, we now consider that the driving field is an optical pulse, $\mathbf{E}_{inc}(\mathbf{r}, t)$, i.e. a wave packet that can be Fourier transformed $\mathbf{E}_{inc}(\mathbf{r}, t) = \int_{-\infty}^{+\infty} \mathbf{E}_{inc}(\mathbf{r}, \omega) \exp(i\omega t) d\omega$, with $\mathbf{E}_{inc}(\mathbf{r}, \omega)$ the frequency spectrum of the pulse. Driven by the incident optical pulse, the plasmonic resonator scatters a time-dependent electromagnetic field, $\mathbf{E}_{sca}(\mathbf{r}, t)$. Every

infinitesimal component $\mathbf{E}_{inc}(\mathbf{r}, \omega)d\omega$ of the driving field gives rise to an infinitesimal scattered field $d\mathbf{E}_{sca}(\mathbf{r}, \omega)$ which is conveniently expanded as a sum of QNM modes $d\mathbf{E}_{sca}(\mathbf{r}, \omega) \approx \sum_m d\alpha_m(\omega) \mathbf{E}_m(\mathbf{r})$ with

$$d\alpha_m(\omega) = \frac{-\omega d\omega}{\omega - \omega_m} \iiint \Delta\varepsilon(\mathbf{r}, \omega) \mathbf{E}_{inc}(\mathbf{r}, \omega) \cdot \mathbf{E}_m(\mathbf{r}) d\mathbf{r}^3. \quad (4-1)$$

Assuming that the scattered field can be inverse Fourier transformed, we then obtain the scattered field in the time domain by summing up all the frequency components, $\mathbf{E}_{sca}(\mathbf{r}, t) = \int_{-\infty}^{+\infty} d\mathbf{E}_{sca}(\mathbf{r}, \omega) \exp(i\omega t)$. The latter can be conveniently expressed as

$$\mathbf{E}_{sca}(\mathbf{r}, t) \approx \sum_m \beta_m(t) \mathbf{E}_m(\mathbf{r}), \quad (4-2)$$

with

$$\begin{aligned} \beta_m(t) &= \int_{-\infty}^{+\infty} d\alpha_m(\omega) \exp(i\omega t) \\ &= \int_{-\infty}^{+\infty} \frac{\omega \exp(i\omega t)}{\omega_m - \omega} \iiint \Delta\varepsilon(\mathbf{r}, \omega) \mathbf{s}(\mathbf{r}, \omega) \cdot \mathbf{E}_m(\mathbf{r}) d\mathbf{r}^3 d\omega. \end{aligned} \quad (4-3)$$

Because of the linearity in the time-domain, the scattered field remains a sum of QNM modes with time-dependent excitation coefficients, the $\beta_m(t)$'s. Moreover, the total field, $\mathbf{E}_{sca}(\mathbf{r}, t) + \mathbf{E}_{inc}(\mathbf{r}, t)$, is simply given by a sum of independent contributions, analytically known from the sole knowledge of the QNM mode profile in the resonator, the resonance frequency and the driving field. Equations 4-2 and 4-3 provide a very simple and intuitive description of the temporal response of nanoresonators.

Let us note that the formalism is valid for any driving field, e.g. a field scattered by another resonator, a dipole emission in the near-field of the resonator or a far-field focused laser pulse. Hereafter we will consider a plane-wave driving field, a pulse propagating towards the positive z direction defined in the spectral domain by

$\mathbf{s}(\mathbf{r}, \omega) = \mathbf{W}g(\omega - \omega_0)\exp(-ik(\omega)z)$, with ω_0 the central frequency of the pulse, $k(\omega)$ the wavevector modulus in the background medium, g the frequency spectrum of the pulse and \mathbf{W} the 3×1 electric-field vector of the plane wave. Substituting into the expression of $\beta_m(t)$, we obtain

$$\beta_m(t) = \int \frac{\omega \exp(i\omega t) g(\omega - \omega_0)}{\omega_m - \omega} \iiint \Delta\varepsilon(\mathbf{r}, \omega) \exp(-ik(\omega)z) \mathbf{W} \cdot \mathbf{E}_m(\mathbf{r}) d\mathbf{r}^3 d\omega.$$

The $\beta_m(t)$'s are easily calculated in practice. The most difficult part consists in computing and normalizing the few dominant QNMs. For that purpose, we use the method described in [Bai13] and the associated freeware implemented with COMSOL Multiphysics, a commercial finite-element software. To simplify, the frequency dependence of $\Delta\varepsilon(\mathbf{r}, \omega)$ and $\exp(-ik(\omega)z)$ in the spectral window defined by the resonance term $1/(\omega - \omega_m)$ is neglected hereafter, so that the spatial integral is performed only once at a single frequency equal to $\text{Re}(\omega_m)$. We have numerically checked that that accounting for the dispersion by calculating the spatial integral for every frequency gives almost the same results in the following examples (see Appendix 6). Finally, the integral over ω in $\beta_m(t)$ is performed using a fast Fourier transform algorithm. The present formalism is thus very easy to implement. Indeed, once the few dominant QNMs are computed, any change in the driving field (polarization, propagation direction, central frequency, pulse duration, etc.) is straightforwardly taken into account because of the analyticity with the driving field, in sharp contrast with the FDTD method that requires to re-perform the entire computation for every instance of the driving field.

4.3 PEEM experimental data

To evidence the benefit brought by QNM expansions to interpret measurements of ultrafast resonator dynamics, we start by reviewing the difficulties encountered when interpreting experiments with available modeling tools. For the sake of illustration, we consider interferometric time-

resolved PEEM measurements recently performed on silver rice shaped nanoparticles (inset of Fig. 4-2a).

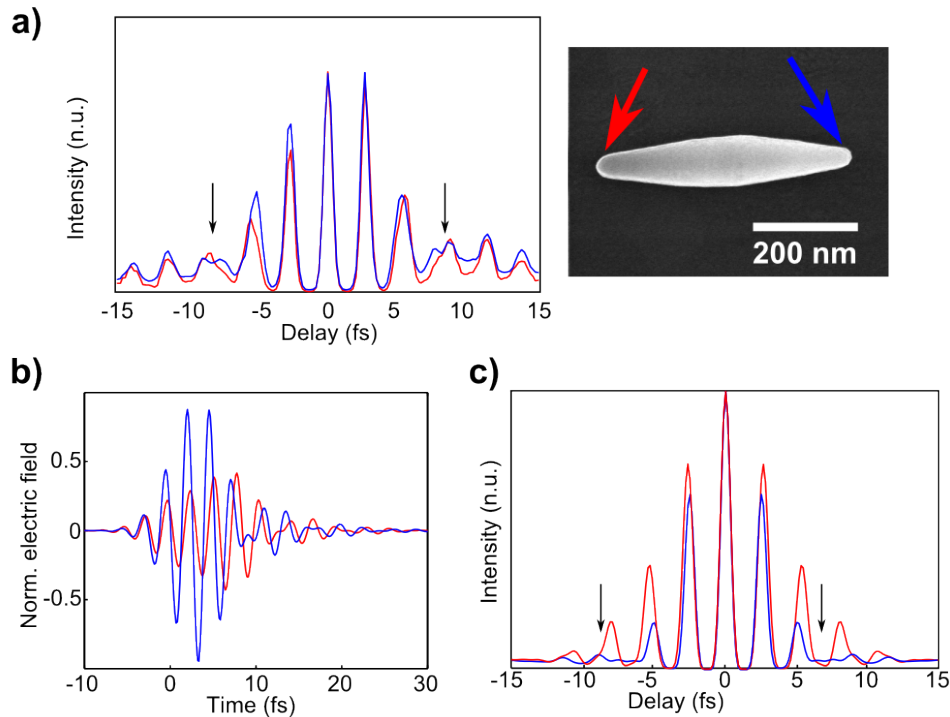


Figure 4-2. Experimental measurements and FDTD calculations. **a)** Non-linear autocorrelation of the fields induced by ~ 6 -fs laser pulses at the two ends of a rice-shaped silver nanoparticle, measured by interferometric time-resolved PEEM. Each curve is normalized to its maximum. The black arrows evidence a duplication of the intensity peaks, suggesting markedly-different time-evolutions for the two fields. The inset shows a Scanning Electron Microscope image of the rice shaped silver nanoparticle. The colored arrows indicate the ends that correspond to the colored curves. Details of the experimental parameters can be found in [Mar15] and in Fig. 4-3a. **b)** Normalized time-evolution of the fields at the two ends of the nanoparticle, obtained from FDTD computations. **c)** Non-linear normalized autocorrelation of the fields shown in **(b)**. Consistently with the experimental data in **(a)**, the autocorrelation functions are markedly different for delays > 5 fs and < 10 fs, see the black arrows **(c)**.

In the experiment [Mar15], the nanoparticles were randomly deposited on an glass substrate covered with ITO and illuminated by ~ 6 fs laser pulses. Autocorrelation measurements of the induced plasmonic fields at the particle ends (indicated by the blue and red arrows) were performed by splitting the laser pulses into two identical replicas delayed by a controlled amount of time, and by recording PEEM images of the rice particle for varying delays. Importantly, we observed that the autocorrelation functions of the intensity

spots imaged at the two ends of the particles were systematically and markedly different for delays > 5 fs and < 10 fs, see the black arrows in Fig. 4-2a, suggesting a complex time evolution of the plasmonic fields at the nanoparticle ends that we were not able to fit with simple analytical models [Mar15].

To support the observations, FDTD calculations were performed. Consistently with the experiment, they predicted a complex temporal evolution of the plasmonic fields (Fig. 4-2b) which allow us to qualitatively reproduce the near-field autocorrelation measurements, see Fig. 4-2c. The complex temporal evolution was attributed to the interplay between (i) the non-normal incidence wide field and broadband excitation and (ii) the particles whose size leaves the quasistatic regime, and which support several eigenmodes. This interplay leads to a delocalized induction of intricate surface wave packets over the particle that interfere with each other as well as with the excitation pulses. However, the details of such interference could not be captured from the field calculated by FDTD, and the interpretation of the experiment thus remained limited. In contrast, by disentangling the intrinsic properties of the object from the excitation, the present QNM expansion method allows an in-depth interpretation of the temporal evolution of the field probed by the PEEM experiment.

4.4 Interpretation of the PEEM experimental data

To compute the QNMs, we model the nanorice shaped particle as an ellipsoid of length 600 nm and radius 50 nm positioned just above a substrate of permittivity 2.1 (see Fig. 4-3a). The permittivity of silver is approximated by a Drude model with plasma frequency of 1.25×10^{16} rad/s and relaxation rate of 1.6×10^{14} s $^{-1}$. In order to match the experimental conditions, we consider a plane wave illumination with a 5.5 femtoseconds Fourier limited Gaussian pulse of central frequency $\omega_0 = 2.43 \times 10^{15}$ rad/s, p-polarized and propagating with an angle of 25° with respect to the substrate (Fig. 4-3a). In the spectral

range spanned by the pulse, the nanorice deposited on the substrate supports two dominant QNMs whose mode profiles in the plane of incidence are shown in Fig. 4-3b. Their respective complex resonance frequencies are $\omega_1 = 2.08 \times 10^{15} (1 + i/(2Q_1))$ rad/s and $\omega_2 = 2.95 \times 10^{15} (1 + i/(2Q_2))$ rad/s, $Q_1 = 5.4$ and $Q_2 = 8.1$ being the quality factors of the resonances. The QNMs are independent from the driving field and are thus either symmetric (mode 1) or anti-symmetric (mode 2) with respect to the small axis of the ellipsoid. Due to the presence of the substrate, a small asymmetry is present with respect to the long axis of the ellipsoid.

In Figs. 4-3c-e, we show the three contributions to the total field at the two ends of the particle, denoted by points A and B in Fig. 4-3a. In accordance with [Mar15], we solely consider the z component of the field as it is the main component driving the nonlinear photoemission process in the experiment [Mar15]. The driving field is shown in Fig. 4-3c. Because of the oblique incidence, a phase delay corresponding to the propagation distance between points A and B is observed. The fields scattered by the modes 1 and 2 are shown in Figs. 4-3d and 4-3e. They resemble the usual temporal response of any dissipative resonators (or damped harmonic oscillators) with markedly different oscillation frequencies equal to $\text{Re}(\omega_m)$, and with a relaxation (by absorption and scattering) at a decay rate fixed by $\text{Im}(\omega_m)$. Referring to Eq. 4-2, since the coupling coefficients β_1 and β_2 do not depend on the position \mathbf{r} , the spatial dependence of the response of every individual mode is solely determined by the mode profile. Accordingly, the mode responses at all spatial locations have all the same normalized envelop, only the amplitudes or phases may differ. In the present case, the fields scattered by mode 1 at both ends are identical by symmetry, and the fields scattered by mode 2 are π -phase shifted (see Fig. 4-3b).

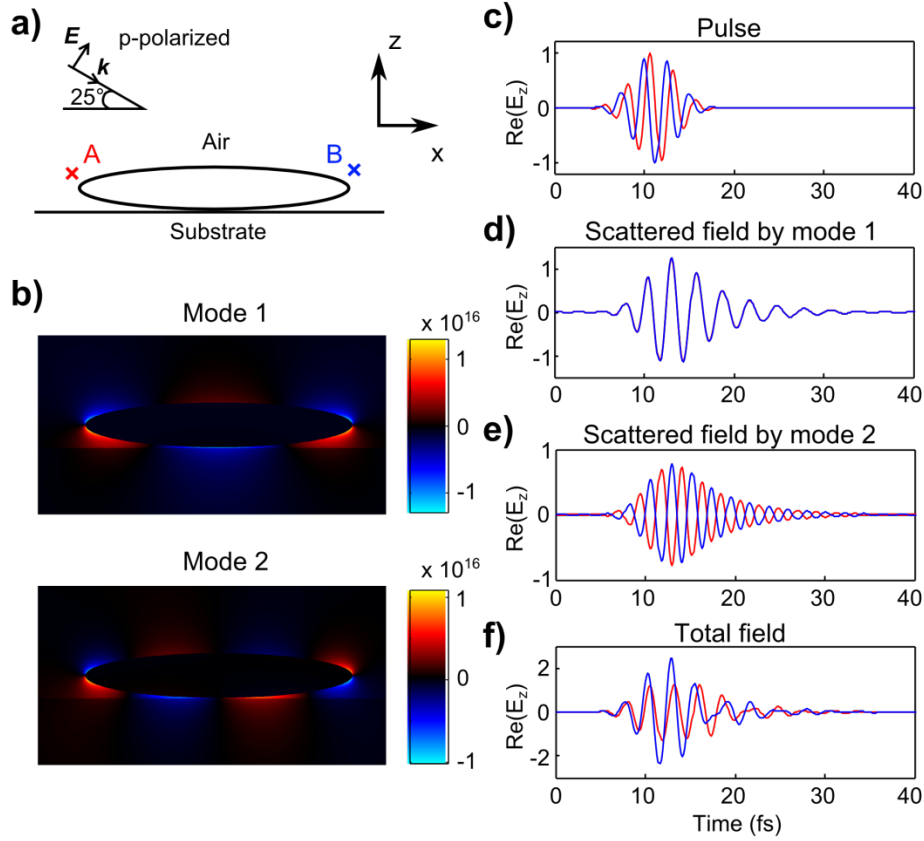


Figure 4-3. Modal analysis of the nanorice temporal response. **a)** The nanorice is deposited on a glass substrate and illuminated by a p-polarized 5.5-fs plane-wave Fourier limited Gaussian pulse of central frequency $\omega_0 = 2.43 \times 10^{15}$ rad/s¹ propagating with a 25° incidence degree with respect to the substrate. **b)** E_z -profile of the normalized dominant QNM modes. **c-f)** Temporal profile of the E_z field-component computed at point A (red) and B (blue). **c)** Driving pulse, which includes the reflection of the incident plane wave on the substrate in the absence of nanorice. **d)** Fields scattered by mode 1 (they are the same due to the mode symmetry). **e)** Fields scattered by mode 2. **f)** Total field.

The resulting total field (Fig. 4-3f) is given by the sum of the three contributions. The responses are different at the two ends. Notably, the signal envelopes strongly differ from one another, both in amplitude and shape. In addition, the interference induces different oscillation distortions during the relaxation for 15-25 fs delays, and a slight initial retardation of the red signal due to the incident pulse. The QNM model qualitatively corroborates the observations in [Mar15] and predicts the FDTD calculations in Fig. 4-2b (the parameters in the two calculations are slightly different, and thus only qualitative agreement can be found). However, the decomposition

into different contributions in the modal formalism brings new insights on the underlying phenomena and greatly eases the interpretation. For instance, it clearly appears that the oscillation distortions results from interferences between the two QNMs, creating a beating at the frequency $\text{Re}(\omega_2 - \omega_1)$ that is comparable to the central frequencies of the driving pulse. Thus the beating period is similar to the oscillation period, and the FDTD computational results showing the distortion are difficult to interpret directly. Additionally, since the phase of the different contributions are different at the two ends, the resulting interferences selectively modify both the envelope and oscillations of the response. Overall, by identifying the individual contributions of the resonance modes, the present QNM-expansion method provides unique insights and new clues for quantitatively interpreting time-resolved measurements of the ultrafast dynamics of nanoresonators, which are difficult to assess with classical frequency- or time-domain methods.

4.5 Quantitative test of the modal formalism

The previous analysis on nanorices was meant to demonstrate the potential of the present method to intuitively interpret experimental measurements. Hereafter we aim at showing the versatility of the modal expansion and at testing its strength and weaknesses. We thus study a more complex geometry and compare the QNM-expansion predictions with numerical data obtained with the FDTD method as well as with fully-vectorial Finite-Element Method (FEM) calculations.

We chose a Dolmen nanostructure composed of three gold nanorods. The Dolmen provides a richer physics than the nanorice, with a Fano response resulting from the interference of out-of-phase modes [Ver09, Lov13] that can be exploited for sensing and realizing induced transparency in plasmonic metamaterials [Zha08]. The Dolmen is represented in Fig. 4-4a and the relevant geometrical parameters are given in the caption.

In the following computations, it is illuminated by a 12.7 fs plane-wave Fourier limited Gaussian pulse (central frequency $\omega_0 = 2.90 \times 10^{15}$ rad/s) propagating in the z -direction and linearly polarized along the $\hat{x} + 2\hat{y}$ direction (\hat{x} and \hat{y} are the unitary vectors along the x - and y -axis). At visible frequencies, the Dolmen supports three dominant QNMs. Their normalized intensity distributions are plotted in Figs. 4-4b-d. Their complex resonance frequencies are $\omega_1 = 2.70 \times 10^{15}(1 + i/(2Q_1))$ rad/s, $\omega_2 = 2.97 \times 10^{15}(1 + i/(2Q_2))$ rad/s and $\omega_3 = 3.11 \times 10^{15}(1 + i/(2Q_3))$ rad/s with $Q_1 = 19.1$, $Q_2 = 23.1$ and $Q_3 = 8.7$. Modes 1 and 2 preferably couple to x -polarized driving fields and mode 3 preferably couples to y -polarized fields. For the sake of understanding, the in-plane equivalent electrical dipoles of the nanorods, determined from the field lines, are depicted with white arrows in the figure.

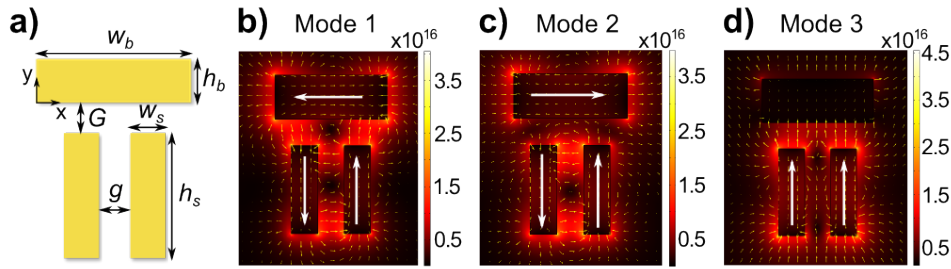


Figure 4-4. QNMs of the Dolmen. **a)** The Dolmen is composed of 3 gold rods. The geometrical parameters are $h_t = 100$ nm, $w_t = g = G = 30$ nm, $h_s = 50$ nm and $w_s = 128$ nm. The three rods have a thickness of 20 nm. **b-d)** Intensities of the normalized QNM modes (the yellow tiny arrows represent the local E-field direction). The white arrows represent the equivalent electric dipoles of each rod. For the simulations, the gold permittivity is approximated by a Drude model with a plasma frequency of 1.365×10^{16} rad.s $^{-1}$ and a relaxation rate of 3.2×10^{13} s $^{-1}$. The Dolmen is in air with a background refractive index of 1.

The FDTD calculations are performed with the FDTD Solutions software from Lumerical. We use typical parameters for convergent simulations using total-field scattered-field sources (computational box size of $800 \times 800 \times 800$ nm 3 , 64 PML layers, mesh override region with mesh size of $0.25 \times 0.25 \times 0.25$

nm³ containing the nanorods), resulting in CPU times of the order of a few days on an Intel i7-4770K CPU, 3.50 GHz, 16 GB RAM PC. The FDTD methods allow to calculate the temporal response of the dolmen for any driving pulse with a single run [Hua09].

The Dolmen QNMs are computed and normalized with the radio frequency module of COMSOL Multiphysics using the freeware in [Bai13], with a simulation space of radius 600 nm, a PML layer of thickness 300 nm and second-order finite elements. An extremely refined mesh ($\sim \lambda/300$) is used close to the rice surface to finely sample the rapid variations of the field. In total, 329000 tetrahedral elements are considered. To compute the QNM, we use two mirror-symmetry planes. Only 11 min are required to compute and normalize every individual QNM with the very fine mesh, using the iterative pole search method [Bai13], with an Intel Xeon(R) E5-2637 CPU, 3.50 Ghz, 64 Go RAM PC. The CPU time to compute the $\beta_m(t)$ of Eq. 4-3 is negligible < 1 s and is dominantly due to the computation of the volume integral with COMSOL Multiphysics. We use the Fast-Fourier-Transform algorithm of Matlab to compute the 1D Fourier transform.

Figure 4-5a compares the FDTD- and QNM-method predictions for the x -component of the total electric field, $\mathbf{E}_x(t, \mathbf{r}_A)$ computed at point $A = (-5, -10, 0)$ nm. Overall, a good agreement is obtained. Both methods evidence a clear signature of mode beating, with a beating period much greater than that previously observed for the nanorice case due to the small frequency difference between the modes. However, a more attentive inspection reveals two main discrepancies. First, the QNM treatment predicts oscillation amplitudes that are larger than those obtained with the FDTD method, the difference being especially stringent for the first beating. Second, the responses are in quadrature for large t 's and slightly shifted for small ones, as respectively shown in the right and left lower insets.

· https://kb.lumerical.com/en/layout_analysis_test_convergence_fDTD.html

To have a deeper insight into inaccuracy issues, we have performed frequency-domain computations with COMSOL Multiphysics, using the same fine mesh as the one used for the QNM computations. The dots in Fig. 4-5b show the field $\mathbf{E}_{sca,x}(\omega, \mathbf{r}_A)$ scattered by the Dolmen at point A under illumination by an harmonic plane wave with the same incident angle and polarization vector as before, and with an electric field $\mathbf{E}(\omega, \mathbf{r}) = \left(\frac{\hat{x}}{\sqrt{5}}, \frac{2\hat{y}}{\sqrt{5}}, 0\right) \exp\left(-i\frac{\omega}{c}z\right)$. The computation was performed for 100 frequencies ranging from $\omega = 2 \times 10^{15}$ to 4×10^{15} rad/s and the CPU time per frequency point is 3.5 min on average. We have also computed the scattered field computed with the QNM expansion, $\mathbf{E}_{sca,x}(\omega, \mathbf{r}_A) \approx \sum_{m=1,2,3} \alpha_m(\omega) \mathbf{E}_m(\mathbf{r})$, with the α_m 's given by Eq. 4-1, see the red-solid curve. We used the same fine mesh to minimize numerical dispersion, so that the discrepancies between the fully-vectorial FEM results and the QNM-expansion results directly assess inaccuracy issues inherent to QNM expansions with a small number of QNMs.

Clearly, although it only qualitatively predicts the magnitude of the spectral response, the QNM formalism quantitatively predicts the Fano response. It is especially remarkable that the complex shape can be unambiguously attributed to the interference between modes 1 and 2 (blue solid curve) and that the frequencies of the extrema of the complex spectral response are all accurately predicted with an expansion involving only 3 QNMs (red curve). This evidences that the physics of the electromagnetic interaction between the three nanorods is well captured by the QNM formalism and that the discrepancy between the fully-vectorial (dots) and QNM-expansion (red-solid) data corresponds to higher-order QNMs that are neglected in the expansion and are likely to exhibit rather smooth spectral responses in the spectral range of interest, away from their own resonance frequencies.

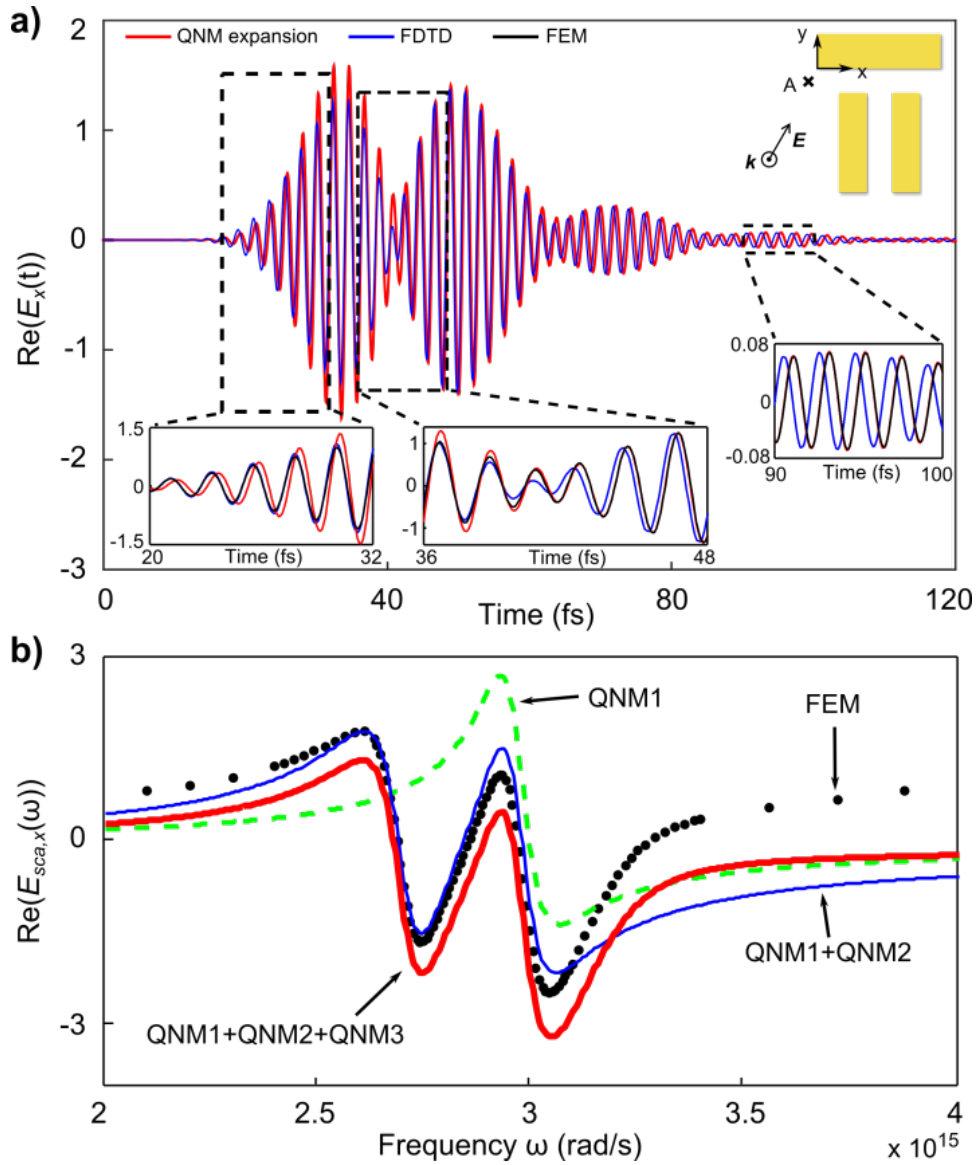


Figure 4-5. Temporal and spectral analysis of the Dolmen. **a)** Comparison of the temporal responses computed at point $A = (-5, -10, 0)$ nm with the FDTD method (blue) and the QNM-expansion formalism (red), for a 12.7-fs Gaussian incident pulse polarized along the $\hat{x} + 2\hat{y}$ direction, see the upper-right inset. Bottom-left/center/right insets: Enlarged views of the temporal response. The black curves represent the temporal response obtained by Fourier transforming the data computed with the fully-vectorial FEM and shown in **(b)**. **b)** Spectrum of the field scattered by the Dolmen at A under illumination by a plane wave with a unit amplitude and with the same polarization as in **(a)**. The dots are data computed with COMSOL Multiphysics. The coloured curves show the contributions of modes 1, 1+2, and 1+2+3, see the main text for more details.

It is tempting to attribute the deviation between the FDTD and QNM methods in Fig. 4-5a to the QNM-expansion inaccuracies revealed in Fig. 4-5b. To evidence that it is not that simple, we have computed $\mathbf{E}_x(t, \mathbf{r}_A)$ from the fully-vectorial data obtained for the frequency response $\mathbf{E}_{sca,x}(\omega, \mathbf{r}_A)$ with COMSOL Multiphysics, using a Fourier transform to go back to the time domain. The new FEM data, which are shown with black curves in the lower insets of Fig. 4-5a, led to three conclusive remarks.

At small t 's, the fully-vectorial FEM results quantitatively agree with the FDTD results, evidencing that the initial temporal response is only qualitatively predicted with the QNM formalism. It is reasonable to assume that the initial pulse excites higher-order QNMs with larger complex frequencies, which are neglected. At intermediate t 's (central inset), a transition regime is observed, in which the fully-vectorial FEM results, initially in perfect agreement with the FDTD results, start to depart from the FDTD data and become nearly superimposed with the QNM-expansion results. The transition regime occurs for $t \approx 40$ fs, which approximately corresponds to the end of the crossing with the driving pulse and beginning of the relaxation of the three dominant QNMs. It is thus a characteristic time such as the impact of higher-order QNMs becomes less significant. Finally, at long t 's, the fully-vectorial FEM results quantitatively match the QNM-expansion results both in amplitude and phase, whereas the FDTD results are phase-shifted by $\approx \pi/2$.

Although the FDTD method is clearly a reference method that is widespread for time-domain analysis, its performance deteriorates when implementing metal dispersion with auxiliary differential equations [Taf00]. The second-order accuracy of the Yee grid is no longer guaranteed at metal-dielectric interfaces even for straight interfaces and square corners, and the FDTD predictions for metallic structures suffer from numerical errors that are known to far exceed those of FEMs [Bes07]. As shown in Appendix 5 where the accuracy of the QNM-expansion and FDTD methods are studied by

increasing the mesh discretization accuracy, the convergence of the QNM-expansion data appears much more stabilized than the FDTD ones.

Indeed only the fundamental QNMs contribute to the response at long t 's and the high accuracy of the QNM formalism is to be expected. However, the high degree of accuracy together with the high level of simplicity constitute a direct evidence of the force of the present formalism, and especially Eqs. 4-2 and 4-3.

4.6 Conclusion

A semi-analytical time-domain QNM-expansion theory to calculate the temporal response of plasmonic and photonic nanoresonators has been presented. The approach relies on an analytic continuation at complex frequencies using a modal expansion of the scattered field and markedly contrasts with classical Maxwell's equation solvers, such as the FDTD method. The numerical implementation of the QNM-expansion formalism is simple. It relies on the computation and normalization of a few QNMs (Eq. 4-2), which can be performed with effective mode-solvers, followed by the calculation of a 3D integral over the physical volume of the resonator and a 1D Fourier transform straightforwardly implemented with a Fast-Fourier-Transform algorithm (Eq. 4-3). The present theory is approximate, but when the physics of the temporal response is driven by a few dominant QNMs only, as it is often the case, it becomes highly accurate. Comparison with the FDTD method have evidenced two major assets. First, by providing a direct access to the few control knobs, the QNM excitation coefficients, of the ultrafast dynamics of metallic nanoresonators, the QNM-expansion theory eases the interpretation of experiments, in sharp contrast with more widespread scattering theories that does not intrinsically rely on modal expansions. The comparison has also revealed that the QNM-expansion can be almost as accurate as the FDTD, while the required computational speeds and resources are considerably smaller.

It would be interesting from a theoretical point of view to investigate the limitations imposed by our QNM solver, namely the use of a low number of QNMs. Practically the QNM formalism, due to its simplicity and analyticity, may be helpful for inverse design [Alp16] to engineer for instance nanoscale pulse shapers. Other interesting perspectives concern the extension of the formalism towards molecular plasmonics [Csa11], i.e. hybrid systems composed of molecule ensembles that collectively interact with plasmonic resonances.

Chapter 5 - QUENCHING, PLASMONIC, AND RADIATIVE DECAYS IN NANOGAP EMITTING DEVICES

5.1 Introduction

Spontaneous emission remains at the core of the performance of many optoelectronic devices, including not only lighting components and displays, but also lasers, optical amplifiers, single photon sources and non-classical light sources in general. Metal nanogaps formed by a thin insulator layer sandwiched between two metals films have very rich physical properties and many established applications ranging from electron tunneling microscopy, nanocatalysis, Raman spectroscopy to disruptive electronics, but they are also likely to profoundly impact spontaneous emission [Aks14]. Owing to the strong localization in the gap, metal nanogaps strongly modify the electromagnetic density of modes. It follows that the spontaneous emission of dye molecules or quantum dots that are placed in the gap can be enhanced considerably. This fundamental phenomenon of light emission, known as the Purcell effect [Pur46], has been first demonstrated in optics by coupling quantum emitters with resonant dielectric microcavities [Lod15] with very high quality factors and mode volumes of the order of the wavelength cube. The use of deep-subwavelength confinements with plasmonic nanostructures has created a totally new framework with mode volumes 10,000 times smaller and broadband responses [Pel15, Sau13], and thus have opened a promising route toward new applications in optical spectroscopy [Gia11, Muh05, Tam08], spaser or low-threshold nanolasers [Ber03, Kha12], or broadband non-classical light sources [Pel15]. For instance, for a molecule placed close to a single metallic nanoparticle, such as a nanorod or preferably a triangular particle with sharp corners, spontaneous emission rate

enhancements of a few hundred are observed over a spectral linewidth of about a tenth of the emitted frequency. This is remarkable and unfeasible with dielectric structures. The down-side is that metal absorbs. High radiation efficiencies are achieved as long as the coupling with the particle resonance dominates, but as the molecule approaches the metal surfaces down to separation distances smaller than 10 nm , the emission efficiency breaks down. Photon emission is quenched. Consequently, quenching has been considered for many years as the predominant spontaneous decay channel for an emitter that is placed at a small separation distance d from a metallic object [Dre74]. In classical electrodynamics, this effect, which usually scales as $\propto (k_0 d)^{-3}$ [Bar98, For84], is due to the intense near field of the emitter that induces considerable Ohmic heating of the metal.

Since the very early stage of plasmonic-nanoantenna research, there was thus a concern that large spontaneous-emission-rate enhancements with metallic nanostructures would be inevitably accompanied by a strong quenching that would critically restrict antenna efficiencies. However, recent experiments [Aks14, Egg15, Kin09, Rin08] performed with molecules placed in nanogaps formed by pairs of particles placed side by side, such as patches [Aks14], bowties [Kin09], and nanoparticle dimmers [Egg15, Rin08] have shown that nanogaps offer enhancements even stronger than those achieved with single nanoparticles due to the capacitive coupling, and most importantly have revealed that the initial intuition is wrong. A recent experimental result obtained for nanocube-antenna [Aks14] provide a particularly striking example. In the experiment, a significantly large Purcell factor of 10^3 is measured and a good extraction efficiency of 50% is surprisingly predicted for dye molecules in an 8-nm -thin polymer-film sandwiched between a gold substrate and a small silver nanocube. Notably, the good efficiency is obtained for molecules that are placed only 4-nm away from the metal interfaces. In the end, the precise physical mechanisms that drive the emission of quantum emitters placed very close to metal surfaces in tiny gaps

are not well understood. In particular, it is unclear from the literature why good efficiencies are achieved despite the proximity to the metal, why quenching is not the dominant decay channel, what is the ultimate efficiency, and whether this limit is impacted by the gap thickness or other parameters.

To further explore how optical antennas may lead to new regimes of light-matter interactions, it is important to first understand the different channel decays at play when quantum emitters in 2D nanogaps emit light in the immediate vicinity of metal surfaces and then draw a relationship between this basic situation and more complex problems of light emission and coupling with nanogap antenna architectures.

This is exactly the approach that is adopted in the present chapter. First, after describing the emission of an emitter on a metallic interface, we provide a comprehensive analysis of the decay rates of quantum emitters placed in 2D planar nanogaps. So far, this has been discussed only with scattered numerical calculations performed for specific gap thicknesses and metal dielectric constants [For84, Jun08, Rus12]. In contrast, we derive a closed-form formula for the branching ratio between quenching and gap plasmon decays in the limit of small gap thicknesses, and then clarify the key material and geometrical parameters that drive the ratio. Counterintuitively, we evidence that the key parameters are the material permittivities, and not the gap thickness and that the gap plasmon decay surpasses the quenching decay for nanogaps fed with high-refractive-index materials and molecules polarized perpendicular to the gap interfaces.

Then we use the understanding gained from 2D planar structures to infer general recipes for designing efficient nanogap emitting devices. For that purpose, we model nanogap devices as gap-plasmon Fabry-Perot resonators and propose a phenomenological classification of nanogap antenna architectures, based on the tradeoff between quenching, absorption and free-space radiation rates, which may be monitored by controlling the gap-facet reflectance.

To set the classification against real structures, we analyze nanogap emitting devices formed by tiny nanocubes laying on metal surfaces. By scaling down the gap thickness and the cube dimensions to keep resonance in the visible, distinct behaviors within the same architecture family are comprehensively reviewed. Our analysis corrects inaccurate numerical results of the recent literature [Aks14, Ros14], and definitely sets nanogaps with engineered facets as a very promising technological platform for light-emitting devices.

5.2 Decays on a single interface

To start the analysis, let us consider the classical problem of the emission of a vertically-polarized molecule (treated as an electric dipole) buried in a polymer layer at a small distance d from a silver interface. Figure 5-1 summarizes the main trends for an emission wavelength λ at 650 nm.

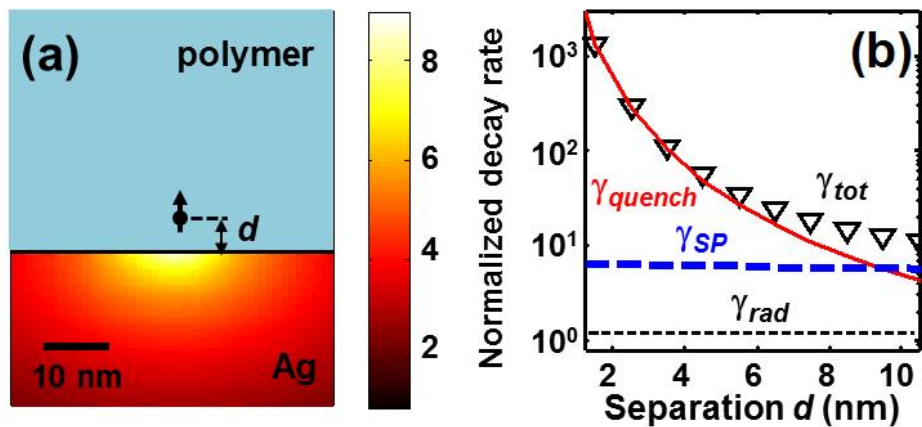


Figure 5-1. Radiation of a vertical electric dipole above a Ag/polymer interface. **a)** $\log_{10}(|E|^2)$ of the total electric field excited by the dipole (black arrow) for a dipole-metal separation distance $d = 4$ nm. **b)** Calculated decay rates into SPPs (γ_{SP} , blue), free space photons (γ_{rad} , black), and quenching (γ_{quench}^{SI} , red). The total decay rates γ_{tot} is shown with black triangles. All decay rates are normalized by the decay rate in a vacuum. The calculations are performed for an emission wavelength $\lambda_0 = 650$ nm. The refractive index of polymer is $n = 1.4$ and the silver permittivity is $\epsilon_{Ag} = -17 + 1.15i$ [Pal98].

As d decreases, the normalized decay rate γ_{SP} (we normalize all decay rates by the vacuum decay rate hereafter) into surface plasmon polaritons (SPPs) and the normalized radiative decay rate γ_{rad} remain constant and the total normalized decay rate γ_{tot} becomes dominantly driven by the direct decay γ_{quench}^{SI} in the metal, which is known to scale with the cube of d , $\gamma_{quench}^{SI} = \frac{3}{8\varepsilon_d(k_0d)^3} \text{Im} \left(\frac{\varepsilon_m - \varepsilon_d}{\varepsilon_m + \varepsilon_d} \right)$ in a local quasi-static approximation [For84], with ε_d and ε_m denoting the dielectric and metal permittivities, and $k_0 = 2\pi/\lambda$ the wavevector.

5.3 Decays in dielectric nanogaps

We obtain radically different results when two adjacent metallic interfaces are considered. Let us consider the emission of a vertically-polarized molecule buried in the middle of a polymer layer of thickness $2d$ of a metal-insulator-metal (MIM) planar stack. Two channels are available for the decay. Either the molecule excites the gap plasmon modes of the planar stack or quenches by directly heating the metal. We denote by γ_{GSP} and γ_{quench} the corresponding normalized decay rates. Figure 5-2a-b shows the radiated field and decay rates for the same emission wavelength and materials as those used for the single interface in Fig. 5-1. First we find that the direct decay in the metal, γ_{quench} scales as d^{-3} as $d \rightarrow 0$. This scaling is understood from the local and static nature of quenching. Intuitively the quenching rate in a nanogap is expected to be ~ 2 times larger than the quenching rate γ_{quench}^{SI} of the same vertical dipole on a *single interface* at the same separation distance d , and since $\gamma_{quench}^{SI} = \frac{3}{8\varepsilon_d(k_0d)^3} \text{Im} \left(\frac{\varepsilon_m - \varepsilon_d}{\varepsilon_m + \varepsilon_d} \right)$ as $d \rightarrow 0$ [For84], the cubic scaling is well anticipated. In fact, $\gamma_{quench} \approx 2\gamma_{quench}^{SI}$ holds for $d > 10 \text{ nm}$ only; as smaller d 's, we found empirically with numerical calculations performed at 650 nm that the quenching rate γ_{quench} is ~ 3 times larger than γ_{quench}^{SI} .

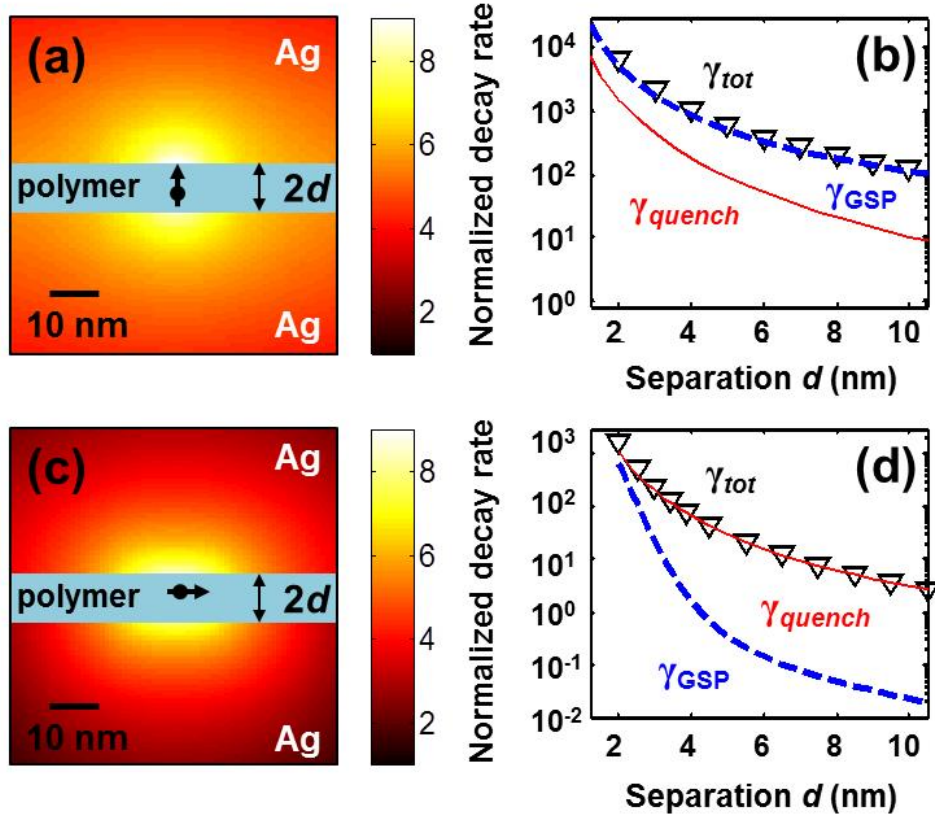


Figure 5-2. Radiation of an electric dipole placed inside an Ag/polymer/Ag nanogap. a-b) Vertical electric dipole placed at the center of the nanogap; **c-d)** horizontal electric dipole that is placed 1 nm above the nanogap center (horizontal electric dipoles placed in the gap center do not couple to the gap plasmon mode). **a-c)** $\log_{10}(|E|^2)$ of the total electric field radiated by the dipole (black arrow) for a gap thickness $2d = 8$ nm. **b-d)** same legend as in Fig. 5-1b, except for the additional dashed-blue curves that represent the decay rates into gap plasmons.

Importantly, we also find that the normalized decay rate into the gap plasmon modes of the planar stack also scales as the cube of the separation distance $2d$ between the metal films. The fact that γ_{GSP} and γ_{quench} have an identical rate-dependence with d is not trivial but should not come as a surprise; for vanishing d 's, gap plasmons exhibit slower group velocities ($v_g \propto d^{-1}$) [Yan12] and become mostly electronic waves with a low photonic character; they lose their delocalized coherent character, so that direct near-field absorption and gap-plasmon excitations contribute similarly to the local density of states seen by the quantum emitter. By using a complex continuation approach to calculate the Green-tensor [Col04] and by assuming

that the transverse electric and magnetic field components of the gap plasmon bear a flat profile within the gap, we have derived an analytical expression for γ_{GSP} for very small gap thickness, $\gamma_{GSP} \approx \frac{12\pi\epsilon_d}{(2k_0d)^3|\epsilon_m|^2}$ (details of the derivation are given in the next section), which evidences the inverse-cubic scaling.

Let us note that the results are very different when one considers molecules with a polarization parallel to the interfaces. Since the parallel electric-field component of the gap plasmon is much weaker than the perpendicular component, plasmonic modes are weakly excited for parallel polarizations, see Figs. 5-2c-d, and quenching is now the dominant decay channel, even for tiny gap thicknesses. Likewise, since optical pumping of molecules placed in nanogaps is dominantly performed via the excitation of gap plasmons, optical pumps are much less efficient for molecules oriented parallel to the interfaces than for those oriented vertically.

Thus we obtain an analytical expression for an important figure of merit of planar nanogaps with vanishing gap thicknesses, namely the branching ratio F between gap-plasmon decay rates and quenching rates

$$F \approx \frac{\gamma_{GSP}}{3\gamma_{quench}^{SI}} = \frac{2\epsilon_d}{\text{Im}(\epsilon_m(\omega))} \left| \frac{\epsilon_m(\omega) + \epsilon_d}{\epsilon_m(\omega)} \right|^2, \quad (5-1)$$

with ϵ_d and ϵ_m denoting the dielectric and metal permittivities. The formula carries important hints:

First, the ratio is independent of d for $k_0d \rightarrow 0$, the first correction term being of order $O(k_0d)^2$, and takes a universal expression that only depends on the dielectric constants.

Second, for good metals, $\epsilon_d \ll |\epsilon_m(\omega)|$, one should bury the quantum emitter in a high-index material to enhance the branching ratio in the near- and far-infrared spectral regions.

Third, the ratio solely depends on the losses encountered in polarizing the material, i.e. on $\text{Im}(\epsilon_m(\omega))$, and not on the usual quality factor $-\frac{\text{Re}(\epsilon_m(\omega))}{\text{Im}(\epsilon_m(\omega))}$ of plasmonic materials, which gives an incontestable advantage to silver at visible frequencies, in comparison with gold or aluminum for instance.

Figure 5-3 shows typical branching ratios that can be obtained in the visible and near-infrared spectral regions with different metals and gap materials. The usefulness of the simple formula in Eq. 5-1 is reinforced by its ability to provide quantitative predictions, as evidenced with the comparison with fully-vectorial computational data (shown with marks) obtained for planar nanogaps with small gap sizes ($d = 2 \text{ nm}$). We emphasize that Eq. 5-1 is obtained in the asymptotic limit $k_0 d \rightarrow 0$; as the gap thickness increases beyond the quasi-static approximation, the ratio F increases because quenching rapidly vanishes, and in this sense Eq. 5-1 actually sets a lower bound for the branching ratio. On overall, Eq. 5-1 represents a good compromise between simplicity or intuition and accuracy.

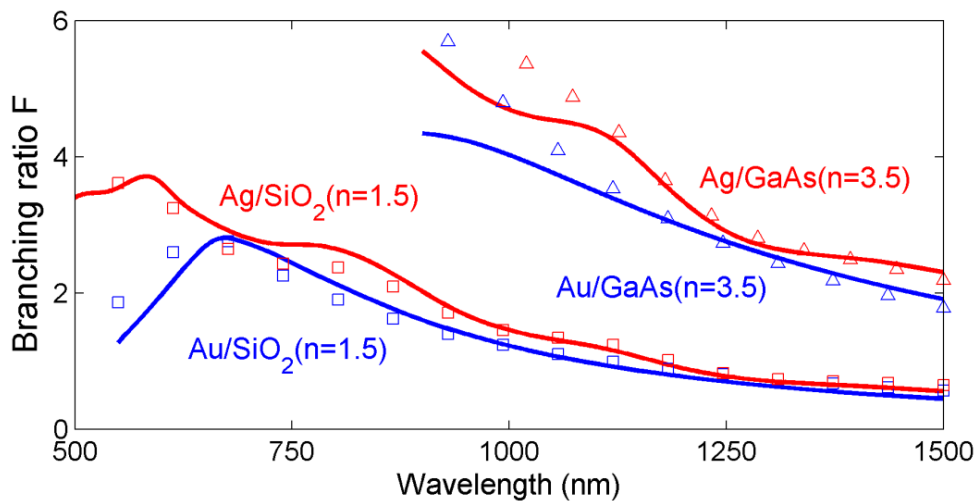


Figure 5-3. Branching ratios for nanogaps formed with various materials at visible and near-infrared frequencies. Fully-vectorial calculations (for $d = 2 \text{ nm}$) and analytical predictions from Eq. 5-1 are shown with markers and solid curves. Calculations made with Ag and Au are represented by red and blue colors, for dielectric (squares) and semiconductor (triangles) gap materials. Metal permittivities are taken from tabulated values [Pal98].

In the fully-vectorial results shown in Figs. 5-1, 5-2 and 5-3, quenching rates are found as the difference between the total decay rates (calculated as the Poynting-vector flux on a close surface surrounding the emitter) and the decay rates into the remaining channels (free-space and SPPs for Fig 5-1 and gap plasmon modes for Figs 5-2 and 5-3) calculated using an open-source software [Yan16a]. Details on the calculation technique are provided in Appendix 7 along with a verification that the indirect derivation of the quenched energy actually corresponds to the absorption in the near-field zone ($< 0.02\lambda_0^2$) of the emitter.

5.4 Analytical expression of the decay rate in gap plasmons

The objective of this section is to derive an analytical formula for the emission of a vertically polarized electric dipole source emitting in an MIM stack. The following derivation relies on a formalism that is developed in [Yan16a].

5.4.1 Power coupled to gap plasmons in MIM stacks

For an electric current J that is vertically polarized ($J = J_z$, see Fig. 5-4) and placed at $r = 0$, the excited gap plasmon field $E_{GSP}(r, \theta, z)$ can be written as

$$E_{GSP}(r, \theta, z) = c_{GSP} \hat{E}_{GSP}^+(k_{GSP}, r), \quad (5-2)$$

where c_{GSP} denotes the mode amplitude (a constant to be determined), $\hat{E}_{GSP}^+(k_{GSP}, r)$ describes the r - and z -dependent mode profile, and the superscript '+' indicates outgoing mode (propagating from $r = 0$ to $r = \infty$).

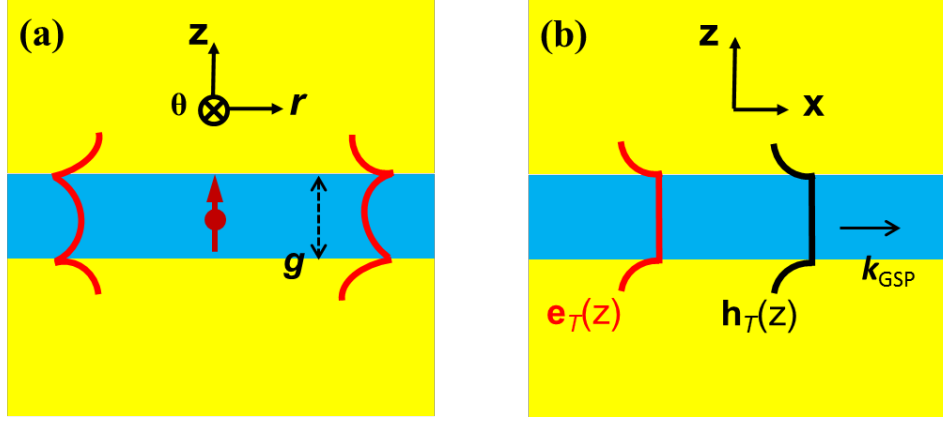


Figure 5-4. Dipole emission in an MIM stacks. **a)** We consider the emission of a vertical electric dipole placed in the dielectric nanogap at $r = 0$. **b)** In an MIM stack with a narrow gap ($g \rightarrow 0$), the transverse electric and magnetic field-components can be assumed to be independent of the transverse coordinate.

According to the unconjugated form of Lorentz reciprocity, the plasmon amplitude can be found by a dot product of J_z and the ingoing mode $\hat{E}_{GSP}^+(k_{GSP}, r)$ as [Yan16a]

$$c_{GSP} = \hat{E}_{GSP}^- \cdot J_z / N_{GSP}. \quad (5-3)$$

In Eq. 5-3, $N_{GSP} = 16/k_{GSP}$ denotes the mode normalization coefficient [Yan16a] and the minus superscript ‘-’ refers to ingoing modes (propagating from $r = \infty$ to $r = 0$). Accordingly the total power carried by the gap plasmon is found as

$$P_{GSP} = 4|c_{GSP}|^2 / |k_{GSP}|. \quad [Yan16a] \quad (5-4)$$

According to Eqs. 5-3 and 5-4, we need the z-component electric field of the mode. The z-component of the gap plasmon can be written as $\hat{E}_{GSP}^\pm(k_{GSP}, r) = H_0^\pm(k_{GSP}r)e_T(z)$ [Yan16a], with H_n^\pm denoting the Hankel function of the first (+) or second (-) kind of order n , $e_T(z)$ denoting the transverse electric field of the z-dependent mode profile (see Fig. 5-4). Note that since the dipole source is placed at $r = 0$, the Hankel functions diverge at $r = 0$. Therefore a

special trick to avoid singularity is applied [Yan16a], and Eq. 5-4 is rewritten as

$$P_{GSP}(z) = |J_z|^2 |e_T(z)|^2 |k_{GSP}|/16. \quad (5-5)$$

5.4.2 Mode profile of gap plasmon in MIM stacks with very small gap

To use Eq. 5-5 for deriving a closed-form expression, we need to calculate $e_T(z)$ and k_{GSP} . In principle, the mode profile can be calculated analytically [Yeh88]; however, as we are solely interested by vanishing gaps ($g \rightarrow 0$), the mode profile can be found in a simple manner by assuming that the transverse electric $e_T(z)$ and magnetic $h_T(z)$ field components inside the gap are uniform (Fig. 5-4b). Thus we have

$$\begin{cases} e_T(z) = e_0, h_T(z) = h_0, \text{ for } |z| \leq g/2 \\ e_T(z) = e_0 \frac{\varepsilon_d}{\varepsilon_m} \exp(-\tau|z-g/2|), h_T(z) = h_0 \exp(-\tau|z-g/2|), \text{ for } |z| > g/2 \end{cases} \quad (5-6)$$

where e_0 and h_0 denote the amplitudes of electric and magnetic components inside the gap, τ denotes the damping term of the plasmon in the metal cladding. Applying Eq. 5-6 into unconjugated form of mode normalization based on Lorentz reciprocity (a normalization method valid for lossy modes) [Sny83, Lal09] $\int e_T(z)h_T(z)dz = -2$, we find easily that

$$e_0 h_0 \left(g + \frac{\varepsilon_d}{\varepsilon_m} \frac{1}{\tau} \right) = -2. \quad (5-7)$$

If $g \rightarrow 0$, k_{GSP} can be expressed as $k_{GSP} = -\frac{2\varepsilon_d}{\varepsilon_m g}$ [Boz07], with ε_d and ε_m denoting the gap (dielectric) and metal permittivities, and τ ($\tau^2 = k_{GSP}^2 - k_0^2 \varepsilon_m$) can be found as

$$\tau = -\frac{2\varepsilon_d}{\varepsilon_m g}. \quad (5-8)$$

Applying Eq. 5-8 into Eq. 5-7, we obtain the important (and simple) relation

$$e_0 h_0 \approx -\frac{4}{g}. \quad (5-9)$$

Then by applying $h_T(z) = \frac{\omega \varepsilon_0 \varepsilon_d}{k_{GSP}} e_T(z)$ into Eq. 5-9, which is valid within the dielectric gap and can be easily found for any slab waveguide, we find

$$e_T(z) = e_0 = \sqrt{8/(\omega \varepsilon_0 \varepsilon_d g^2)} \text{ for } |z| \leq g/2. \quad (5-10)$$

5.4.3 Asymptotic expression of the decay rate in gap plasmons for very small gaps

Incorporating Eq. 5-10 into Eq. 5-5, we find

$$P_{GSP} = \frac{\varepsilon_d}{\omega g^3 \varepsilon_0 |\varepsilon_m|^2} |J_z|^2 (g \rightarrow 0). \quad (5-11)$$

The radiated power of the same dipole in vacuum being $P_0 = \frac{\omega^2 n}{12\pi \varepsilon_0 c^3} |J_z|^2$, we finally get the normalized decay rate as [Nov06]

$$\gamma_{GSP} = \frac{P_{GSP}}{P_0} = \frac{12\pi \varepsilon_d}{(k_0 g)^3 |\varepsilon_m|^2}. \quad (5-12)$$

Clearly, Eq. 5-12 indicates that decay to gap plasmon varies as d^{-3} (d denoting the dipole-metal distance). We recall that Eq. 5-12 relies on the approximation that the transverse components of the gap-plasmon mode does not vary with the transverse coordinate. This is all the more accurate as the gap thickness is small. Thus, the coupling to gap plasmons in nanogaps may overcome, by choosing the proper materials permitivities, the decay into quenching and enables the design of nanogap-based structures.

5.5 Classification of nanogap emitting devices

As a matter of fact, the decay into plasmon modes is often considered as detrimental, just like quenching. However it is of different nature since plasmons are coherent oscillations that may be transformed into free-space photons by scattering. This transformation is at the art of nanogap-device design. Intuitively, gap devices can be thought as Fabry-Perot nanoresonators with gap plasmon modes that bounce back and forth between two facets [Bol07, Miy06, Yan12]. The nanoresonator modes can couple to different decay channels, i.e. to free-space photons and surface plasmon polaritons (SPPs) for nanoresonators surrounded by metal films, with normalized rates γ_{rad} and γ_{SP} respectively. They also give rise to a new non-radiative decay, the mode absorption, with a decay rate γ_{abs} . Unlike quenching which is intrinsically determined by proximity to metal, γ_{abs} is determined by the nanoantenna design and particularly the reflectivity R of the gap facets. Thus, from the sole knowledge acquired on the 2D planar structures and according to values of R that govern the resonance strength, we may distinguish three different nanogap-device categories, as illustrated in the classification of Fig. 5-5.

Almost nil reflectivity is implemented in tapered nanogaps formed for instance by curved and flat metal surfaces (Fig. 5-5a) by adiabatically converting the slow gap-plasmons generated at the mouth [Fer10, Mub12, Yam11a] into free-space photons and SPPs launched on the flat metal surface surrounding the device. The SPPs can be further converted into photons with groove arrays for instance. Thus the total decay rate is expected to be equal to $\gamma_{tot} \approx \gamma_{GSP} + \gamma_{quench}$ where γ_{GSP} and γ_{quench} are the gap-plasmon and quenching decay rates obtained in a planar nanogap with a thickness equal to the mouth thickness. For full SPP conversion into free-space photons, the photon-radiation efficiency is thus limited by quenching and is bounded by $F/(F + 1)$, a value that can be as large as 0.75 at an emission wavelength of 600 nm for Ag/polymer gaps (see Fig. 5-3).

By contrast, for strong reflectivity favored by large impedance mismatch at the facet of tiny gaps [Aks14, Oul09], see Fig. 5-5c, the total decay rate is considerably boosted and quenching becomes completely negligible. However, the photon-radiation efficiency is limited by the absorption of gap plasmons in the tiny gap; it is expected to be much smaller than the value reached for adiabatically-tapered antennas.

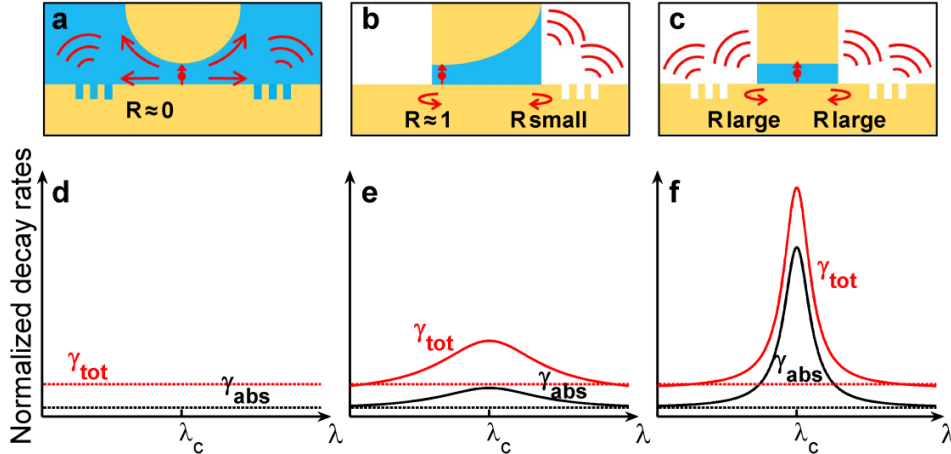


Figure 5-5. Classification of planar nanogap emitting devices with different degrees of decay rate enhancements. **a)** Tapered devices with large photon-radiation efficiencies. Dipole emission is initially captured by gap plasmons and then adiabatically (low reflection $R \sim 0$) converted into photons. Grooves etched in the metal film help conversion of launched SPPs into free-space photons. **b)** Nanoresonators with controlled facet reflectivities. **c)** Nanoresonators with strong facet reflectivities. **d-f)** Corresponding decay rates. **d)** Due to the tapering, $\gamma_{tot} \approx \gamma_{GSP} + \gamma_{quench}$ where γ_{GSP} and γ_{quench} are the gap-plasmon and quenching decay rates obtained in a planar nanogap with a thickness equal to the mouth thickness. **e)** The weak reflection in **(b)** results in a broadband rate enhancement with a large photon-radiation efficiency. **f)** The strong reflection in **(c)** results in a narrowband Fabry-Perot resonance; γ_{tot} can be considerably boosted, but the non-radiative decay γ_{abs} due to cavity absorption lowers the photon-radiation efficiency.

Figure 5-5b illustrates a promising class of nanogap antenna, with intermediate values of the facet reflectivity. Spontaneous-decay rates larger than γ_{GSP} are implemented, but the photon-radiation efficiency that is limited by quenching and absorption in the cavity may approach or even exceed the upper bound value of the $R \approx 0$ case.

5.6 Study of the nanocube antenna

After this qualitative discussion, it is interesting to set the classification of Fig. 5-5 against real nanogap emitting-device technologies. For that purpose, we consider devices formed by a tiny dielectric layer sandwiched between a metallic nanocube and a metallic substrate. This geometry that has been recently studied [Aks14, Ros14] is particularly suitable for exploring the three categories of the classification, since by scaling down the cube dimension, a whole family of gap emitting devices with distinct facet reflectivities can be straightforwardly designed and studied at the same resonant visible wavelength. But first let us begin by explaining how we calculate the photon-radiation efficiency and estimate the respective impact of quenching and gap-plasmon absorption. This is necessary because our results differ from those reported in [Aks14, Ros14], at least by a factor two for the efficiency, and it is important to understand the reason.

We consider the same nanocube geometry as in [Aks14], with a vertically-polarized emitting dipole. The latter is placed in the middle of an 8-*nm*-thick polymer gap at a cube corner, where maximum coupling with the resonance mode is achieved. Using COMSOL multiphysics, we first calculate the normalized total decay rate γ_{tot} by integrating the total power radiated around the source. Consistently with [Aks14], at resonance γ_{tot} (black circles) is as large as 10^4 , a value which represents a tenfold enhancement, compared to the normalized gap-plasmon decay rate γ_{GSP} (cyan circles) obtained for a planar nanogap with the same materials and gap thickness.

To provide a deeper insight, we also calculate the normalized decay rate γ_{mode} (i.e. the Purcell factor) into the fundamental magnetic-dipolar nanocube mode [Ros14]. γ_{mode} is calculated by using a resonance-mode theory recently developed [Bai13, Sau13] to the analysis of plasmonic nanoresonators. Owing to the very small mode volume $V = (84,000 + 8,000i) \text{ nm}^3$ of the magnetic-dipolar mode, we find that 95% of the total

decay is actually funneled into the resonance mode at resonance. The quenching rate γ_{quench} (red circles) is then calculated as $\gamma_{quench} = \gamma_{quench} - \gamma_{mode} - \gamma_{quad}$, where γ_{quad} represents a residual decay into a quadrupolar mode that resonates in the green [Las13]. Unlike intuitive statements in [Aks14], our calculations indicate that quenching (red circles) is playing a negligible role, as its rate only represents $\sim 2\%$ of γ_{tot} at resonance. Then, using an open source code that computes the radiation diagrams of free-space and guided waves [Yan16a], we calculate the normalized decays into free space photons and SPPs launched around the nanocube, γ_{rad} and γ_{SP} , respectively. We find that $\sim 60\%$ of the mode energy is dissipated into heat, and the remaining 40% equally decays into free-space photons (20%) and SPPs (20%) that are launched on the flat metal interface surrounding the cube. This suggests the great potential of nanocubes for implementing plasmon sources. The present prediction $\gamma_{rad}/\gamma_{tot} \approx 20\%$ differs from the 50% photon-radiation efficiency calculated in [Aks14, Ros14] for the same geometrical parameters. We believe that the discrepancy is due to the fact that in [Aks14, Ros14], the photon-radiation efficiency is inferred from a direct computation of the Poynting-vector flux on a close surface surrounding the nanocube, without separating the respective contributions of the radiated photons and surface plasmons with a near-to-far-field transform.

Clearly, the nanocube antenna with a facet reflectivity of ~ 0.85 , a value deduced from results reported in [Yan12], belongs to the category of nanogap antennas with large facet reflectivities, i.e. case (c) in the classification of Fig. 5-5.

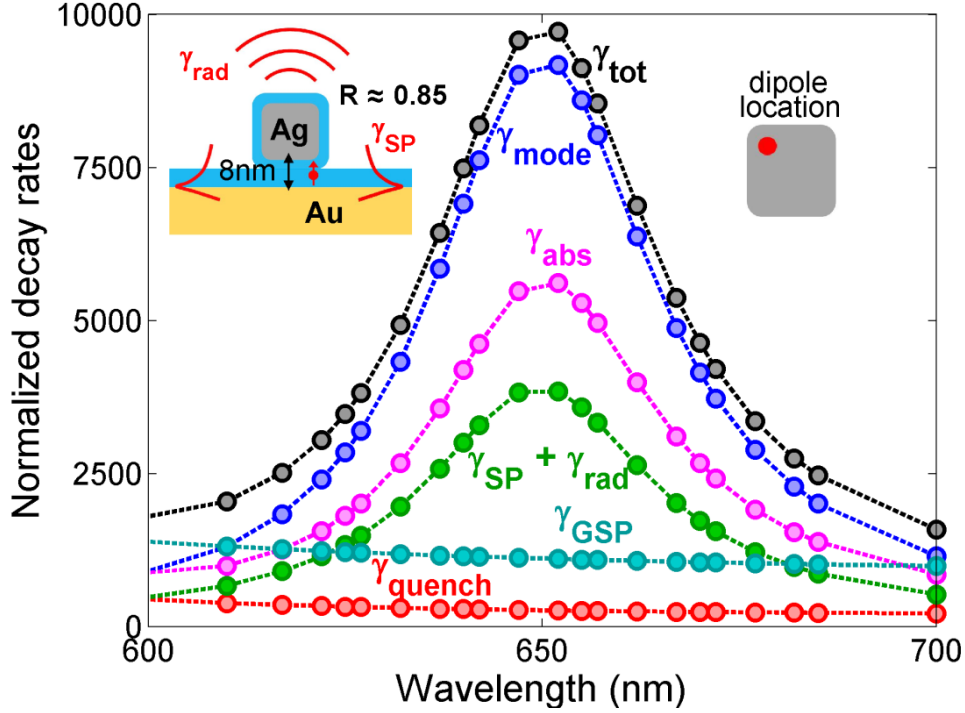


Figure 5-6. The decay channels of nanocube antennas. Calculated normalized decay rates of a vertical electric dipole at the corner (insets) of the antenna as a function of the wavelength. γ_{tot} , γ_{mode} (decay into the fundamental magnetic mode), γ_{abs} (antenna absorption), $\gamma_{rad} + \gamma_{SP}$ (sum of the radiative and SPP decay rates) and γ_{tot} are shown by black, blue, magenta, green, and red circles, respectively. γ_{GSP} (cyan) represents the decay into the gap plasmon of a planar nanogap of the same materials and gap thickness. Left inset: cross-sectional view of the nanoantenna: a silver nanocube (side length 65 nm) with a 3-nm polymer coating ($n = 1.4$) is placed on a gold substrate covered by a 5-nm polymer (8-nm gap). The molecule is represented as a red arrow placed in the middle of gap. Right inset: top view of the cube showing the position of the dipole. The frequency-dependent permittivities, ϵ_{Ag} and ϵ_{Au} , of silver and gold are taken from tabulated data [Pal98], $\epsilon_{Ag} = -17 + 1.15i$ and $\epsilon_{Au} = -9.7 + 1.04i$ @ $\lambda = 650$ nm.

We are now ready to study the nanocube performance for various thicknesses. For that, at every thickness, we adapt the cube size to maintain the magnetic-dipolar resonance at $\lambda_0 = 650$ nm and repeat the previous modal analysis. The results for total decay rate γ_{tot} and the external efficiency $(\gamma_{rad} + \gamma_{SP})/\gamma_{tot}$ defined as the normalized decay into SPPs and photons are displayed in Fig. 5-7a as a function of the gap thickness. The latter is shown to importantly impact the nanocube performance. As the thickness reduces, the facet reflectivity increases [Yan12] and accordingly,

γ_{tot} strongly increases. However, the coupling to outgoing channels also decreases and the enhancement of the total decay rates is accompanied by a sudden drop of the external efficiency, from 80% for $d = 20 \text{ nm}$ to 15% for $d = 4 \text{ nm}$.

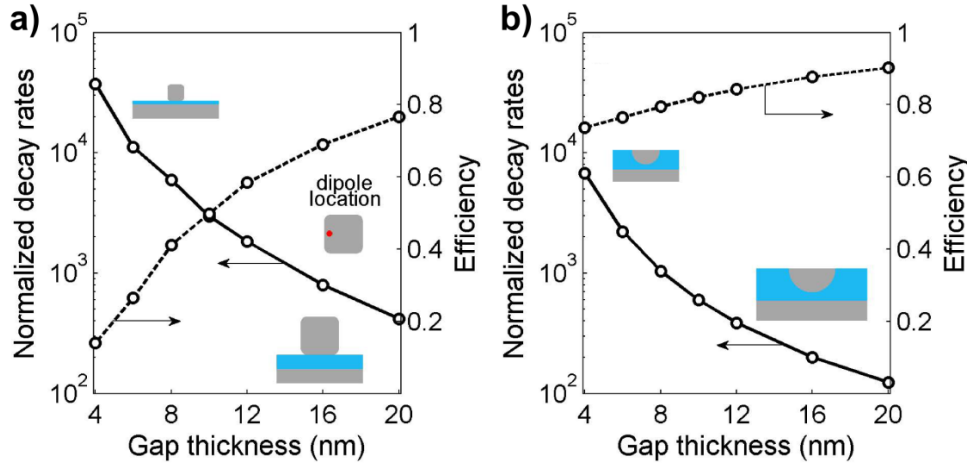


Figure 5-7. Patch versus tapered-nanogap antennas with polymer gaps. a) Patch antennas. The calculations are performed for a vertical electric dipole located close to the center of the antenna facet (inset). The cube size varies with the gap thickness to maintain the resonance wavelength at 650 nm (side lengths are $47, 56, 65, 70, 75, 80$ and 85 nm , for gap thickness $d = 4, 6, 8, 10, 12, 16$ and 20 nm). **b)** Perfectly tapered-nanogap antennas. The performances are predicted with planar-nanogap calculations by assuming perfect tapering of the gap-plasmons into SPPs and/or radiative photons. In **(a)** and **(b)**, the normalized total decay rates γ_{tot} are shown with solid curves and the external efficiencies $(\gamma_{rad} + \gamma_{SP})/\gamma_{tot}$ with dashed curves.

For the sake of comparison, in Fig. 5-7b, we display γ_{tot} and the external efficiency $(\gamma_{rad} + \gamma_{SP})/\gamma_{tot}$ (again, γ_{SP} denotes the decay to the SPPs on the flat metal surface, not gap plasmons) for a perfectly-tapered antenna (case (a) of the classification in Fig. 5-5). The predictions are obtained from planar nanogap calculations only, by assuming that $(\gamma_{rad} + \gamma_{SP})$ is equal to the gap-plasmon decay rate γ_{GSP} in a planar nanogap with a thickness equal to the mouth thickness. This amounts to assume that gap plasmons are fully converted by the tapering structure into SPPs and/or photons and this provides an upper bound for the photon-radiation efficiency. As shown by a comparison between Figs. 5-7a and 5-7b, smaller decay rates are achieved

with the tapered antenna, but significantly larger external efficiencies are also obtained. Impressively, we predict that large efficiencies $> 70\%$ with large normalized emission rates $\sim 10^3$ are achieved for tiny nanogaps. Lastly, our simulations do not include additional loss mechanisms such as electron surface collisions [Egg15] but we use silver permittivity tabulated in [Pal98] that exhibits a larger amount of non-radiative losses compare to other data sets. Regardless, even if doubts remain on the exact amount of losses in metal films/particles, our calculations open important perspectives for spontaneous light emission in general, and definitely set nanogaps as a relevant technological platform. The future success of the platform will depend on fabrication and material issues, and on our ability to engineer facet reflectivities adequately.

5.7 Conclusion

Emitting photonic devices with quantum emitters embedded in nanogaps for operation at visible and near-infrared frequencies can provide large spontaneous emission rate enhancements and good photon-radiation efficiencies, because the decay into slow gap-plasmons is considerably boosted, and quenching is thus effectively overcome. This is particularly true for gaps with high-refractive-index insulators sandwiched between good metals, since the branching ratio $\propto \epsilon_d / \text{Im}(\epsilon_m(\omega))$ between gap-plasmon decay rates and quenching rates reach values as large as 80% for semiconductor gaps operated at near-infrared frequencies. The dominant character of plasmonic decays for small gaps has a direct impact on the design and performance of nanogap emitting devices. First, the high decay rates found in planar nanogaps can be harnessed to realize tapered antennas (Fig. 5-3a) offering strong decay rate enhancements ($\approx 10^2$ - 10^3) and large photon-radiation efficiencies limited by the branching ratio between gap-plasmon decay rates and quenching rates, see Eq. 5-1. Second, even larger rate enhancements can be even achieved in nanogap cavities (Fig. 5-3c),

which exhibit strong resonances owing to strong reflection of gap plasmons at the cavity facets. In return, the photon-radiation efficiency is significantly reduced by the cavity absorption, as indicated by the analysis of the state-of-the-art nanocube devices. Third, a better balance between decay rate enhancement and photon-radiation efficiency may be reached with nanogap antennas with engineered facet reflectivities (Fig. 5-3b) for which a delicate engineering of the facets and a precise choice of the gap and metal materials may lead to acceleration decay rates greater than 10^3 with significant photon-radiation efficiency, $\approx 50\%$.

Certainly, the main strength of nanogap light emitting devices is the capability to boost the spontaneous emission rate over a broad bandwidth with potentially easy electrical contacting. This might be useful for increasing quantum yield. However, the present analysis seems to indicate that it will be hard to achieve extremely high efficiencies (≈ 1), as required for some quantum-information protocols, and that the branching of Eq. 5-1 appears as a barrier for the photon-radiation efficiency which will be hard to overcome.

CONCLUSION AND PERSPECTIVES

Photonic nanostructures provide an extremely rich physics, and their interactions with light give rise to fascinating phenomena. In this thesis, we have tried to study and understand different aspects of the interaction, examining the intrinsic responses of nanostructures but also the effects on the response of small variations in their geometries, the impact of their dimensions, or simply trying to engineer their properties.

In Chapter 1, we have studied the impact on slowness of the finite length of “periodic” waveguides. We have notably shown that physical phenomena occurring in infinite periodic systems, such as the LDOS divergence, can be mimicked on very short length scales by tricking the waves at the termination of the structure. This founding, based on general 1D-wave-physics arguments and 3D simulations on photonic crystal waveguides, has enabled the design of a new kind of resonators for which the resonance is due to sudden slow down and acceleration of light, quite differently from usual microcavities for which recirculation of reflected waves between mirrors and phase-matching are required.

Just like all slow light devices, the proposed photonic speed bump may suffer from fabrication disorder. However, the length of the structure, comparable to the spatial extent of localized modes measured and computed in Chapter 2, may reduce the sensitivity to localization with respect to long photonic crystal waveguides. Further study on the impact of disorder are interesting, both for fundamental understanding and application perspectives.

Moreover, the frequency response of the photonic speed-bump is a step-like transition that strongly contrasts with the Lorentzian responses of cavities.

This feature, achieved in a compact system, may have interests for the realization of optical switch. For instance, one could envision to exploit material properties such as electro-optical [Sor87] or thermo-optic [Yam11b] effects to dynamically shift the transmission drop as sketched in Fig. C-1.

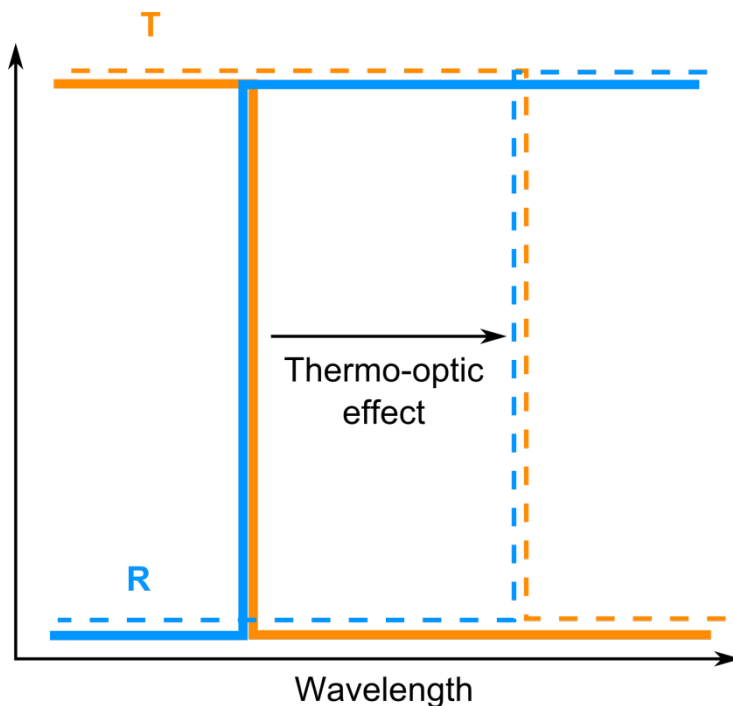


Figure C-1. Schematic of the frequency shift of the photonic speed bump for dynamic optical switches. Solid lines represent the initial behavior of the photonic speed bump. Dashed lines show the potential frequency shift in transmission and reflection after thermo-optic or electro-optical effects.

In Chapter 2, we evidenced that wavelength-scale localized modes naturally form up in photonic crystal waveguides in presence of tiny intrinsic fabrication imperfections due to the extreme flatness of photonic-crystal waveguide mode. These results, supported by both experimental and numerical data, may promote further investigations on the precise role of the effective mass on the mode sensitivity to disorder, either to achieve even smaller localized modes or to lower disorder-induced losses in slow light periodic structures, to improve the design of future photonic structures.

In Chapter 3, we have designed an original photonic crystal waveguide in which light-matter interaction is significantly increased in the surrounding

vacuum cladding. Notably, we have shown that the engineering of the modal properties could enable slow hollow-core modes with a significant fraction of the field in air to achieve strong guide-atom couplings as large as 95% for a 560-nm ($\sim \lambda/3$) separation distance from any structure material at a frequency corresponding to $n_g = 50$. However, the weak-permittivity modulation inherent to the design imposes a small slow-light bandwidth. Accordingly, a realistic implementation of atom-photon interaction schemes exploiting slow light effects with the present hollow-core waveguide seems hardly realizable.

A first idea to circumvent this issue consists in releasing the constraints on the design by finding a compromise between field extension in air and bandwidth, respectively related to the effective mode index and flatness of the mode. Another solution may reside in a more efficient control of the dispersion of the reflection-coefficient phase of the photonic-crystal mirror to tailor the penetration length [Sau09, Fra06] and evaluate its impact on the mode dispersion. With this in mind, one could replace the photonic crystal mirrors by Bragg-stack mirrors (Fig. C-2(a)). Indeed, in addition to an easier numerical implementation, the reduced degrees of freedom in the design of Bragg-stacks may facilitate the study of the penetration length.

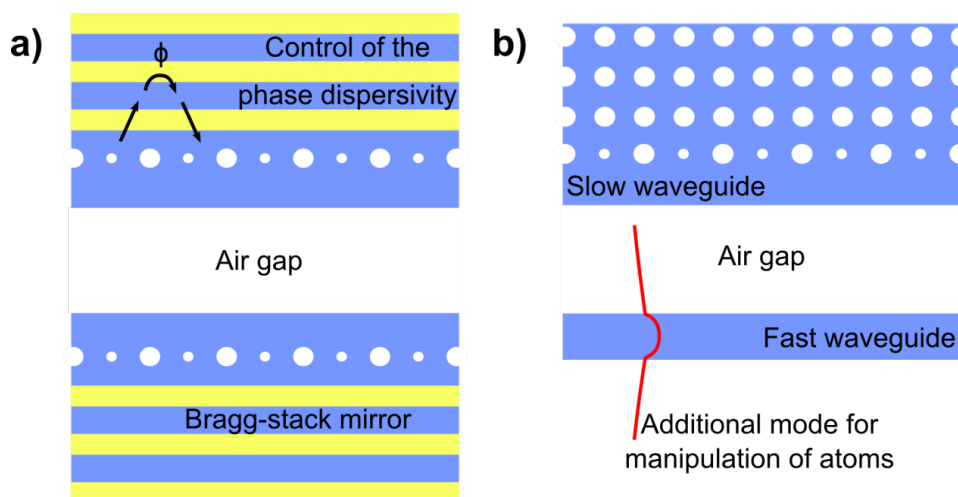


Figure C-2. Sketch of potential future designs for strong light-matter interaction in vacuum.

Alternatively, the wide-slot PhC waveguide may be modified to implement more complex trapping schemes. A first approach would be to increase the waveguide length, thus decreasing the mode frequency, and take advantage of the "conduction" mode present at higher frequencies. Moreover, the weak interaction between the two sides of the waveguide suggests that only half of the structure may be sufficient to sustain a slow mode, as demonstrated in [Zan16], providing that small geometrical parameter changes are realized to preserve the mode operation frequency. Thus, one could replace the other half of the structure by a fast waveguide (a simple dielectric ridge or a fiber for instance, see Fig. C-2(b)). Ultimately, those alternative approach may provide new paths for implementing stable trapping potentials with detuned frequencies [Gob14, Vet10].

In Chapter 4, we have first introduced a new formalism based on a QNM expansion to describe the temporal dynamics of plasmonic nanoresonators. Interestingly, the formalism, which relies on the natural resonances of the systems, provides an intuitive understanding of the underlying physical phenomena at the origin of the responses, in contrast with other scattering theories, and constitutes a powerful tool to help modeling and interpreting experiments. In addition, the analyticity of the formalism allows a quick and accurate computation of the response of any resonator for any driving pulse, much faster than that of widespread numerical methods such as the FDTD.

As briefly discussed in the Chapter, even better accuracy could be achieved by considering more QNMs in the expansion such as higher order modes and radiation (or PML) QNM's (i.e. not bounded to the resonator but delocalized in the PML). Following this goal, preliminary theoretical derivations and numerical tests for the calculations of many QNM modes based on auxiliary-field method [Ram10] have been carried out. Figure C-3 shows the calculation of 100 QNMs of the Dolmen geometry. First, the new QNM solver retrieves the three dominant modes (insets A, B and C) previously computed with the iterative pole-search solver [Bai13]. The agreement is excellent since the relative difference between the frequencies

calculated with the new QNM solver and the iterative pole search are smaller than 10^{-14} when the same mesh is used for both computations. The solver also gives access to higher order modes (insets D and E) and PML modes (inset F). Details on their respective contribution in the resonator response is still under study and will be discussed during the defense.

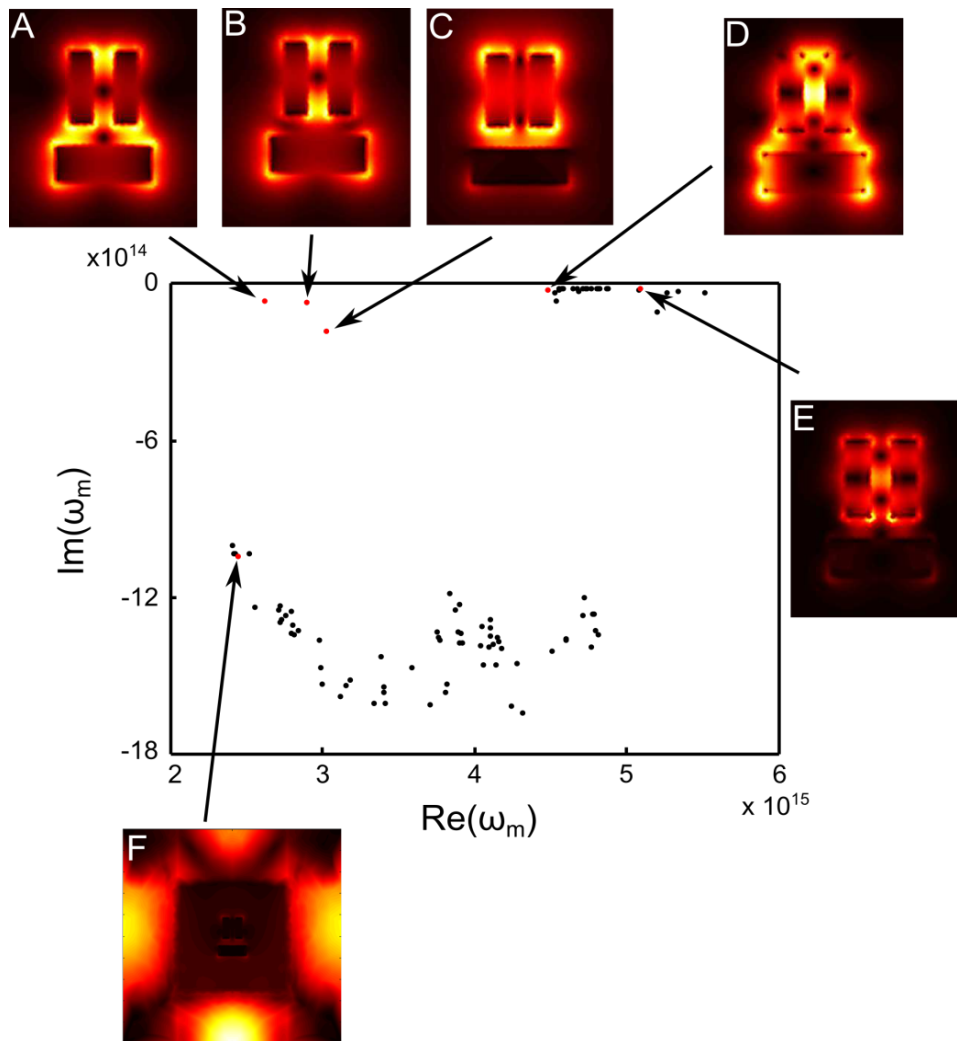


Figure C-3. Dolmen QNM eigenfrequencies computed with the auxiliary-field method. Insets: Absolute value of the electric field in a cross-section. Insets A, B and C: Dominant QNMs used in Chapter 4. Insets D and E: Higher-order QNMs. Inset F: PML QNMs (plotted in the full numerical space).

Another perspective would be the development of a coupled mode theory with QNMs. The latter would enable the description of complex geometries from simpler building blocks, i.e. the QNMs of individual resonators, and may provide more degrees of freedom for the design of new plasmonic

devices. Applied to the temporal regime, the coupled mode theory may allow us to assess, for instance, time-dependent energy transfers between resonators.

In the last Chapter, we studied the different decay processes involved in the emission of quantum emitters embedded in nanogap plasmonic antennas and evidenced that high radiation efficiency could be reached despite the small proximity between the emitter and the metal. Indeed, the intrinsic non-radiative decay, i.e. quenching, may be overcome thanks to deep-subwavelength confinement and the coupling to slow plasmons offered by nanogap structures. This important finding suggests that one should not be afraid of tiny gaps to implement emitting optical devices, and that nanogap antennas may really offer new opportunities not met with dielectric cavities.

There is still a long way to go before optimizing the performance of nanogap plasmonic antennas, starting from designing nanogap geometries to match the impedance of slow gap plasmons with free-space photons and to make the extraction efficiency approaching 100%. This approach is already under study [Yan16b] and shows promising results. Ultimately, quenching will always limit the efficiency but derivations of the different decay rates provided in the chapter may provide inspiration to wisely select quantum emitters, dielectric insulators and plasmonic materials [Nai13] to maximize both radiative decay rate and radiative efficiency in a specific wavelength range.

APPENDIX 1: COMPUTATIONAL METHOD

In this Appendix, we describe the numerical method used in Chapter 1, 2 & 3, which was initially developed at Institut d'Optique in the group of P. Lalanne in the 00's. The method is an extension of the rigorous coupled-wave analysis (RCWA) also called the Fourier Modal Method (FMM) to analyze aperiodic systems.

The RCWA or FMM has been gradually developed over years for analyzing the diffraction by gratings, starting in the 80's [Moh81, Moh95]. As the name Fourier modal method suggests, the electromagnetic field components and material functions are expanded into Fourier series in terms of spatial harmonics. However, the spatial discretization and finite truncation of Fourier series that are required for the numerical implementation result in the deviation from the exact values. For a long time, the numerical performances of Fourier expansion techniques have been plagued by slow convergences, which have been thought to be due to Gibbs phenomenon occurring from the Fourier expansion of discontinuous functions [Li93, Vil94]. A few years after, a spectacular improvement in the convergence rate has been achieved for TM polarization of one-dimensional gratings [Gra96, Lal96], as well as for the general case of conical diffraction [Lal96]. This finding was followed by the derivation of mathematical theorems that govern the factorization of Fourier series, i.e. Fourier factorization rules [Li96a]. It implies that an appropriate formulation of the eigenvalue problem and the correct Fourier factorization must be carefully performed to assure fast convergence rate. These works had a tremendous impact on the

performances of theories relying on Fourier expansion techniques for solving Maxwell's equations.

A1.1 a-FMM: implementation of Perfectly Matched Layer

The a-FMM (where “a” denotes “artificially periodic, or aperiodic for short”) is a generalization of the FMM approach that allows to handle non-periodic geometries, using an artificial periodization and the introduction of absorbers [Lal00], Perfectly Matched Layers (PMLs) [Sil01] or of complex nonlinear coordinate transformations [Hug05b] to satisfy the outgoing wave conditions on finite periodic spaces. Basically, the PMLs map the two semi-infinite half spaces surrounding the investigated geometry into a finite space. Theoretically, this mapping guarantees that the outgoing wave conditions are perfectly satisfied since evanescent or propagative fields, incoming from the boundaries of the computational domain, are attenuated over an infinite distance before reaching the geometry. The mapping can be implemented either as a modification of the differential operators, or as a renormalization of the permittivity and permeability distributions [Hug05b] and appears as a generalization of more classical PML-formulations [Che94, Sac95].

The artificial periodization along the transverse directions makes the field periodic, which allows to expand the electric field \mathbf{E} and magnetic field \mathbf{H} into a Fourier basis [Sil01],

$$\mathbf{H}(r) = \sum_{p,q} (U_{xpq}\mathbf{x} + U_{ypq}\mathbf{y} + U_{zpq}\mathbf{z}) \exp(i(pG_x x + qG_y y)), \quad (\text{A1-1})$$

$$\mathbf{E}(r) = \sum_{p,q} (S_{xpq}\mathbf{x} + S_{ypq}\mathbf{y} + S_{zpq}\mathbf{z}) \exp(i(pG_x x + qG_y y)), \quad (\text{A1-2})$$

where $G_x = 2\pi/\Lambda_x$ and $G_y = 2\pi/\Lambda_y$, Λ_x and Λ_y being the lengths of the artificial unit cell. In Eqs. (A1-1) and (A1-2), S and U are unknown z -dependent coefficients. In practice, the Fourier series have to be truncated, so

we denote by m_x and m_y the truncation ranks, $-m_x < p < m_x$ and $-m_y < q < m_y$. By incorporating Eqs. (A1-1) and (A1-2) into the curl Maxwell's equations, and by expanding the permittivity and the permeability in the Fourier basis as well, we obtain after elimination of the z-components

$$\frac{1}{k_0} \frac{d[\Psi]}{dz} = \mathbf{\Omega}(z)[\Psi]. \quad (\text{A1-3})$$

In Eq. (A1-3), Ψ is equal to $[S_x S_y U_x U_y]$, a column-vector formed by the electric- and magnetic-field coefficients and $\mathbf{\Omega}$ is a matrix formed by the z-dependent Fourier coefficients of the permittivity and of the permeability.

A1.2 Scattering matrix

For periodic waveguides, the computation of the Bloch modes requires the integration of Eq. (A1-3) over one period a along the z-direction from z to $z + a$. For the integration, we approximate the real profile of the circular holes by a stack of slices with locally z-invariant permittivities [Lal02]. Within this approximation, the integration along the z-direction can be performed analytically. The modes of each slice (p) correspond to the modes of a z-invariant waveguide surrounded by PMLs [Sil01]. The modes, denoted by the vectors $\mathbf{W}_n^{(p)}$ and $\mathbf{W}_{-n}^{(p)}$ ($n = 1, \dots, N$) in the Fourier basis, are computed in every slice (p) as the eigenvectors of a reduced matrix $\mathbf{\Omega}^{(p)}$. Denoting by $\lambda_n^{(p)}$ the corresponding eigenvalue, the electromagnetic field $\Psi^{(p)}$ in every slice (p) can be written as a superposition of modes

$$\Psi^{(p)} = \sum_1^N b_n^{(p)} \exp(-\lambda_n^{(p)} z) \mathbf{W}_{-n}^{(p)} + f_n^{(p)} \exp(\lambda_n^{(p)} z) \mathbf{W}_n^{(p)}, \quad (\text{A1-4})$$

where $\mathbf{b}^{(p)}$ and $\mathbf{f}^{(p)}$ are column vectors whose elements are the amplitudes of the modes propagating backward (in the negative z-direction) and forward (in the positive z-direction) respectively. The linearity of Maxwell's equations assures the existence of a linear relationship between the mode amplitudes of

the slice (1), $\mathbf{b}^{(1)}$ and $\mathbf{f}^{(1)}$, in the input z -plane and those of the slice (N), $\mathbf{b}^{(N)}$ and $\mathbf{f}^{(N)}$, in the output $(z + a)$ -plane. An S-matrix approach is used to relate these amplitudes and we have

$$\begin{bmatrix} \mathbf{b}^{(1)} \\ \mathbf{f}^{(1)} \end{bmatrix} = \begin{bmatrix} S_{11} & S_{12} \\ S_{21} & S_{22} \end{bmatrix} \begin{bmatrix} \mathbf{b}^{(N)} \\ \mathbf{f}^{(N)} \end{bmatrix}, \quad (\text{A1-5})$$

where the matrix on the right-hand side of the equation is simply the S-matrix of a unit cell. Details concerning the recursive calculation of S can be found in [Li96b]. The Bloch modes are computed from eq. (A1-5) using a generalized and stable eigenproblem [Cao02].

APPENDIX 2: FABRY-PEROT MODEL FOR THE DESCRIPTION OF THE PHOTONIC SPEED BUMP

To understand and explain the behavior of the photonic speed bump discussed in Chapter 1, we have developed a single-mode model by assuming that the structure can be described by the bouncing back and forth of the slow-W1 Bloch mode between the left and right tapers. This assumption can be justified by the fact that this mode is the dominant mode that transfers energy in the structure at frequencies close to the band edge.

The model, which solely relies on parameters related to the Bloch mode itself and its reflection coefficient on the taper, gives two analytical expressions of the Purcell factor of a source in the center of the structure according to the frequency range of emission.

The starting point of the model is the coupling coefficient

$$A_S = -E(r_0) \cdot J/4 \quad (\text{A2-1})$$

of the source with the dominant Bloch mode [Lec07a]. In Eq. A2-1, $E(r_0)$ is the amplitude of the normalized Bloch mode field on the source and J the amplitude of the considered current source. In the conduction band, A_S is proportional to $(c/v_g)^{-1/2}$. In the band gap, the source does not radiate but excite an evanescent Bloch mode that does not carry energy. How the Bloch mode should be correctly normalized so that Eq. A2-1 holds for both evanescent and propagative Bloch modes is explained in [Lec07a].

In a second step, the finite size is taken into account by considering the Bloch mode reflection coefficient r of the tapers. With a one-mode model, we

obtain $A_S/(1 - ru^2)$, for the coupling coefficient with $u = \exp(ik_0 n_{eff} Na)$ the phase and the damping accumulated on the inner section of the speed bump that is composed of N periodic cells. The Purcell factor P is straightforwardly inferred. For a frequency in the band, we have

$$P = 2 \left| \frac{A_S}{1 - ru^2} \right|^2 (1 - |ru^2|^2). \quad (\text{A2-2})$$

Equation A2-2 is identical to that obtained for Fabry-Perot cavities formed by the bouncing back and forth of a slow mode between two mirrors [Sau05]. In the gap, the phenomena is radically different as it results from the tunneling of two counter-propagating evanescent Bloch modes. Each mode does not carry energy but actually their superposition provides a net power flow and we have

$$P = 2 \left| \frac{A_S}{1 - ru^2} \right|^2 \text{Im}(ru^2), \quad (\text{A2-3})$$

We note that for $r = 0$ (perfect tapers), the two expressions recover the trivial expressions $P_{band} = 2|A_S|^2$ and $P_{gap} = 0$, where the factor two arises from the coupling to two channels.

Figure A2-1 compares the Purcell factor of an electric source placed in the center of a speed bump calculated with fully-vectorial technique based on a Green tensor formalism [Lec07b] and the Purcell factor predicted by the Fabry-Perot model. We notice that for long enough speed bumps (≥ 8 periods), the model predictions are almost perfectly superimposed with the Green-tensor computations. As expected, the model well predicts the LDOS inhibition in the gap, the LDOS enhancement at the band edge and the oscillations due to backreflection for long speed bumps. Moreover, it implies that the propagative Bloch mode solely contributes to the energy transfer in the structure. For short speed bumps in a), the model largely overestimate the Purcell factor in the structure. This suggests that other modes, not taken into account in the model, are involved in the energy transfer. As mentioned

in Chapter 1, we attribute the modification of the Purcell factor to evanescent modes supported by PhC waveguides.

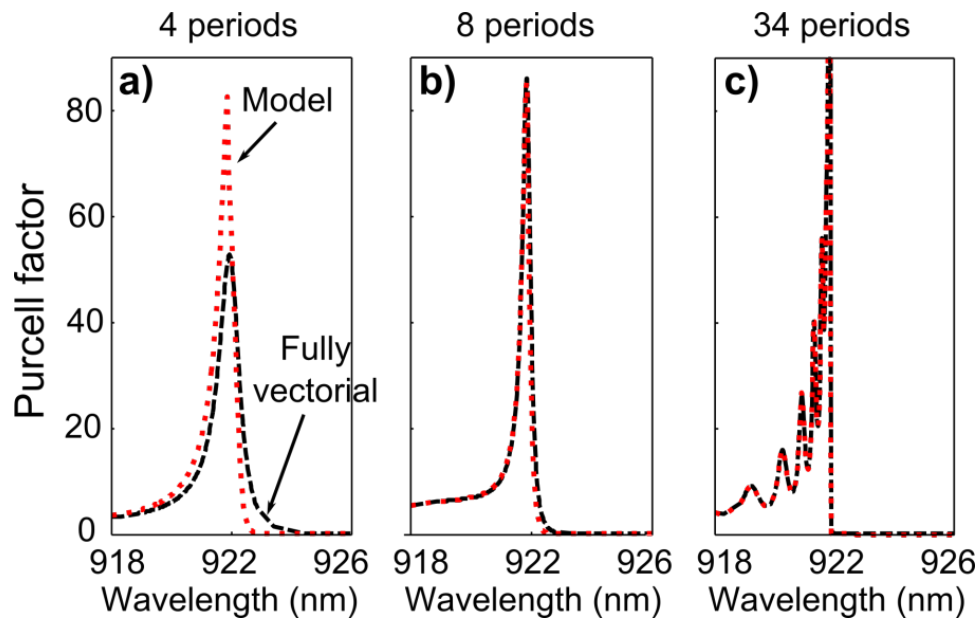


Figure A2-1. Fabry-Perot model for the speed-bump. Purcell factor calculations of a electric source placed in the center of 4- **(a)**, 8- **(b)** and 34- **(c)** period long speed bumps for tapers designed for $n_g = 500$. The dashed black curves represent data obtained with the fully-vectorial computations and the dotted- red curves represent the Purcell factor predicted by the Fabry-Perot model.

APPENDIX 3: PROTOCOL FOR THE CALCULATION OF INDIVIDUAL LOCALIZED MODES

In this Appendix, we detail the strict procedure that we used in Chapter 2 to determine the distribution function of the spatial extent of localized modes. The protocol thoroughly eliminates necklace or delocalized states, to solely count states that are truly-confined in a limited space.

All our computational results were obtained with an in-house fully-vectorial frequency-domain Fourier-Bloch-mode method [Sil01, Lec07a]. The statistical retrieval of $P_\sigma(L_0)$ requires determining whether the resonant modes identified in the LDOS spectrum are truly individual localized modes. On the one hand, the field profile of localized modes (with spatial extent smaller than the computational system size) should remain unchanged after increasing the waveguide length. On the other hand, a normalized field profile independent of the position of the source indicates that a single mode contributes to it. On this basis, we computed the on-axis magnetic-field profiles generated by a dipole source at the center of the system at the resonance wavelength for the $100a$ -long perturbed waveguide, for a $200a$ -long protracted waveguide obtained by surrounding the $100a$ -long waveguide by two $50a$ -long perturbed sections, and for the same $200a$ -long waveguide where the source position was shifted by two periods. A resonant mode was considered as an individual localized mode only if the field profile remained unchanged after the waveguide extension and source displacement. The spatial extent of the localized mode is defined as $L = |z_1 - z_2|$, where the magnetic field intensity $|H(z)|^2$ should be smaller than $(|H(z)|^2)/e^2$ everywhere outside the interval $[z_1; z_2]$. Figure A3-1 shows several examples of resonant modes corresponding or not to individual

localized modes. Note that individual localized modes are retrieved independently of the physical mechanism underlying their formation (Anderson localization or gap confinement) [Bli08] and all delocalized modes, including necklace states [Ber05, Seb06], are excluded.

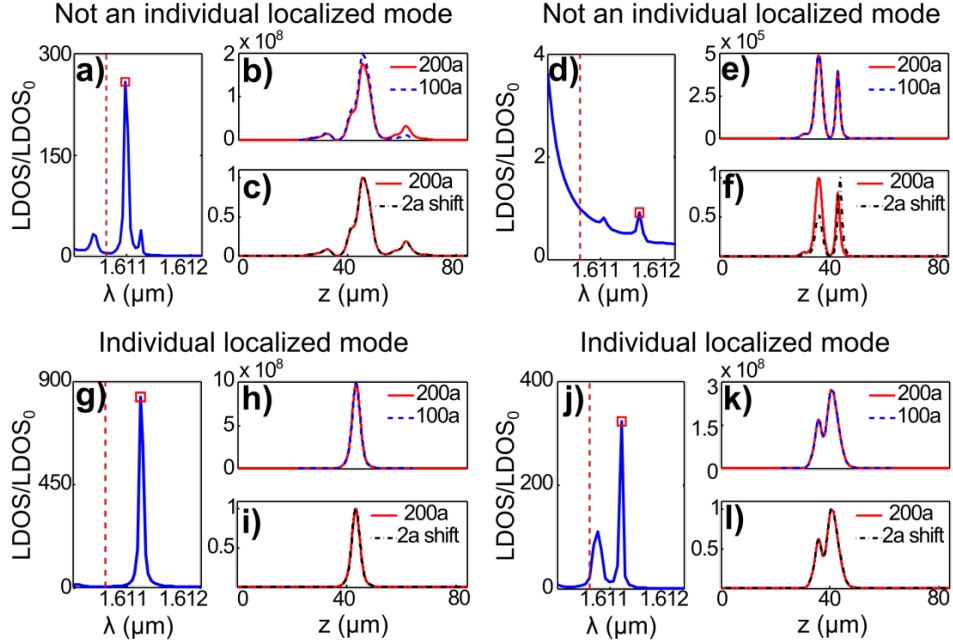


Figure A3-1. Examples of resonances that are or are not accounted for in the distribution function of spatial extent of localized modes. a,d,g,j) Spectral dependence of the normalized LDOS obtained for a source placed in the center of the $100a$ -long W1 waveguide. The vertical red dashed line indicates the band-edge wavelength λ_0 . **b,e,h,k)** Envelop of the magnetic-field-intensity profiles, $|H_{100}|^2$ and $|H_{200}|^2$, at the resonance wavelength for the $100a$ -long W1 waveguide (dashed blue line) and the extended $200a$ -long W1 waveguide (red solid line). **c,f,i,l)** Envelop of the magnetic-field-intensity profiles in the $200a$ -long W1 waveguide for a source positioned in the center (red solid line) and for the same right-shifted source (black dashed-dotted line). **a-c)** Resonance that is *not* considered as an individual localized mode (mode profile affected by the boundary). Here, $\sigma = 0.5 \text{ nm}$. **d-f)** Resonance that is *not* considered as an individual localized mode (mode profile affected by the source position). Here, $\sigma = 0.75 \text{ nm}$. **g-i)** Resonance that is considered as an individual localized mode. The extension length is $L = 6.4 \mu\text{m}$ and $\sigma = 0.5 \text{ nm}$. **j-l)** Resonance that is considered as an individual localized mode. The extension length is $L = 12.5 \mu\text{m}$ and $\sigma = 0.75 \text{ nm}$.

APPENDIX 4: WIDE-SLOT PHOTONIC CRYSTAL WAVEGUIDE WITH FULL BAND GAP MIRROR

In this Appendix, we investigate the design of a full photonic band gap mirror to be implemented in the wide-slot photonic crystal waveguide discussed in Chapter 3.

In the Chapter, we considered a square lattice offering a partial band gap. An alternative solution, commonly used in photonic crystal waveguide, is the triangular lattice. Photonic band gap computation using the MPB package for the same parameters (hole radius, period, membrane thickness) as Chapter 3 is shown in Figure A4-1a. As for the case of the square lattice, it does not provide a full band gap at the frequency of interest (represented by the red horizontal dashed line). However, a large full band gap exists at a slightly larger frequency. It suggests that only a small change in geometrical parameters may be sufficient to lower its frequency and match the operation frequency of the waveguide.

Intuitively, lowering the frequency of photonic bands amount to increase their effective index and thus the relative amount of high index material. One possible solution is to increase the periodicity of the lattice. As the periodicity in the propagation direction is fixed by the design criteria of the wide-slot photonic crystal waveguide, only the period in the transverse direction can be tuned.

Figure A4-1b shows the computation of the photonic bands of an elongated triangular lattice with a period $a_1 = 380$ nm in the propagation direction and a period $a_2 = 440$ nm in the transverse direction (see sketched in Fig. A4-2a). Let us note that the symmetry breaking caused by the elongation of the

periodicity in one direction distorts the irreducible first Brillouin zone (as sketched in the inset of Fig. A4-1b) and additional critical points must be considered to fully scan the reciprocal space. As predicted, the new lattice provides a full band gap at the frequency of interest. We also notice that the spectral width of the gap is reduced which can intuitively be explained by the reduction of the index modulation as the periodicity increases.

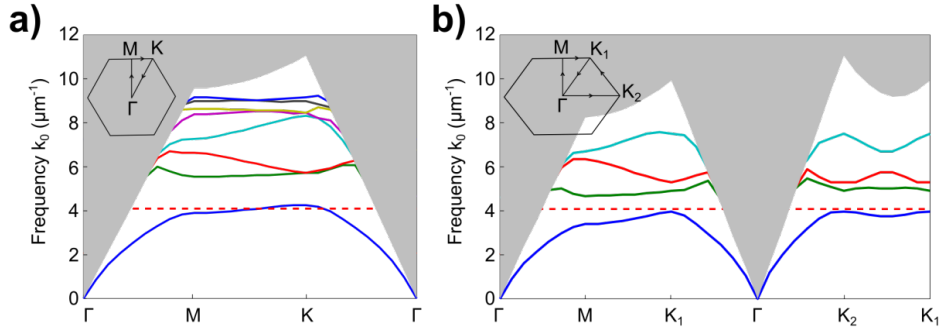


Figure A4-1. Photonic bands of photonic crystal mirrors. **a)** Photonic bands of a photonic crystal with a triangular lattice of air holes ($n = 1$) in a medium of index $n = 3.48$. The computation is realized for a period $a_M = 380$ nm, hole radius $r = 0.3a_M$ and membrane thickness 220 nm. **b)** Photonic bands of a photonic crystal with a triangular lattice stretched in one direction ($a_1 = 380$ nm and $a_2 = 440$ nm). The hole radius, membrane thickness and refractive indices are the same as in (a). **a-b)** The grey area represents the area above the air light line and the red dashed line represents the frequency of interest in the design. **Insets:** First Brillouin zone of the photonic crystal and critical points of the irreducible first Brillouin zone.

The elongated triangular lattice can thus provide a full band gap at the frequency of interest. However, the implementation of a full band gap does not modify the properties of the wide-slot waveguide since guidance was already ensured by the partial gap of the square lattice and no significant modification of the effective mass is observed in the mode dispersion curves plotted in Fig A4-2b.

To summarize, both the square lattice and the elongated triangular lattice are suitable for the design of the wide-slot waveguide. However, for reasons of calculation time, we have decided to use the square lattice for the final design.

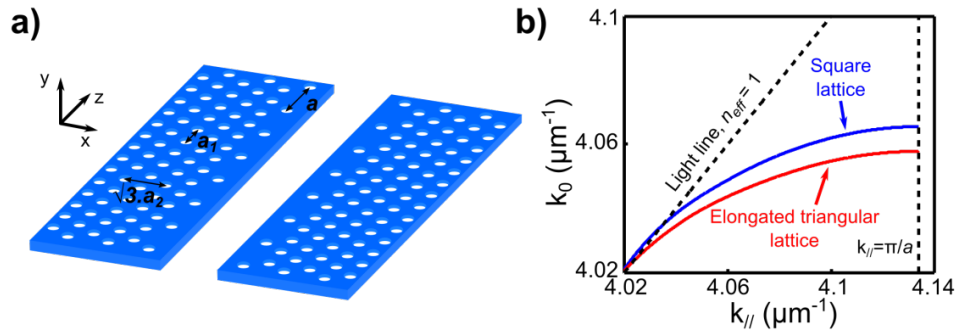


Figure A4-2. Wide-slot PhC waveguide with an elongated triangular lattice. **a)** Sketch of the wide-slot PhC waveguide with an elongated triangular lattice. The periods of the mirrors are respectively $a_1 = 380$ nm in the propagation direction and $a_2 = 440$ nm in the transverse direction. **b)** Dispersion curves of the wide-slot waveguide presented in Chapter 3 (blue) and with the elongated triangular lattice (red). The latter has a waveguide width $L_g = 280$ nm. Other parameters are identical. The black dashed lines represent the light line and the edge of the first Brillouin zone.

APPENDIX 5: CONVERGENCE OF THE FDTD AND TEMPORAL QNM-EXPANSION METHODS

Comparison of the temporal responses computed with the FDTD method and the QNM-expansion formalism reveals discrepancies in the phase and amplitude of the temporal signal. Hereafter, we study the accuracy of the two approaches as a function of the mesh discretization to check their respective convergence.

In Fig. A5-1a, we show FDTD computations realized for 3 different mesh sizes, $1.5 \times 1.5 \times 1.5 \text{ nm}^3$ (red), $0.75 \times 0.75 \times 0.75 \text{ nm}^3$ (blue) and $0.25 \times 0.25 \times 0.25 \text{ nm}^3$ (black). The three computations clearly gives different responses. In the first beating oscillations, responses are in phase but amplitude is different. More significant, the responses at long t 's (inset) display both large amplitude and phase differences. Even though the two finer meshes give more similar results, the FDTD method does not seem to converge.

In Fig. A5-1b, we show computational results obtained with the QNM-expansion formalism for three different meshes. The mesh sizes in the dolmen are approximately equal to $\sim \lambda/30 \approx 20 \text{ nm}$ (red), $\sim \lambda/150 \approx 4 \text{ nm}$ (blue) and $\sim \lambda/300 \approx 2 \text{ nm}$ (black). Small amplitude and phase differences are observed in the responses, but an overall agreement is achieved, even for meshes much coarser than those used for the FDTD computations. The more significant discrepancy, a slight phase shift for long t 's (inset), is attributed to numerical dispersion of the resonance frequencies, the relative difference between the resonance frequencies computed with mesh 1 and 3 being about 1%.

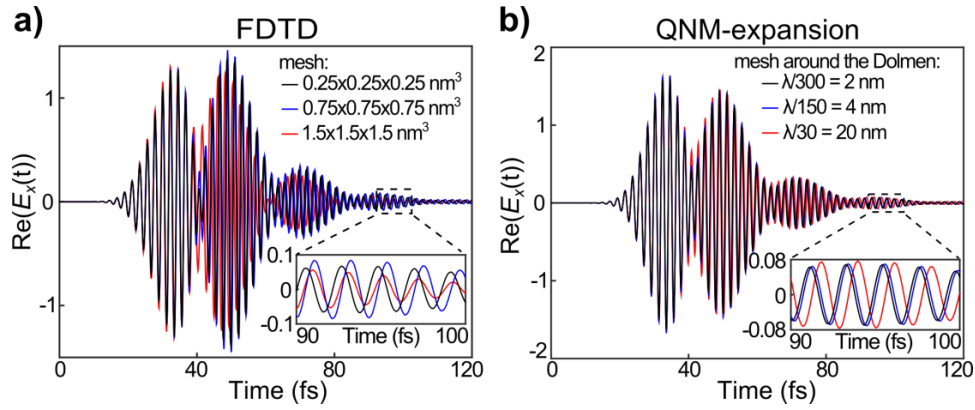


Figure A5-1. FDTD and QNM-expansion computational results for different meshes for the field at point A of the Dolmen, see Fig. 4-5a of Chapter 4 for details. **a)** FDTD computations are performed for meshes of $1.5 \times 1.5 \times 1.5 \text{ nm}^3$ (red), $0.75 \times 0.75 \times 0.75 \text{ nm}^3$ (blue) and $0.25 \times 0.25 \times 0.25 \text{ nm}^3$ (black). **b)** QNM-expansion computations are performed for refined mesh around the dolmen of size $\sim \lambda/30 \approx 20 \text{ nm}$ (red), $\sim \lambda/150 \approx 4 \text{ nm}$ (blue) and $\sim \lambda/300 \approx 2 \text{ nm}$ (black). Insets: zoom of the responses for $90 < t < 100 \text{ fs}$.

We note that, for both methods, the phase of the signal for all meshes is identical in the first beating period (which corresponds to the crossing with the driving pulse) and discrepancies on the phase only occur at longer t 's. This suggests that the first oscillations are not very impacted by the three dominant resonance frequencies of the Dolmen.

The QNM-expansion formalism implemented with second-order finite-elements exhibits a fast convergence rate, much faster than the FDTD method that relies on finite-differences. This explains why a better accuracy is achieved with the QNM-expansion at long t 's in Chapter 4.

APPENDIX 6: APPROXIMATION ON THE DISPERSION IN THE TEMPORAL QNM-EXPANSION

The QNM-expansion developed in Chapter 4 is computed by assuming that the frequency dependence of $\Delta\varepsilon(\mathbf{r}, \omega)$ and $\exp(-ik(\omega)z)$ is negligible in the spectral window defined by the resonance term $1/(\omega - \omega_m)$. In this Appendix, we numerically check the validity of this assumption. In Fig. A6-1, we show the calculation of the temporal response of the Dolmen at the same location and for the same driving field as in Fig. 4-5a. of Chapter 4 performed by neglecting the dispersion of $\Delta\varepsilon(\mathbf{r}, \omega)$ and $\exp(-ik(\omega)z)$ (red) and without this approximation (black).

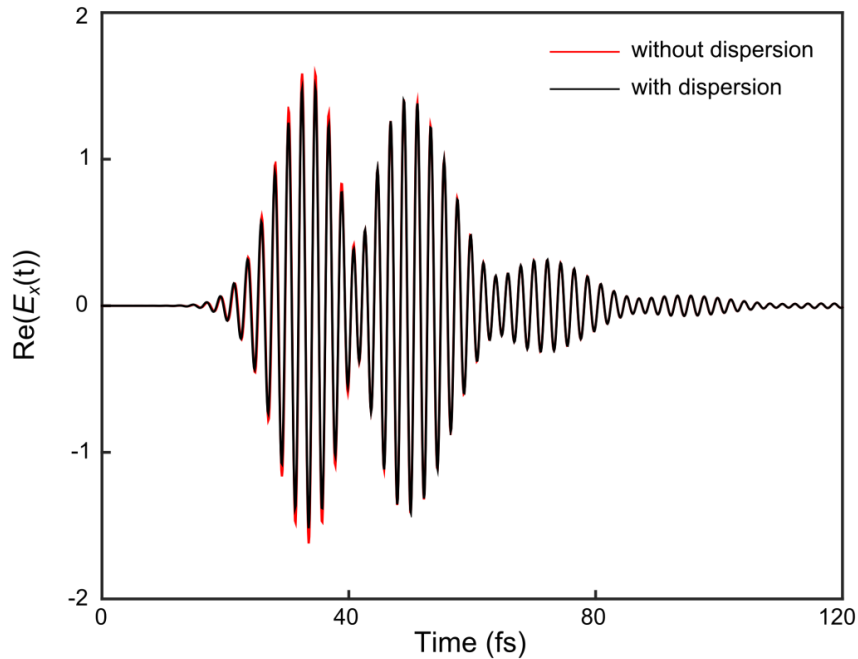


Figure A6-1. Test of the assumption on the dispersion in the QNM-expansion. The computations are performed for the gold Dolmen at the same location and for the same driving field as in Fig. 4-5a of Chapter 4. The red curve represents the calculation neglecting the frequency dependence of $\Delta\varepsilon(\mathbf{r}, \omega)$ and $\exp(-ik(\omega)z)$. The black curve represents the calculation without this assumption.

Both computations give almost identical predictions and only small discrepancies in the amplitude of the signal are observed at short t 's while the responses are superimposed for t 's larger than 40 fs. It suggests that only mode excitations are affected by the dispersion while the relaxation remains unchanged. One may conclude that the dominant dispersive term is in fact $\exp(-ik(\omega)z)$ while $\Delta\varepsilon(\mathbf{r},\omega)$ has only a small impact on the response. In conclusion, we can safely consider the approximation as valid. Similar observations can be done in the case of the rice-shaped nanoparticle.

APPENDIX 7: QUENCHING CALCULATION

In this Appendix, we describe the calculation techniques to evaluate the decay rates into quenching in an MIM structure and demonstrate its near-field nature.

A7.1 Indirect calculation of quenching

For the dipole emission into an MIM stack problem shown in Fig. 5-2 of Chapter 5, the dipole decays either into gap plasmons modes (γ_{GSP}) or couples directly to the metal (quenching, γ_{quench}). To estimate the quenching, we first calculate the total decay rate by integrating the total power emitted by the source over a box surrounding the source. Then with an open-source near-to-far-field transform (NFFT) tool [Yan16a], we obtain the decay into the propagative modes (γ_{GSP}). Finally γ_{quench} is *indirectly* calculated as the difference $\gamma_{quench} = \gamma_{tot} - \gamma_{GSP}$.

Note that, in previous works on dipole emission in MIM stacks [For84, Jun08], γ_{quench} is directly calculated by integrating the power coupled into all evanescent waves, i.e. into decay channels that are not associated to propagative modes. In contrast, in our work γ_{quench} is obtained in an indirect way, mainly because the calculations of γ_{tot} and the NFFT implementation are accurate and efficient. The validity of the indirect calculation by difference is shown in the next section.

The latter also applied for the quenching on a single interface shown in Fig. 5-1 of Chapter 5. The quenching decay rate is calculated as $\gamma_{quench} = \gamma_{tot} -$

$\gamma_{rad} - \gamma_{SP}$, where γ_{rad} and γ_{SP} are respectively the decay rates into free-space and surface plasmons.

A7.2 Verification of the indirect quenching calculation and localized nature of quenched fields

The following verification is motivated by two main reasons:

1/ Power does not sum up in absorbing media, and thus strictly speaking, we cannot decompose the total decay rate as a sum of decays into different channels. This decomposition is valid only in the limit of “weak absorptions”. Nothing guaranties that.

2/ Taking the example of metal-dielectric interfaces for simplicity, it is well known that absorption in the metal has (at least) three distinct origins: SPP launching, a quasi-cylindrical wave launching that alters the SPP absorption over an area of $\approx 100\lambda^2$ around the source [Loz14], and a localized absorption in the near-field of the source. This again implies that quenching (defined as the localized absorption) cannot be strictly obtained as a difference between the total decay and the sum of the decays into propagative modes.

It is therefore important to check numerically that this difference in power decays effectively corresponds to a localized absorption.

For that purpose, we consider a vertically-polarized dipole emitting at a wavelength of 650 nm in an MIM with a gap thickness $g = 8\text{ nm}$. Since the MIM stack laterally extends to infinity, all the emitted power is absorbed by the metal. The total field is shown in Fig. A7-1a. We can clearly see an intense field in the metal claddings in the immediate vicinity of the source. In a cylindrical coordinate (r, θ, z) , we define the absorbed power density as $A(r, \theta) = 0.5\omega \int \text{Im}(\varepsilon)|E(r, \theta)|^2 dz$. The total absorbed power (or total emitted

power) P_{tot} is simply $P_{tot} = \iint rA(r, \theta)drd\theta$. In Fig. A7-1b, the logarithm of $rA(r, \theta)$ is plotted with a red curve at an arbitrary azimuth (for a vertical dipole, the whole system is azimuthal-independent). The exponentially decaying tail (the linear part in the logarithm coordinates) of $rA(r, \theta)$ corresponds to the gap-plasmon damping $e^{-2\text{Im}(k_{GSP})r}$, with k_{GSP} denoting the propagation constant. A backward extrapolation of the tail (black dashed) to $r = 0$ offers a clear distinction between the respective contributions of gap plasmons and quenching (which occurs in a very short length scale around the source) to total absorption. The quenching area (between the red and black curves) is at deep subwavelength scale, revealing the localized nature of quenching.

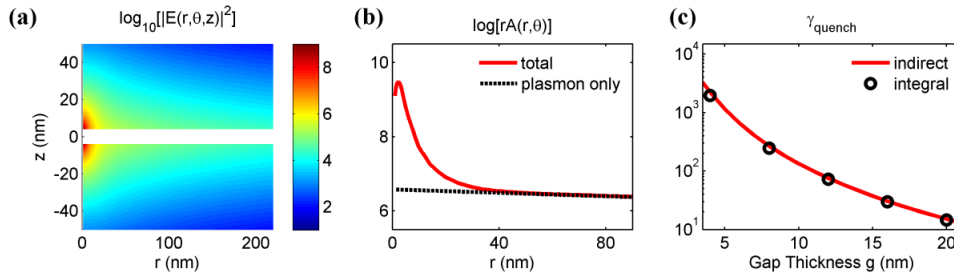


Figure A7-1. Localized nature of quenching. **a)** Intensity of the field excited at a wavelength of 650 nm by a vertical electric dipole in the center ($z = 0$ and $r = 0$) of an Ag/Polymer/Ag MIM stack with a gap thickness of $g = 8 \text{ nm}$. The field in the gap is not represented to better show the field in metal claddings. **b)** Radial plots of $rA(r, \theta)$ as a function of r (red solid) and of the exponential damping of gap plasmon (black dashed). **c)** γ_{quench} obtained by indirect calculation ($\gamma_{quench} = \gamma_{tot} - \gamma_{GSP}$, red line) and by integrating the density of quenched power (black circles), for varying gap thicknesses. In the calculation, the refractive index of polymer is $n = 1.4$ and the relative permittivity of silver is $\epsilon_{Ag} = -17 + 1.15i$.

As shown in Fig. A7-1c, quenching rate γ_{quench} (black circles) obtained by directly integrating the density of quenched power in real space matches γ_{quench} obtained with the indirect calculation (red lines). The quantitative agreement validates the indirect calculation.

BIBLIOGRAPHY

- [Acc14] N. Accanto, L. Piatkowski, J. Renger, and N. F. van Hulst, "Capturing the optical phase response of nanoantennas by coherent second-harmonic microscopy", *Nano Lett.* **14**, 4078 (2014).
- [Ada09] R. Adatoa, A. A. Yanika, J. J. Amsden, D. L. Kaplan, F. G. Omenetto, M. K. Hong, S. Erramilli, and H. Altug, "Ultra-sensitive vibrational spectroscopy of protein monolayers with plasmonic nanoantenna arrays", *PNAS* **106**, 19227-19232 (2009).
- [Aes10] M. Aeschlimann, M. Bauer, D. Bayer, T. Brixner, S. Cunovic, F. Dimler, A. Fischer, W. Pfeiffer, M. Rohmer, C. Schneider, F. Steeb, C. Strüber, and D. V. Voroninec, "Spatiotemporal control of nanooptical excitations", *PNAS* **107**, 5329 (2010).
- [Aes16] M. Aeschlimann, T. Brixner, A. Fischer, M. Hensen, B. Huber, D. Kilbane, C. Kramer, W. Pfeiffer, M. Picuch, and P. Thielen, "Determination of local optical response functions of nanostructures with increasing complexity by using single and coupled Lorentzian oscillator models", *Appl. Phys. B* **122**, 199 (2016).
- [Agi12] M. Agio, "Optical antennas as nanoscale resonators", *Nanoscale* **4**, 692–706 (2012).
- [Aks14] G. M. Akselrod, C. Argyropoulos, T. B. Hoang, C. Ciraci, C. Fang, J. Huang, D. R. Smith, and M. H. Mikkelsen, "Probing the mechanisms of large Purcell enhancement in plasmonic nanoantennas", *Nature Photon.* **8**, 835 (2014).
- [Alp16] F. Alpeggiani, P. Nikhil, E. Verhagen, and L. Kuipers, "Quasinormal-mode expansion of the scattering matrix", *arXiv preprint arXiv:1609.03902* (2016).
- [Arc14] M. Arcari, I. Söllner, A. Javadi, S. Lindskov Hansen, S. Mahmoodian, J. Liu, H. Thyrestrup, E. H. Lee, J. D. Song, S. Stobbe, and P. Lodahl, "Near-Unity Coupling Efficiency of a Quantum Emitter to a Photonic Crystal Waveguide", *Phys. Rev. Lett.* **113**, 093603 (2014).
- [Ash76] N. W. Ashcroft, and N. D. Mermin, "Solid State Physics" (Holt, Rinehart and Winston, 1976).
- [Atl10] K. A. Atlasov, M. Felici, K. Fredrik Karlsson, P. Gallo, A. Rudra, B. Dwir, and E. Kapon, "1D photonic band formation and photon localization in finite-size photonic-crystal waveguides", *Opt. Express* **18**, 117-122 (2010).

- [Atw10] H. A. Atwater, and A. Polman, "Plasmonics for improved photovoltaic devices", *Nat. Mater.* **9**, 205–213 (2010).
- [Bab16] F. Baboux, L. Ge, T. Jacqmin, M. Biondi, E. Galopin, A. Lemaître, L. Le Gratiet, I. Sagnes, S. Schmidt, H.E. Türeci, A. Amo, and J. Bloch, "Bosonic Condensation and Disorder-Induced Localization in a Flat Band", *Phys. Rev. Lett.* **116**, 066402 (2016).
- [Bai13] Q. Bai, M. Perrin, C. Sauvan, J. P. Hugonin, and P. Lalanne, "Efficient and intuitive method for the analysis of light scattering by a resonant nanostructure", *Opt. Express* **21**, 27371-27382 (2013).
- [Bar98] W. L. Barnes, "Fluorescence near interfaces: The role of photonic mode density", *J. Mod. Opt.* **45**, 661 (1998).
- [Bar09a] A. Baron, A. Ryasnyanskiy, N. Dubreuil, P. Delaye, Q. V. Tran, S. Combrié, A. de Rossi, R. Frey, and G. Roosen, "Light localization induced enhancement of third order nonlinearities in a GaAs photonic crystal waveguide", *Opt. Express* **17**, 552-557 (2009).
- [Bar09b] B. Barwick, D. J. Flannigan, and A. H. Zewail, "Photon-induced near-field electron microscopy", *Nature* **462**, 902 (2009).
- [Bar11] A. Baron, S. Mazoyer, W. Smigaj, and P. Lalanne, "Attenuation Coefficient of Single-Mode Periodic Waveguides", *Phys. Rev. Lett.* **107**, 153901 (2011).
- [Ben96] J. M. Bendickson, J. P. Dowling, and M. Scalora, "Analytic expressions for the electromagnetic mode density in finite, one-dimensional, photonic band-gap structure", *Phys. Rev. E* **53**, 4107-4121 (1996).
- [Ben03] M. P. Bendsøe and O. Sigmund, *Topology optimization — Theory, Methods and Applications* (Springer-Verlag, 2003).
- [Ber03] D. J. Bergman, and M. I. Stockman, "Surface plasmon amplification by stimulated emission of radiation: quantum generation of coherent surface plasmons in nanosystems", *Phys. Rev. Lett.* **90**, 027402 (2003).
- [Ber05] J. Bertolotti, S. Gottardo, D. S. Wiersma, M. Ghulinyan, and L. Pavesi, "Optical necklace states in Anderson localized 1D systems", *Phys. Rev. Lett.* **94**, 113903 (2005).
- [Ber10] S. Berweger, J. M. Atkin, R. L. Olmon, and M. B. Raschke, "Adiabatic Tip-Plasmon Focusing for Nano-Raman Spectroscopy", *J. Phys. Chem. Lett.* **1**, 3427 (2010).
- [Bes07] M. Besbes, J.P. Hugonin, P. Lalanne, S. van Haver, O.T.A. Janssen, A.M. Nugrowati, M. Xu, S.F. Pereira, H.P. Urbach, A.S. van de Nes, P. Bienstman, G. Granet, A. Moreau, S. Helfert, M. Sukharev, T. Seideman, F. I. Baida, B. Guizal, and D. Van Labeke, "Numerical analysis of a slit-groove diffraction problem", *J. Eur. Opt. Soc. Rapid Publ.* **2**, 07022 (2007).

- [Bir95] T. A. Birks, P.J. Roberts, P. S. J. Russell, D. M. Atkin, and T. J. Shepherd, "Full 2-D photonic band gaps in silica/air structures", *Electron. Lett.* **31**, 1941-1943 (1995).
- [Ble11] J. Bleuse, J. Claudon, M. Creasey, N. S. Malik, and J. M. Gérard, "Inhibition, Enhancement, and Control of Spontaneous Emission in Photonic Nanowires", *Phys. Rev. Lett.* **106**, 103601 (2011).
- [Bli08] K. Y. Bliokh, Y. P. Bliokh, V. Freilikher, S. Savel'ev, and F. Nori, "Colloquium: Unusual resonators: Plasmonics, metamaterials, and random media", *Rev. Mod. Phys.* **80**, 1201–1213 (2008).
- [Bri13] D. Brinks, M. Castro-Lopez, R. Hildner, and N. F. van Hulst, "Plasmonic antennas as design elements for coherent ultrafast nanophotonics", *PNAS* **110**, 18386 (2013).
- [Bol07] S. I. Bozhevolnyi, and T. Søndergaard, "General properties of slow-plasmon resonant nanostructures: nano-antennas and resonators", *Opt. Express* **15**, 10869-10877 (2007).
- [Boy11] R. W. Boyd, "Material slow light and structural slow light: similarities and differences for nonlinear optics [invited]", *J. Opt. Soc. Am. B* **28**, A38–A44 (2011).
- [Bul96] S. A. Bulgakov, and M. Nieto-Vesperinas, "Competition of different scattering mechanisms in a one-dimensional random photonic lattice", *J. Opt. Soc. Am. A* **13**, 500–508 (1996).
- [Cao02] Q. Cao, P. Lalanne, and J. P. Hugonin, "Stable and efficient Bloch-mode computational method for one-dimensional grating waveguides", *J. Opt. Soc. Am. A* **19**, 335-338 (2002).
- [Cha10] J. T. Chalker, T. S. Pickles, and P. Shukla, "Anderson localization in tight-binding models with flat bands", *Phys. Rev. B* **82**, 104209 (2010).
- [Che94] W. C. Chew, and W. H. Weedon, "A 3D perfectly matched medium from modified maxwell's equations with stretched coordinates", *Microw. Opt. Technol. Lett.* **7**, 599–604 (1994).
- [Col04] R. E. Collin, "Hertzian dipole radiating over a lossy earth and sea: some early and late 20th-century controversies", *IEEE Antennas Propag. Mag.* **46**, 64-79 (2004).
- [Con08] C. Conti, and A. Fratalocchi, "Dynamic light diffusion, Anderson localization and lasing in disordered inverted opals: 3D ab-initio Maxwell-Bloch computation", *Nat. Phys.* **4**, 794–798 (2008).
- [Cor09] B. Corcoran, C. Monat, C. Grillet, D. J. Moss, B. J. Eggleton, T. P. White, L. O'Faolain, and T. F. Krauss, "Green light emission in silicon through slow-light enhanced third-harmonic generation in photonic-crystal waveguides", *Nat. Photon.* **3**, 206-210 (2009).
- [Cot72] A.A. Cottley, "Solutions of Schrodinger's equation at a band edge in a one dimensional crystal", *J. Phys. C: Solid State Phys.* **5**, 2583-2590 (1972).

- [Csa11] A. Csaki, T. Schneider, J. Wirth, N. Jahr, A. Steinbrück, O. Stranik, F. Garwe, R. Müller, and W. Fritzsche, "Molecular plasmonics: light meets molecules at the nanoscale", *Phil. Trans. R. Soc. A* **369**, 3483–3496 (2011).
- [Del12] J. Dellinger, K. Van Do, X. Le Roux, F. de Fornel, E. Cassan, and B. Cluzel, "Hyperspectral optical near-field imaging: Looking graded photonic crystals and photonic metamaterials in color", *Appl. Phys. Lett.* **101**, 141108 (2012).
- [Dey98] L. I. Deych, D. Zaslavsky, and A. A. Lisyansky, "Statistics of the Lyapunov Exponent in 1D Random Periodic-on-Average Systems", *Phys. Rev. Lett.* **81**, 5390–5393 (1998). [Dic12] I. Dicaire, A. De Rossi, S. Combrié, and L. Thévenaz, "Probing molecular absorption under slow-light propagation using a photonic crystal waveguide", *Opt. Letters* **37**, 4934–4936 (2012).
- [Doo13] M. B. Doost, W. Langbein, and E. A. Muljarov, "Resonant state expansion applied to two-dimensional open optical systems", *Phys. Rev. A* **87**, 043827 (2013).
- [Dou15] J. S. Douglas, H. Habibian, C.-L. Hung, A.V. Gorshkov, H. J. Kimble, and D. E. Chang, "Quantum many-body models with cold atoms coupled to photonic crystals", *Nat. Photonics* **9**, 326 (2015).
- [Dow94] J. P. Dowling, M. Scalora, M.J. Bloemer, and C. M. Bowden, "The photonic band-edge laser: a new approach to gain enhancement mode", *J. Appl. Phys.* **76**, 1896–99 (1994).
- [Dre74] K. H. Drexhage, "Interaction of light with monomolecular dye layers", *Prog. Optics* **12**, 165 (1974).
- [Dua04] L.-M. Duan and H. Kimble, "Scalable Photonic Quantum Computation through Cavity-Assisted Interactions", *Phys. Rev. Lett.* **92**, 127902 (2004).
- [Egg15] M. S. Eggleston, K. Messer, L. Zhang, E. Yablonovitch, and M. C. Wu, "Optical antenna enhanced spontaneous emission", *Proc. Natl. Acad. Sci.* **112**, 1704–1709 (2015).
- [Fae14] S. Faez, P. Turschmann, H. R. Haakh, S. Gotzinger, and V. Sandoghdar, "Coherent Interaction of Light and Single Molecules in a Dielectric Nanoguide", *Phys. Rev. Lett.* **113**, 213601 (2014).
- [Fag16] R. Faggiani, A. Baron, X. Zang, L. Lalouat, S. A. Schulz, B. O'Regan, K. Vynck, B. Cluzel, F. de Fornel, T. F. Krauss, and P. Lalanne, "Lower bound for the spatial extent of localized modes in photonic-crystal waveguides with small random imperfections", *Sci. Rep.* **6**, 27037 (2016).
- [Fer10] A. I. Fernandez-Dominguez, S. A. Maier, and J. B. Pendry, "Collection and Concentration of Light by Touching Spheres: A Transformation Optics Approach", *Phys. Rev. Lett.* **105**, 266807 (2010).

- [For84] G. W. Ford, and W. H. Weber, "Electromagnetic interactions of molecules with metal surfaces", *Phys. Rep.* **113**, 195-287 (1984).
- [Fra06] L. H. Frandsen, A.V. Lavrinenko, J. Fage-Pedersen, and P. I. Borel, "Photonic crystal waveguides with semi-slow light and tailored dispersion properties", *Opt. Express* **14**, 9444 (2006).
- [Gao13] J. Gao, S. Combrie, B. Liang, P. Schmitteckert, G. Lehoucq, S. Xavier, X. Xu, K. Busch, D. L. Huffaker, A. De Rossi & C. Wei Wong, "Strongly coupled slow-light polaritons in one-dimensional disordered localized states", *Sci. Rep.* **3**, 1994 (2013).
- [Gar10] P. D. García, S. Smolka, S. Stobbe, and P. Lodahl, "Density of states controls Anderson localization in disordered photonic crystal waveguides", *Phys. Rev. B* **82**, 165103 (2010).
- [Gia11] V. Giannini, A. I. Fernandez-Domínguez, S. C. Heck, and S. A. Maier, "Plasmonic nanoantennas: fundamentals and their use in controlling the radiative properties of nanoemitters", *Chem. Rev.* **111**, 3888 (2011).
- [Gob14] A. Goban, C. L. Hung, S. P. Yu, J. D. Hood, J. A. Muniz, J. H. Lee, M. J. Martin, A. C. McClung, K. S. Choi, D. E. Chang, O. Painter, and H. J. Kimble, "Atom-Light Interactions in Photonic Crystals", *Nat. Commun.* **5**, 3808 (2014).
- [Gob15] A. Goban, C. L. Hung, J. D. Hood, S. P. Yu, J. A. Muniz, O. Painter, and H. J. Kimble, "Superradiance for Atoms Trapped along a Photonic Crystal Waveguide", *Phys. Rev. Lett.* **115**, 063601 (2015).
- [Gra96] G. Granet, and B. Guizal, "Efficient implementation of the coupled-wave method for metallic lamellar gratings in TM polarization", *J. Opt. Soc. Am. A* **13**, 1019-1023 (1996).
- [Gra14] D. K. Gramotnev and S. I. Bozhevolnyi, "Nanofocusing of electromagnetic radiation", *Nat. Photon.* **8**, 13–22 (2014).
- [Haa15] H. R. Haakh, S. Faez, and V. Sandoghdar "Polaritonic states in a dielectric nanoguide: localization and strong coupling", arXiv preprint arXiv:1510.07979 (2015).
- [Han09] T. Hanke, G. Krauss, D. Trautlein, B. Wild, R. Bratschitsch, and A. Leitenstorfer, "Efficient Nonlinear Light Emission of Single Gold Optical Antennas Driven by Few-Cycle Near-Infrared Pulses", *Phys. Rev. Lett.* **103**, 257404 (2009).
- [Het11] G. Hétet, L. Slodička, M. Hennrich, and R. Blatt, "Single Atom as a Mirror of an Optical Cavity", *Phys. Rev. Lett.* **107**, 133002 (2011).
- [Hua09] J. S. Huang, D. V. Voronine, P. Tuchscherer, T. Brixner, and B. Hecht, "Deterministic spatiotemporal control of optical fields in nanoantennas and plasmonic circuits", *Phys. Rev. B* **79**, 195441 (2009).
- [Hug05a] S. Hughes, L. Ramunno, J. Young, and J. Sipe, "Extrinsic Optical Scattering Loss in Photonic Crystal Waveguides: Role of Fabrication

- Disorder and Photon Group Velocity", *Phys. Rev. Lett.* **94**, 033903 (2005).
- [Hug05b] J. P. Hugonin, and P. Lalanne, "Perfectly matched layers as nonlinear coordinate transforms: a generalized formalization", *J. Opt. Soc. Am. A* **22**, 1844-1849 (2005).
- [Hug07] J. P. Hugonin, P. Lalanne, T. White, and T. F. Krauss, "Coupling into slow-mode photonic crystal waveguides", *Opt. Letters* **32**, 2638-2640 (2007).
- [Hui12] S. R. Huisman, G. Ctistis, S. Stobbe, A. P. Mosk, J. L. Herek, A. Lagendijk, P. Lodahl, W. L. Vos, and P. W. H. Pinkse, "Measurement of a band-edge tail in the density of states of a photonic-crystal waveguide", *Phys. Rev. B* **86**, 155154 (2012).
- [Izr09] F. M. Izrailev, and N. M. Makarov, "Localization in Correlated Bilayer Structures: From Photonic Crystals to Metamaterials and Semiconductor Superlattices", *Phys. Rev. Lett.* **102**, 203901 (2009).
- [Joa08] J. D. Joannopoulos, S. G. Johnson, J. N. Winn, and R. D. Meade, *Photonic Crystals: Molding the Flow of Light*, 2nd ed. (Princeton University, 2008).
- [Joh87] S. John, "Strong localization of photons in certain disordered dielectric superlattices", *Phys. Rev. Lett.* **58**, 2486-2489 (1987)
- [Joh01] S. Johnson and J. Joannopoulos, "Block-iterative frequency- domain methods for maxwell's equations in a planewave basis", *Opt. Express* **8**, 173 (2001).
- [Jun08] Y. C. Jun, R. D. Kekatpure, J. S. White, and M. L. Brongersma, "Nonresonant enhancement of spontaneous emission in metal-dielectric-metal plasmon waveguide structures", *Phys. Rev. B* **78**, 153111 (2008).
- [Kal06] M. A. Kaliteevski, D. M. Beggs, S. Brand, R. A. Abram, and V. V. Nikolaev, "Statistics of the eigenmodes and optical properties of onedimensional disordered photonic crystals", *Phys. Rev. E* **73**, 056616 (2006).
- [Kha12] M. Khajavikhan, A. Simic, M. Katz, J. H. Lee, B. Slutsky, A. Mizrahi, V. Lomakin, and Y. Fainman, "Thresholdless nanoscale coaxial lasers", *Nature* **482**, 204 (2012).
- [Khu15] J. B. Khurgin, "How to deal with the loss in plasmonics and metamaterials", *Nat. Nanotech.* **10**, 2–6 (2015).
- [Kie04] F. Le Kien, V. I. Balykin, and K. Hakuta, "Atom trap and waveguide using a two-color evanescent light field around a subwavelength-diameter optical fiber", *Phys. Rev. A* **70**, 063403 (2004).
- [Kie05] F. Le Kien, S. Dutta Gupta, V. I. Balykin, and K. Hakuta, "Spontaneous emission of a cesium atom near a nanofiber: Efficient coupling of light to guided modes", *Phys. Rev. A* **72**, 032509 (2005).

- [Kim08a] H. J. Kimble, "The quantum internet", *Nature* **453**, 1023-1030 (2008).
- [Kim08b] S. Kim, J. Jin, Y. J. Kim, I. Y. Park, Y. Kim, and S. W. Kim, "High harmonic generation by resonant plasmon field enhancement", *Nature* **453**, 757 (2008).
- [Kin09] A. Kinkhabwala, Z. Yu, S. Fan, Y. Avlasevich, K. Müllen, and W. E. Moerner, "Large single-molecule fluorescence enhancements produced by a bowtie nanoantenna", *Nature Photon.* **3**, 654-657 (2009).
- [Kni96] J. C. Knight, T. A. Birks, P. St. J. Russell, and D. M. Atkin, "All-silica single-mode optical fiber with photonic crystal cladding", *Opt. Letters* **21**, 1547-1549 (1996).
- [Koe05] A. Koenderink, M. Kafesaki, B. Buchler, and V. Sandoghdar, "Controlling the Resonance of a Photonic Crystal Microcavity by a Near-Field Probe", *Phys. Rev. Lett.* **95**, 153904 (2005).
- [Koh59] W. Kohn, "Analytic properties of Bloch waves and Wannier functions", *Phys. Rev.* **115**, 809-821 (1959).
- [Kon15] K. Kondo, N. Ishikura, T. Tamura, and T. Baba, "Temporal pulse compression by dynamic slow-light tuning in photonic-crystal waveguides", *Phys. Rev. A* **91**, 023831 (2015).
- [Kra16a] A. Krasnok, S. Glybovski, M. Petrov, S. Makarov, R. Savelev, P. Belov, C. Simovski, and Y. Kivshar, "Demonstration of the enhanced Purcell factor in all-dielectric structures", *Appl. Phys. Lett.* **108**, 211105 (2016).
- [Kra16b] V. Kravtsov, R. Ulbricht, J. M. Atkin, and M. B. Raschke, "Plasmonic nanofocused four-wave mixing for femtosecond near-field imaging", *Nature Nano.* **11**, 459 (2016).
- [Kub05] A. Kubo, K. Onda, H. Petek, Z. Sun, Y. S. Jung, and H. Koo Kim, "Femtosecond Imaging of Surface Plasmon Dynamics in a Nanostructured Silver Film", *Nano Lett.* **5**, 1123 (2005).
- [Kur06] E. Kuramochi, M. Notomi, S. Mitsugi, A. Shinya, T. Tanabe, and T. Watanabe, "Ultrahigh-Q photonic crystal nanocavities realized by the local width modulation of a line defect", *Appl. Phys. Lett.* **88**, 041112 (2006).
- [Lag09] A. Lagendijk, B. van Tiggelen, and D. S. Wiersma, "Fifty years of Anderson localization", *Phys. Today* **62**, 24-29 (2009).
- [Lai11] W. C. Lai, S. Chakravarty, X. Wang, C. Lin, and R. T. Chen, "On-chip methane sensing by near-IR absorption signatures in a photonic crystal slot waveguide", *Opt. Lett.* **36**, 984-986 (2011).
- [Lal96] P. Lalanne, and G. M. Morris, "Highly improved convergence of the coupled-wave method for TM polarization", *J. Opt. Soc. Am. A* **13**, 779-784 (1996).
- [Lal00] P. Lalanne, and E. Silberstein, "Fourier-modal methods applied to waveguide computational problems", *Opt. Lett.* **25**, 1092-1094 (2000).

- [Lal02] P. Lalanne, "Electromagnetic analysis of photonic crystal waveguides operating above the light cone", *IEEE J. Quant. Electron.* **38**, 800–804 (2002).
- [Lal08] P. Lalanne, C. Sauvan, and J.P. Hugonin, "Photon confinement in photonic crystal nanocavities", *Laser Photon. Rev.* **2**, 514-526 (2008).
- [Lal09] P. Lalanne, J. P. Hugonin, H. T. Liu, and B. Wang, "A microscopic view of the electromagnetic properties of sub- λ metallic surfaces", *Surf. Sci. Rep.* **64**, 453-469 (2009).
- [Las13] J. B. Lassiter, F. McGuire, J. J. Mock, C. Ciraci, R. T. Hill, B. J. Wiley, A. Chilkoti, and D. R. Smith, "Plasmonic waveguide modes of film-coupled metallic nanocubes", *Nano Lett.* **13**, 5866-5872 (2013).
- [Lec07a] G. Lecamp, J. P. Hugonin, and P. Lalanne, "Theoretical and computational concepts for periodic optical waveguides", *Opt. Express* **15**, 11042-11060 (2007).
- [Lec07b] G. Lecamp, P. Lalanne, and J. P. Hugonin, "Very Large Spontaneous-Emission β Factors in Photonic-Crystal Waveguides", *Phys. Rev. Lett.* **99**, 023902 (2007).
- [Leu94a] P. T. Leung, S. Y. Liu, and K. Young, "Completeness and orthogonality of quasinormal modes in leaky optical cavities", *Phys. Rev. A* **49**, 3057 (1994).
- [Leu94b] P. T. Leung, S. Y. Liu, and K. Young, "Completeness and time-independent perturbation of the quasinormal modes of an absorptive and leaky cavity", *Phys. Rev. A* **49**, 3982 (1994).
- [Li93] L. Li, and C. W. Haggans, "Convergence of the coupled-wave method for metallic lamellar diffraction gratings", *J. Opt. Soc. Am. A* **10**, 1184-1189 (1993).
- [Li96a] L. Li, "Use of Fourier series in the analysis of discontinuous periodic structures", *J. Opt. Soc. Am. A* **13**, 1870-1876 (1996).
- [Li96b] L. Li, "Formulation and comparison of two recursive matrix algorithms for modeling layered diffraction gratings", *J. Opt. Soc. Am. A* **13**, 1024-1035 (1996).
- [Li97] L. Li, "New formulation of the Fourier modal method for crossed surface-relief gratings", *J. Opt. Soc. Am. A* **14**, 2758-2767 (1997).
- [Lif64] I. Lifshitz, "The energy spectrum of disordered systems", *Adv. Phys.* **13**, 483–536 (1964).
- [Liu11] N. Liu, M. L. Tang, M. Hentschel, H. Giessen, and A. P. Alivisatos, "Nanoantenna-enhanced gas sensing in a single tailored nanofocus", *Nat. Mat.* **10**, 631-636 (2011).
- [Liu14] J. Liu, P. D. Garcia, S. Ek, N. Gregersen, T. Suhr, M. Schubert, J. Mørk, S. Stobbe, and P. Lodahl, "Random nanolasing in the Anderson localized regime", *Nat. Nanotechnol.* **9**, 285–289 (2014).

- [Lod15] P. Lodahl, S. Mahmoodian, and S. Stobbe, "Interfacing single photons and single quantum dots with photonic nanostructures", *Rev. Mod. Phys.* **87**, 347 (2015).
- [Lov13] A. Lovera, B. Gallinet, P. Nordlander and O. J. F. Martin, "Mechanisms of Fano resonances in coupled Plasmonic Systems", *ACS Nano* **7**, 4527-36 (2013).
- [Loz14] O. Lozan, M. Perrin, B. Ea-Kim, J. M. Rampnoux, S. Dilhaire, and P. Lalanne, "Anomalous light absorption around subwavelength apertures in metal films", *Phys. Rev. Lett.* **112**, 193903 (2014).
- [Lun08] T. Lund-Hansen, S. Stobbe, B. Julsgaard, H. Thyrrstrup, T. Sünner, M. Kamp, A. Forchel, and P. Lodahl, "Experimental Realization of Highly Efficient Broadband Coupling of Single Quantum Dots to a Photonic Crystal Waveguide", *Phys. Rev. Lett.* **101**, 113903 (2008).
- [Man15] N. Mann, A. Javadi, P. D. García, P. Lodahl, and S. Hughes, "Theory and experiments of disorder-induced resonance shifts and mode edge broadening in deliberately disordered photonic crystal waveguides", *Phys. Rev. A* **92**, 023849 (2015).
- [Mar15] E. Marsell, A. Losquin, R. Svärd, M. Miranda, C. Guo, A. Harth, E. Lorek, J. Mauritsson, C. L. Arnold, H. Xu, A. L'Huillier, and A. Mikkelsen, "Nanoscale Imaging of Local Few-Femtosecond Near-Field Dynamics within a Single Plasmonic Nanoantenna", *Nano Lett.* **15**, 6601 (2015).
- [Maz09] S. Mazoyer, J. P. Hugonin, and P. Lalanne, "Disorder-Induced Multiple Scattering in Photonic-Crystal Waveguides", *Phys. Rev. Lett.* **103**, 063903 (2009).
- [Maz10] S. Mazoyer, P. Lalanne, J.C. Rodier, J. P. Hugonin, M. Spasenović, L. Kuipers, D.M. Beggs, and T.F. Krauss, "Statistical fluctuations of transmission in slow light photonic-crystal waveguides", *Opt. Express* **18**, 14654–14663 (2010).
- [Mcg93] A. McGurn, K. Christensen, F. Mueller, and A. Maradudin, "Anderson localization in one dimensional randomly disordered optical systems that are periodic on average", *Phys. Rev. B* **47**, 120–125 (1993).
- [Mel14] D. Melati, A. Melloni, and F. Morichetti, "Real photonic waveguides: guiding light through imperfections", *Adv. Opt. Photonics* **6**, 156–224 (2014).
- [Min13] M. Minkov, and V. Savona, "Long-distance radiative excitation transfer between quantum dots in disordered photonic crystal waveguides", *Phys. Rev. B* **88**, 081303 (2013).
- [Miy06] H. T. Miyazaki, and Y. Kurokawa, "Squeezing visible light waves into a 3-nm-thick and 55-nm-long plasmon cavity", *Phys. Rev. Lett.* **96**, 097401 (2006).
- [Moh81] M. G. Moharam, and T.K. Gaylord, "Rigorous coupled-wave analysis of planar-grating diffraction", *J. Opt. Soc. Am.* **71**, 811-818 (1981).

- [Moh95] M. G. Moharam, E. B. Grann, D. A. Pommet, and T. K. Gaylord, "Formulation for stable and efficient implementation of the rigorous coupled-wave analysis of binary gratings", *J. Opt. Soc. Am. A* **12**, 1068-1076 (1995).
- [Mok12] S. Mookapati, and K. R. Catchpole, "Nanophotonic light trapping in solar cells", *J. Appl. Phys.* **112**, 101101 (2012).
- [Moo08] S. Mookherjea, J.S. Park, S-H. Yang, and P.R. Bandaru, "Localization in silicon nanophotonic slow-light waveguides", *Nat. Photon.* **2**, 90-93 (2008).
- [Mor14] J. Mork, Y. Chen, and M. Heuck, "Photonic Crystal Fano Laser: TeraHertz Modulation and Ultrashort Pulse Generation", *Phys. Rev. Lett.* **113**, 163901 (2014).
- [Mub12] S. Mubeen, S. Zhang, N. Kim, S. Lee, S. Krämer, H. Xu, and M. Moskovits, "Plasmonic properties of gold nanoparticles separated from gold mirror by an ultrathin oxide", *Nano Lett.* **12**, 2088-2094 (2012).
- [Muc10] M. Mücke, E. Figueroa, J. Bochmann, C. Hahn, K. Murr, S. Ritter, C. J. Villas Boas, and G. Rempe, "Electromagnetically induced transparency with single atoms in a cavity", *Nature* **465**, 755 (2010).
- [Muh05] P. Mühlischlegel, H.-J. Eisler, O. J. F. Martin, B. Hecht, and D. W. Pohl, "Resonant Optical Antennas", *Science* **308**, 1607 (2005).
- [Muj07] S. Mujumdar, A. F. Koenderink, T. Sünner, B. C. Buchler, M. Kamp, A. Forchel, and V. Sandoghdar, "Near-field imaging and frequency tuning of a high-Q photonic crystal membrane microcavity", *Opt. Express* **15**, 17214–17220 (2007).
- [Nai13] G. V. Naik, V. M. Shalaev and A. Boltasseva, "Alternative plasmonic materials: beyond gold and silver", *Adv. Mater.* **25**, 3264–3294 (2013).
- [Nie97] S. Nie, and S. R. Emory, "Probing single molecules and single nanoparticles by surface-enhanced raman scattering", *Science* **275**, 1102-1106 (1997).
- [Nis15] Y. Nishiyama, K. Imura, and H. Okamoto, "Observation of Plasmon Wave Packet Motions via Femtosecond Time-Resolved Near-Field Imaging Techniques", *Nano Lett.* **15**, 7657 (2015).
- [Not01] M. Notomi, K. Yamada, A. Shinya, J. Takahashi, C. Takahashi, and I. Yokohama, "Extremely Large Group-Velocity Dispersion of Line-Defect Waveguides in Photonic Crystal Slabs", *Phys. Rev. Lett.* **87**, 253902 (2001).
- [Not10] M. Notomi, "Manipulating light with strongly modulated photonic crystals", *Rep. Prog. Phys.* **73**, 096501 (2010).
- [Nov06] L. Novotny, and B. Hecht, "Principles of Nano-Optics" (Cambridge Univ. Press, Cambridge, 2006).

- [Ofa10] L. O'Faolain, S. A. Schulz, D. M. Beggs, T. P. White, M. Spasenović, L. Kuipers, F. Morichetti, A. Melloni, S. Mazoyer, J. P. Hugonin, P. Lalanne, and T. F. Krauss, "Loss engineered slow light waveguides", *Opt. Express* **18**, 27627–27638 (2010).
- [Oni13] S. Onishi, K. Matsuishi, J. Oi, T. Harada, M. Kusaba, K. Hirose, and F. Kannari, "Spatiotemporal control of femtosecond plasmon using plasmon response functions measured by near-field scanning optical microscopy (NSOM)", *Opt. Express* **21**, 26631 (2013).
- [Osk12] A. Oskooi, A. Mutapcic, S. Noda, J. D. Joannopoulos, S. P. Boyd, and S. G. Johnson, "Robust optimization of adiabatic tapers for coupling to slow-light photonic-crystal waveguides", *Opt. Express* **20**, 21558–21575 (2012).
- [Oul09] R. F. Oulton, V. J. Sorger, T. Zentgraf, R. M. Ma, C. Gladden, L. Dai, G. Bartal, and X. Zhang, "Plasmon lasers at deep subwavelength scale", *Nature* **461**, 629–632 (2009).
- [Pal98] E. D. Palik, "Handbook of Optical Constants", (Academic Press: San Diego, 1998).
- [Pel15] M. Pelton, "Modified spontaneous emission in nanophotonic structures", *Nature Photon.* **9**, 427–435 (2015).
- [Pia16] L. Piatkowski, N. Accanto, and N. F. van Hulst, "Ultrafast meets ultrasmall: controlling nanoantennas and molecules", *ACS Photonics* **3**, 1401 (2016).
- [Pod12] A. N. Poddubny, M. V. Rybin, M. F. Limonov, and Y. S. Kivshar, "Fano interference governs wave transport in disordered systems", *Nat. Commun.* **3**, 914 (2012).
- [Por11] S. L. Portalupi, M. Galli, M. Belotti, L. C. Andreani, T. F. Krauss, and L. O'Faolain, "Deliberate versus intrinsic disorder in photonic crystal nanocavities investigated by resonant light scattering", *Phys. Rev. B* **84**, 045423 (2011).
- [Pov04] M. L. Povinelli, S. G. Johnson, E. Lidorikis, J. D. Joannopoulos, and M. Soljačić, "Effect of a photonic band gap on scattering from waveguide disorder", *Appl. Phys. Lett.* **84**, 3639–3641 (2004).
- [Pov05] M. L. Povinelli, S. G. Johnson, and J. D. Joannopoulos, "Slow-light, band-edge waveguides for tunable time delays", *Opt. Express* **13**, 7145–7159 (2005).
- [Pur46] E. M. Purcell, "Spontaneous emission probabilities at radio frequencies", *Phys. Rev.* **69**, 681 (1946).
- [Rab02] P. Rabiei, W. H. Steier, C. Zhang and L. R. Dalton, "Polymer micro-ring filters and modulators", *J. Lightwave Technol.* **20**, 1968–1975 (2002).

- [Rai01] J. M. Raimond, M. Brune, and S. Haroche, "Manipulating quantum entanglement with atoms and photons in a cavity", *Rev. Mod. Phys.* **73**, 565 (2001).
- [Ram10] A. Raman, and S. Fan, "Photonic Band Structure of Dispersive Metamaterials Formulated as a Hermitian Eigenvalue Problem", *Phys. Rev. Lett.* **104**, 087401 (2010).
- [Rea12] C. P. Reardon, I. H. Rey, K. Welna, L. O'Faolain, and T. F. Krauss, "Fabrication and characterization of photonic crystal slow light waveguides and cavities", *J. Vis. Exp.* e50216, doi: 10.3791/50216 (2012).
- [Red13] B. Redding, S. F. Liew, R. Sarma, H. Cao, "Compact spectrometer based on a disordered photonic chip", *Nat. Photonics* **7**, 746–751 (2013).
- [Rin08] M. Ringler, A. Schwemer, M. Wunderlich, A. Nichtl, K. Kürzinger, T. A. Klar and J. Feldmann, "Shaping Emission Spectra of Fluorescent Molecules with Single Plasmonic Nanoresonators", *Phys. Rev. Lett.* **100**, 203002 (2008).
- [Ros14] A. Rose, T. B. Hoang, F. McGuire, J. J. Mock, C. Ciraci, D. R. Smith, and M. H. Mikkelsen, "Control of radiative processes using tunable plasmonic nanopatch antennas", *Nano Lett.* **14**, 4797-4802 (2014).
- [Rus12] K. J. Russell, T.-L. Liu, S. Cui, and E. L. Hu, "Large spontaneous emission enhancement in plasmonic nanocavities", *Nature Photon.* **6**, 459-462 (2012).
- [Sac95] Z. S. Sacks, D. M. Kingsland, R. Lee, and J. F. Lee, "A perfectly matched anisotropic absorber for use as an absorbing boundary condition", *IEEE Trans. Antennas Propag.* **43**, 1460–1463 (1995).
- [San07] P. Sanchis, J. Blasco, A. Martínez, and J. Martí, "Design of Silicon-Based Slot Waveguide Configurations for Optimum Nonlinear Performance", *J. Lightwave Technol.* **25**, 1298-1305 (2007).
- [San12] J. Sancho, J. Bourderionnet, J. Lloret, S. Combrié, I. Gasulla, S. Xavier, S. Sales, P. Colman, G. Lehoucq, D. Dolfi, J. Capmany, and A. De Rossi, "Integrable microwave filter based on a photonic crystal delay line", *Nat. Commun.* **3**, 1075 (2012).
- [Sap10] L. Sapienza, H. Thyrestrup, S. Stobbe, P. D. Garcia, S. Smolka, P. Lodahl, "Cavity quantum electrodynamics with Anderson-localized modes", *Science* **327**, 1352–1355 (2010).
- [Sau05] C. Sauvan, P. Lalanne, and J. P. Hugonin, "Slow-wave effect and mode-profile matching in photonic crystal microcavities", *Phys. Rev. B* **71**, 165118 (2005).
- [Sau09] C. Sauvan, J. P. Hugonin, and P. Lalanne, "Difference between penetration and damping lengths in photonic crystal mirrors", *Appl. Phys. Lett.* **95**, 211101 (2009).

- [Sau13] C. Sauvan, J. P. Hugonin, I. S. Maksymov, and P. Lalanne, "Theory of the spontaneous optical emission of nanosize photonic and plasmon resonators", *Phys. Rev. Lett.* **110**, 237401 (2013).
- [Sav11] V. Savona, "Electromagnetic modes of a disordered photonic crystal", *Phys. Rev. B* **83**, 085301 (2011).
- [Sch10] J. A. Schuller, E. S. Barnard, W. Cai, Y. Chul Jun, J. S. White, and M. L. Brongersma, "Plasmonics for extreme light concentration and manipulation", *Nat. Mater.* **9**, 193-204 (2010).
- [Scu11] M.G. Scullion, A. Di Falco, and T.F. Krauss, "Slotted photonic crystal cavities with integrated microfluidics for biosensing applications", *Biosens. Bioelectron.* **27**, 101-105 (2011).
- [Scu13] M. G. Scullion, T. F. Krauss, and A. Di Falco, "Slotted photonic crystal sensors", *Sensors* **13**, 3675–3710 (2013).
- [Scu14] M. G. Scullion, A. Di Falco, and T. F. Krauss, "Contra-directional coupling into slotted photonic crystals for spectrometric applications", *Opt. Letters* **39**, 4345-4348 (2014).
- [Seb06] P. Sebbah, B. Hu, J. M. Klosner, and A. Z. Genack, "Extended Quasimodes within Nominally Localized Random Waveguides", *Phys. Rev. Lett.* **96**, 183902 (2006).
- [Seg13] M. Segev, Y. Silberberg, D. N. Christodoulides, "Anderson localization of light", *Nat. Photonics* **7**, 197–204 (2013).
- [Sil01] E. Silberstein, P. Lalanne, J. P. Hugonin, and Q. Cao, "Use of grating theories in integrated optics", *J. Opt. Soc. Am. A* **18**, 2865–2875 (2001).
- [Smo11] S. Smolka, H. Thyrrerstrup, L. Sapienza, T. B Lehmann, K. R Rix, L. S Froufe-Pérez, P. D García, and P. Lodahl, "Probing the statistical properties of Anderson localization with quantum emitters", *New J. Phys.* **13**, 063044 (2011).
- [Sny83] A. W. Snyder, and J. D. Love, "Optical Waveguide Theory" (Chapman and Hall NY, 1983).
- [Sol02] M. Soljačić, S. G. Johnson, S. Fan, M. Ibanescu, E. Ippen, and J. D. Joannopoulos, "Photonic-crystal slow-light enhancement of nonlinear phase sensitivity", *J. Opt. Soc. Am. B* **19**, 2052-2059 (2002).
- [Sol04] M. Soljacić, and J. D. Joannopoulos, "Enhancement of nonlinear effects using photonic crystals", *Nat. Mater.* **3**, 211–219 (2004).
- [Sol15] I. Söllner, S. Mahmoodian, S. L. Hansen, L. Midolo, A. Javadi, G. Kiršanskė, T. Pregnolato, H. El-Ella, E. H. Lee, J. D. Song, S. Stobbe, and Peter Lodahl, "Deterministic photon-emitter coupling in chiral photonic circuits", *Nat. Nanotech.* **10**, 775–778 (2015).
- [Son05] B. S. Song, S. Noda, T. Asano, and Y. Akahane, "Ultra-high-Q photonic double-heterostructure nanocavity", *Nat. Mater.* **4**, 207–210 (2005).

- [Sor87] R. A. Soref, and B. R. Bennett, "Electrooptical effect in silicon", *IEEE J. Quantum Electron* **23**, 123-129 (1987).
- [Spa12] M. Spasenović, D. M. Beggs, P. Lalanne, T. F. Krauss, and L. Kuipers, "Measuring the spatial extent of individual localized photonic states", *Phys. Rev. B* **86**, 155153 (2012).
- [Spe92] M. Specht, J. D. Pedarnig, W. M. Heckl, and T. W. Hänsch, "Scanning plasmon near-field microscope", *Phys. Rev. Lett.* **68**, 476 (1992).
- [Ste02] S. G. Johnson, P. Bienstman, M. A. Skorobogatiy, M. Ibanescu, E. Lidorikis, and J. D. Joannopoulos, "Adiabatic theorem and continuous coupled-mode theory for efficient taper transitions in photonic crystals", *Phys. Rev. E* **66**, 066608 (2002).
- [Sto02] M. I. Stockman, S. V. Faleev, and D. J. Bergman, "Coherent Control of Femtosecond Energy Localization in Nanosystems", *Phys. Rev. Lett.* **88**, 067402 (2002).
- [Sto07] M. I. Stockman, M. F. Kling, U. Kleineberg, and F. Krausz, "Attosecond nanoplasmonic-field microscope", *Nature Phot.* **1**, 539 (2007).
- [Sun13] Q. Sun, K. Ueno, H. Yu, A. Kubo, Y. Matsuo, and H. Misawa, "Direct imaging of the near field and dynamics of surface plasmon resonance on gold nanostructures using photoemission electron microscopy", *Light: Sci. Appl.* **2**, e118 (2013).
- [Taf00] A. Taflove and S. Hagness, *Computational Electrodynamics: The Finite-Difference Time-Domain Method*, (2nd edition, Artech House, 2000).
- [Tag11] Y. Taguchi, Y. Takahashi, Y. Sato, T. Asano, and S. Noda, "Statistical studies of photonic heterostructure nanocavities with an average Q factor of three million", *Opt. Express* **19**, 11916–11921 (2011).
- [Tam08] T. H. Taminiau, F. D. Stefani, F. B. Segerink, and N. F. van Hulst, "Optical antennas direct single-molecule emission", *Nature Photon.* **2**, 234 (2008).
- [Tey08] M. K. Tey, Z. Chen, S. A. Aljunid, B. Chng, F. Huber, G. Maslennikov, and C. Kurtsiefer, "Strong interaction between light and a single trapped atom without the need for a cavity", *Nat. Phys.* **4**, 924 (2008).
- [Tho13] J. D. Thompson, T.G. Tiecke, N. P. de Leon, J. Feist, A.V. Akimov, M. Gullans, A. S. Zibrov, V. Vuletic, and M. D. Lukin, "Coupling a single trapped atom to a nanoscale optical cavity", *Science* **340**, 1202 (2013).
- [Thy12] H. Thyrestrup, S. Smolka, L. Sapienza, and P. Lodahl, "Statistical Theory of a Quantum Emitter Strongly Coupled to Anderson-Localized Modes", *Phys. Rev. Lett.* **108**, 113901 (2012).
- [Top07] J. Topolancik, B. Ilic, and F. Vollmer, "Experimental Observation of Strong Photon Localization in Disordered Photonic Crystal Waveguides", *Phys. Rev. Lett.* **99**, 253901 (2007).
- [Vah03] K. Vahala, "Optical microcavities", *Nature* **424**, 839-846 (2003)

- [Vel07] P. Velha, J. P. Hugonin, and P. Lalanne, "Compact and efficient injection of light into band-edge slow-modes", *Opt. Express* **15**, 6102–6112 (2007).
- [Ver98] D. W. Vernooy, A. Furusawa, N. P. Georgiades, V. S. Ilchenko, and H. J. Kimble, "Cavity QED with high-Q whispering gallery modes", *Phys. Rev. A* **57**, R2293–R2296 (1998).
- [Ver09] N. Verellen, Y. Sonnefraud, H. Sobhan, F. Ha, V. V. Moshchalkov, P. Van Dorpe, P. Nordlander, and S. A. Maier, "Fano Resonances in Individual Coherent Plasmonic Nanocavities", *Nano Lett.* **9**, 1663–1667 (2009).
- [Vet10] E. Vetsch, D. Reitz, G. Sagué, R. Schmidt, S. T. Dawkins, and A. Rauschenbeutel, "Optical Interface Created by Laser-Cooled Atoms Trapped in the Evanescent Field Surrounding an Optical Nanofiber", *Phys. Rev. Lett.* **104**, 203603 (2010).
- [Via14] B. Vial, F. Zolla, A. Nicolet, and M. Commandré, "Quasimodal expansion of electromagnetic fields in open two-dimensional structures", *Phys. Rev. A* **89**, 023829 (2014).
- [Vil94] P.R. Villeneuve, and M. Piché, "Photonic bandgaps in periodic dielectric structures", *Prog. Quant. Electron.* **18**, 153–200 (1994).
- [Vin04] A. P. Vinogradov, and A. M. Merzlikin, "Band theory of light localization in one-dimensional disordered systems", *Phys. Rev. E. Stat. Nonlin. Soft Matter Phys.* **70**, 026610 (2004).
- [Vog15] J. Vogelsang, J. Robin, B. J. Nagy, P. Dombi, D. Rosenkranz, M. Schiek, P. Groß, and C. Lienau, "Ultrafast Electron Emission from a Sharp Metal Nanotaper Driven by Adiabatic Nanofocusing of Surface Plasmons", *Nano Lett.* **15**, 4685 (2015).
- [Vyn12] K. Vynck, M. Burrese, F. Riboli, and D. S. Wiersma, "Photon management in two-dimensional disordered media", *Nat. Mater.* **11**, 1017–1022 (2012).
- [Wan08] B. Wang, S. Mazoyer, J. P. Hugonin, and P. Lalanne, "Backscattering in monomode periodic waveguides", *Phys. Rev. B* **78**, 245108 (2008).
- [Wan10] F. Wang, H. Yu, J. Li, X. Sun, X. Wang, and H. Zheng, "Optical absorption enhancement in nanopore textured-silicon thin film for photovoltaic application", *Opt. Lett.* **35**, 40–42 (2010).
- [Xia07] F. Xia, L. Sekaric, and Y. Vlasov, "Ultracompact optical buffers on a silicon chip", *Nat. Photon.* **1**, 65–71 (2007).
- [Xue16] W. Xue, Y. Yu, L. Ottaviano, Y. Chen, E. Semenova, K. Yvind, and J. Mork, "Threshold Characteristics of Slow-Light Photonic Crystal Lasers", *Phys. Rev. Lett.* **116**, 063901 (2016).
- [Yam11a] N. Yamamoto, S. Ohtani, and F. J. García de Abajo, "Gap and Mie plasmons in individual silver nanospheres near a silver surface", *Nano Lett.* **11**, 91–95 (2011).

- [Yam11b] S. Yamada, B.-S. Song, T. Asano, and S. Noda, "Experimental investigation of thermo-optic effects in SiC and Si photonic crystal nanocavities", *Opt. Letters* **36**, 3981 (2011).
- [Yan03] M. F. Yanik, S. Fan, and M. Soljacic, "High-contrast all-optical bistable switching in photonic crystal microcavities", *Appl. Phys. Lett.* **83**, 2739 (2003).
- [Yan11] J. K. Yang, H. Noh, M. J. Rooks, G. S. Solomon, F. Vollmer, and H. Cao, "Lasing in localized modes of a slow light photonic crystal waveguide. *Appl. Phys. Lett.* **98**, 241107 (2011).
- [Yan12] J. Yang, C. Sauvan, A. Jouanin, S. Collin, J. L. Pelouard, and P. Lalanne, "Ultrasmall metal-insulator-metal nanoresonators: impact of slow-wave effects on the quality factor", *Opt. Express* **20**, 16880-16891 (2012).
- [Yan16a] J. Yang, J. P. Hugonin, and P. Lalanne, "Near-to-Far Field Transformations for Radiative and Guided Waves", *ACS Photonics*, **3**, 395–402 (2016).
- [Yan16b] Y. Yang, B. Zhen, C. W. Hsu, O. D. Miller, J. D. Joannopoulos, and M. Soljacic, "Optically Thin Metallic Films for High-Radiative-Efficiency Plasmonics", *Nano Lett.* **16**, 4110–4117 (2016).
- [Yeg14] E. Yeganegi, A. Lagendijk, A. P. Mosk, and W. L. Vos, "Local density of optical states in the band gap of a finite one-dimensional photonic crystal", *Phys. Rev B* **89**, 045123 (2014).
- [Yeh88] P. Yeh, "Optical Waves in Layered Media" (Wiley, New York, 1988).
- [Yu11] N. Yu, Patrice Genevet, M. A. Kats, F. Aieta, J.-P. Tetienne, F. Capasso, and Z. Gaburro, "Light Propagation with Phase Discontinuities: Generalized Laws of Reflection and Refraction", *Science* **334**, 333-337 (2011).
- [Yu14] S.-P. Yu, J. D. Hood, J. A. Muniz, M. J. Martin, R. Norte, C.-L. Hung, S.M. Meenehan, J. D. Cohen, O. Painter, and H. J. Kimble, "Nanowire photonic crystal waveguides for single-atom trapping and strong light-matter interactions", *Appl. Phys. Lett.* **104**, 111103 (2014).
- [Zan15] X. Zang, and P. Lalanne, "Theoretical treatment of the interaction between two-level atoms and periodic waveguides", *Opt. Lett.* **40**, 3869-3872 (2015).
- [Zan16] X. Zang, J. Yang, R. Faggiani, C. Gill, P. G. Petrov, J.-P. Hugonin, K. Vynck, S. Bernon, P. Bouyer, V. Boyer, and P. Lalanne, "Interaction between Atoms and Slow Light: A Study in Waveguide Design", *Phys. Rev. Appl.* **5**, 024003 (2016).
- [Zha08] S. Zhang, D. A. Genov, Y. Wang, M. Liu, and X. Zhang, "Plasmon-Induced Transparency in Metamaterials", *Phys. Rev. Lett.* **101**, 047401 (2008).